Paramagnetic Spin-up of a Field Reversed Configuration with Rotating Magnetic Field Current Drive

Andrew Maxwell Peter

A dissertation submitted in partial fulfillment of the
requirements for the degree of

Doctor of Philosophy

University of Washington

2003

Program Authorized to Offer Degree: Aeronautics and Astronautics

ProQuest Information and Learning Company
300 North Zeeb Road
P.O. Box 1346
Ann Arbor, MI 48106-1346

In presenting this thesis in partial fulfillment of the requirements for the Doctoral degree at the University of Washington, I agree that the Library shall make its copies freely available for inspection. I further agree that extensive copying of the dissertation is allowable only for scholarly purposes, consistent with "fair use" as prescribed in the U.S. Copyright Law. Requests for copying or reproduction of this dissertation may be referred to ProQuest Information and Learning, 300 North Zeeb Road, Ann Arbor, MI 48106-1346, to whom the author has granted "the right to reproduce and sell (a) copies of the manuscript in microform and/or (b) printed copies of the manuscript made from microform".

Signature 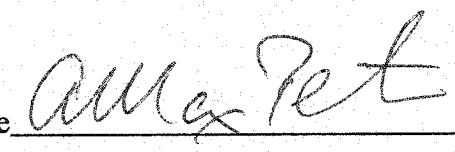

Date 6/3/03

University of Washington

Graduate School

This is to certify that I have examined this copy of a doctoral dissertation by

Andrew Maxwell Peter

and have found that it is complete and satisfactory in all respects,
and that any and all revisions required by the final
examining committee have been made.

Chair of Supervisory Committee:

Alan L. Hoffman

Reading Committee:

Alan L. Hoffman

Thomas R. Jarboe

Uri Shumlak

Date: 6/3/03

University of Washington

Abstract

Paramagnetic Spin-up of a Field Reversed Configuration with
Rotating Magnetic Field Current Drive

Andrew Maxwell Peter

Chair of the Supervisory Committee:
Professor Alan. L. Hoffman
Aeronautics and Astronautics

A transverse Rotating Magnetic Field (RMF) can drive toroidal current and sustain the poloidal flux of a Field Reversed Configuration (FRC) through the application of a $\langle v_z \times B_r \rangle$ Lorentz force on the electrons, where v_z is the axial screening current and B_r is the radial component of the RMF. The torque applied by the RMF will eventually be transferred to the ions through resistive collisions. In the absence of any drag force, the plasma will rapidly spin up in the ion paramagnetic direction, negating the current drive and possibly becoming rotationally unstable. A multi-chord Intensified Charge-Coupled Device (ICCD) spectrometer has measured the ion rotation profile via the Doppler shift of impurity line radiation in the Translation, Confinement, and Sustainment (TCS) experiment. The plasma is observed to rapidly spin up in the ion paramagnetic direction to a rigid rotation frequency of about $\omega_i \approx 7\times10^4$ s^{-1}, less than 15% of the typical RMF frequency $\omega \approx 0.5\times10^6$ s^{-1}. Neutral deuterium is observed to have no rotational velocity, and had been proposed as a mechanism for preventing synchronous spin-up of the ions. The neutral density and resulting charge-exchange and ionization rates have been calculated from an array of absolutely calibrated Dα detectors. The typical neutral fraction of about 2% of the plasma density is several times too low for ion-neutral collisions to balance the applied torque. Other possible braking mechanisms are shorting of the radial electric field needed to confine paramagnetic ions, and viscous drag. Assuming axial and azimuthal symmetry and pure deuterium, viscous wall drag is found to be insufficient to slow the plasma as well. Viscous drag could be significant if the edge plasma has high impurity content or is spatially non-uniform.

TABLE OF CONTENTS

LIST OF FIGURES

LIST OF TABLES

GLOSSARY

CSS .....Coaxial Slow Source

FFT.....Fast Fourier Transform

FLR .....Finite Larmor Radius

FRC.....Field Reversed Configuration

FRTP.....Field Reversed Theta Pinch

FWHM.....Full-Width at Half-Maximum

HWHM .....Half-Width at Half-Maximum

ICCD.....Intensified Charge-Coupled Device

IDS .....Ion Dynamics Spectrometer

LSX.....Large s Experiment

MCP.....Microchannel Plate

MHD .....Magnetohydrodynamics

PMT .....Photomultiplier Tube

PSF.....Point Spread Function

PSD .....Power Spectral Density

PTG.....Programmable Timing Generator

RMF.....Rotating Magnetic Field

RPPL.....Redmond Plasma Physics Laboratory

STX.....Star Thrust Experiment

TCS .....Translation, Confinement, and Sustainment Experiment

TRAP .....Tokamak Refueling by Accelerated Plasmoids

ACKNOWLEDGEMENTS

The author wishes to thank Ed Crawford for his extensive help with the design and implementation of the ICCD system. Many thanks are due to Alan Hoffman, Richard Milroy, John Slough, and Loren Steinhauer for their guidance, as well as to Houyang Guo for his help with TCS operation. This research utilized many of the TCS diagnostics and recognition is due to the scientists and students who assisted with these measurements. In particular, thanks to George Votroubek for his work with the tomography, interferometer, and Dα systems, Ken Miller for his work with the internal magnetic probe, and Adam Pietrzyk for assistance with the power balance model.

The author also thanks his parents, Tom and Marjie, and his grandparents, Bill and Dori, for their love and support.

DEDICATION

To my wife Amy,

I could not have done this without you.

Chapter One

Introduction

Thermonuclear fusion has the potential to be a nearly unlimited energy source with no greenhouse gas emissions and little nuclear waste. For two light ions to fuse into a single heavier one, the reactants must collide with sufficient energy to overcome their electrostatic repulsion. For example, the deuterium-tritium fusion cross-section becomes sufficiently large to make a favorable reactor only at an ion temperature of 10 keV (100 million degrees centigrade). Such high temperature ions cannot be confined by material walls; instead, magnetic fields can provide the necessary confinement. A fundamental consequence of the Lorentz force ($\boldsymbol{F} = q\mathbf{v}\times\boldsymbol{B}$) is that charged particles are restricted to orbit around magnetic field lines. If the magnetic fields are designed such that they form closed flux surfaces inside the vacuum vessel, then the plasma will be magnetically confined, only contacting the walls through diffusion across the field lines.

1.1 The FRC and RMF Current Drive

Of the many magnetic confinement schemes, the Field Reversed Configuration (FRC) is one of the most innovative and attractive from a reactor viewpoint. It has a simple linear geometry, a natural divertor for fusion products, and is very efficient. Conventionally, FRCs have been formed by the Field Reversed Theta Pinch (FRTP) technique, using high-voltage capacitor banks to shock heat the plasma to high temperatures. However, FRTP formation is limited in three ways. Technologically, the plasma size and energy are limited by the high voltage and fast switching required by this formation method. Second, FRTP formation involves an axial implosion, so the quality of the resulting FRC is highly sensitive to the symmetry and timing of the formation. Finally, because of the simple closed geometry there is no way to inductively sustain the plasma current and the FRC resistively decays away after formation.

Rotating Magnetic Field (RMF) current drive can potentially remove these limitations. In this method of current drive, a transverse magnetic field is applied in addition to the larger axial field and is rotated azimuthally in time. Simply put, if the electrons are magnetized in the rotating magnetic field while the ions are not, then only the electrons will follow the field as it rotates, driving toroidal plasma current. If this toroidal current drive matches the resistive decay rate, then the poloidal flux will be constant and the FRC can be maintained in essentially steady state. If the RMF current drive is stronger than the resistive loss, then the poloidal flux can actually be increased; in this manner, FRCs can be formed from a preionized gas directly by the RMF without the need for shock heating or pulsed high-voltage capacitors.

The purpose of the Translation, Confinement, and Sustainment (TCS) experiment is to study the physics of RMF current drive in an FRC. The TCS experiment can be operated in two distinct modes. In the RMF formation mode, an FRC is formed in the sustainment section using RMF current drive alone. This mode completely avoids the difficulties associated with FRTP formation, although it is limited by the few megawatts of input power that the RMF supply can produce. In the second, translated mode, a more energetic FRC is formed using the high-voltage FRTP coils in the formation section. Because these coils can supply gigawatts of instantaneous power, the plasma can be rapidly heated through the radiation barriers to high temperature. The FRC is then translated into the sustainment section, where it is expanded to the lower density necessary for efficient current drive. RMF current drive is then applied with the goal of sustaining the hot FRC.

One potential drawback of RMF current drive is that it puts a net torque on the FRC. At first, only the electrons respond to this torque and toroidal current is driven. Eventually, this torque will spin the ions as well through resistive collisions with the electrons. Ion azimuthal velocity negates the current drive and may lead to rotational

instabilities. Because the ions are rotating in the same direction as the electrons, this is ion paramagnetic rotation and is in contrast with the usual ion diamagnetic rotation associated with conventional FRCs. Previous RMF experiments have relied on a large neutral background and wall viscosity to provide the necessary drag on the ions to prevent them from spinning up. In the future, however, the importance of neutral drag will diminish as experiments reach higher temperatures, have longer confinement times, and employ more wall-conditioning techniques to lower the neutral background. In order to maintain current drive in steady state, these experiments may require an opposing torque to be applied, either by neutral beams or counter-rotating magnetic fields. It is hoped that additional braking mechanisms may be relied upon as well, such as end shorting of the radial electric field and viscous momentum transfer to the wall or open field plasma.

Besides lowering the current drive efficiency, plasma rotation also tends to drive rotational instabilities, particularly the n = 2 rotational flute. This mode often develops in TCS when the plasma radius is compressed inwards from the wall. The mode can degrade the plasma performance by locally ablating the quartz vacuum wall, introducing silicon and oxygen impurities into the plasma. Rotational instability is often observed in conventional FRCs due to diamagnetic rotation. In previous experiments, multipole fields have been used to stabilize these modes. It is hoped that the same stabilization techniques can be applied to paramagnetically rotating modes driven by the applied torque of the rotating magnetic field.

Clearly, a detailed understanding of the various forces acting on the ions in an RMF-driven FRC is crucial. This research aims to understand the complex forces acting on the ions and how these forces reach equilibrium. In order to accomplish this, a multi-chord intensified charge-coupled device (ICCD) spectrometer has been installed on TCS. The ICCD spectrometer can determine the plasma rotation profile from the Doppler shift of impurity line radiation. To quantify the importance of neutral

drag, an array of Dα emission detectors allows a determination of the background neutral density. A global power balance calculation using bolometric, interferometric, and magnetic measurements is used to verify the neutral density calculation. Plasma rotation often leads to rotation instability. The mode structure of the n=2 flute is studied using visible-light tomographic reconstruction, and the mode frequency is compared with the actual plasma rotation frequency.

1.2 Dissertation Overview

This paper is organized in the following way. Chapter two describes the general properties of the field-reversed configuration, including equilibrium and stability. Chapter three introduces the physics of rotating magnetic field current drive. Simple analytic expressions for the penetration of a rotating field into a plasma column are presented. This model assumes that the ions do not rotate in the toroidal direction. As this constraint is relaxed, a simple two-fluid model that neglects the RMF azimuthal force directly on the ions is developed. This model predicts that the plasma rotation will reach a steady-state value when the electron friction balances the drag forces on the ions. Chapter three concludes with a review of previous RMF research. Chapter four summarizes the TCS experiment, including the RMF supply and the general diagnostics. Chapter five focuses specifically on the ICCD Doppler spectroscopy diagnostic. This chapter describes the experimental setup of the ICCD spectrometer, the calibration techniques, and the deconvolution and spatial inversion methods. Results from this diagnostic are presented in chapter six. Chord-integrated velocity profiles and inverted emission and rotation profiles are presented. Within the accuracy of the diagnostic, the plasma rotation is found to be rigid. The dependence of the rotation on RMF frequency, plasma density, and applied torque is examined. The rotation rate is also compared with the n = 2 mode frequency and the two are found to be synchronous. In chapter seven, the background neutral density is calculated from neutral Dα emission. Two important momentum loss mechanisms, ionization and charge-exchange, are examined. A global power balance is used to validate the neutral

density calculation. Radiation is seen to be the dominant power loss mechanism. Chapter eight estimates the applied torque on the FRC and compares it with the neutral drag torque. This includes charge-exchange, ion-neutral elastic collisions, and fueling. Ion-neutral interactions are found to be insufficient to explain the relatively low ion spin-up observed in TCS. Viscous drag to the wall is estimated, although only limited measurements of the edge plasma parameters are available. If the edge plasma is pure deuterium, viscous drag to the wall is insufficient to slow the plasma. Viscous drag could still be significant if the edge plasma has high impurity content or is spatially non-uniform. In Chapter nine, the simple model of ion rotation first presented in Chapter three is expanded. The relative importance of the RMF force directly on the ions is examined using a two-fluid model solved for a fixed field. End-shorting of the radial electric field is also considered as a possible drag torque on the plasma. Chapter ten summarizes the findings and projects them for future experiments. Finally, statistical error analysis is presented in appendix A.

Chapter Two

The Field Reversed Configuration

The field reversed configuration[i], or FRC, is an elongated ring of azimuthal plasma current confined by an axial magnetic field. It is distinct from other magnetic confinement geometries in that it is a prolate compact toroid with little or no toroidal field. The FRC has a simple cylindrical geometry with no walls or coils linking the "hole" of the plasma torus, as in a tokamak. This simple geometry along with inherent high beta and a natural divertor make the FRC attractive as a potential fusion reactor. Unfortunately, it is also one of the least studied magnetic geometries, primarily because MHD theory predicts it to be unstable to the internal tilt mode[ii]. Experimentally this mode is not observed[iii], possibly because of kinetic effects[iv] or two-fluid effects with sheared flow[v].

Previous FRC experiments[vi] have reached total temperatures greater than 1keV, densities of the order of 10^{21} m^{-3}, and energy confinement times as long as 300 μs. However, these experiments have been limited by the flux lifetime of the FRC. Because the FRC is a compact toroid, magnetic induction cannot be used to drive and sustain toroidal plasma current and the FRC decays away resistively. It is this limitation and the need to produce higher-flux FRCs that has led to the present research in RMF current drive.

This chapter will introduce the terminology and general properties of the field reversed configuration. Sec. 2.1 describes the FRC equilibrium, geometry, and rigid rotor model. Sec. 2.2 addresses the MHD stability of the FRC, particularly rotational stability.

2.1 Equilibrium

The simplest way to introduce the field reversed configuration equilibrium is to describe how one is formed by the conventional field reversed theta-pinch (FRTP) method. The FRC is formed in a cylindrical vacuum vessel so it is customary to use cylindrical (r,θ,z) coordinates. A uniform axial magnetic field, or bias field, is created in the vacuum chamber using solenoidal theta-pinch coils. A gas is then pre-ionized in the axial magnetic field. This pre-ionization plasma is cold but sufficiently conducting to be "magnetized"; that is, the axial magnetic field is frozen into the plasma. The current in the theta-pinch coil is rapidly reversed, reversing the external magnetic field as well. This change in magnetic field creates a toroidal electric field in the plasma according to Faraday's Law ($\nabla \times E = -\partial B_z/\partial t$). The electric field drives a toroidal current in the plasma that traps the original reverse bias field. The plasma current ring is then compressed off of the walls by further increasing the external magnetic field. As the plasma is radially compressed, the reverse bias field lines connect with the external magnetic field lines to form closed poloidal field lines. Plasma within these closed field lines is magnetically confined. The FRC then contracts axially until an axial pressure balance is reached. The axial field coils are now shorted with a "crowbar" switch. Since the L/R time of the shorted coils is long compared to the lifetime of the FRC, the coils effectively act as an axial magnetic flux conserver for the duration of the experiment. As mentioned above, without a current drive method the azimuthal plasma current will resistively decay away.

A schematic of a fully formed FRC is shown in Fig. 2.1. Shown are the coil radius r_c, the vacuum wall radius r_w, the separatrix radius r_s (defined as the radius of the last closed poloidal field line), and the field null radius R. The basic geometric property of an FRC is the ratio of the separatrix radius to the coil radius, denoted as $x_s \equiv r_s/r_c$. The FRC is a flux-excluding object; its presence compresses the axial magnetic field from the vacuum value B_o to the excluded value B_e given by $B_e = B_o/(1-x_s^2)$. It is this magnetic field compression that provides the plasma confinement.

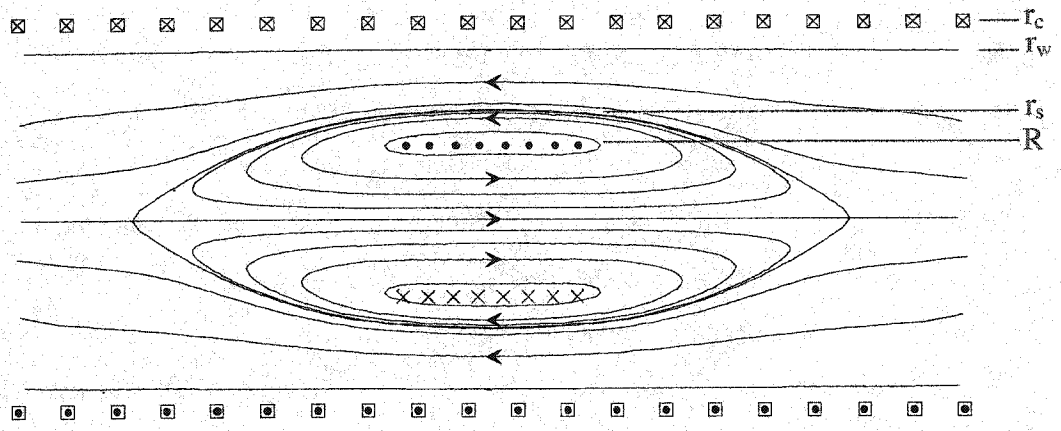

Figure 2.1: *The Field Reversed Configuration. r_c = coil radius, r_w = vacuum wall radius, r_s = separatrix radius, R = magnetic field null radius.*

The plasma pressure is a flux surface quantity $\left(p = p(\psi)\right)$ and is constant along a field line. The separatrix radius and the field null radius are then simply related by $r_s = \sqrt{2}R$. The overall efficiency of the applied magnetic field at confining plasma pressure can be found by assuming that the FRC is sufficiently elongated so that the magnetic field lines are straight (no curvature) at the axial midplane. Defining β as the ratio of the plasma pressure to the magnetic field energy density, the "average beta relation" is expressed as:

$$\langle \beta \rangle \equiv \frac{\langle p \rangle}{B_e^2/2\mu_o} = 1 - \frac{x_s^2}{2}. \tag{2.1}$$

While pressure is equivalent to the energy in the plasma, it is the poloidal flux that determines the energy confinement. The poloidal flux Φ_p is the "trapped" or closed magnetic flux from the geometric axis out to the field null, which must also equal the flux from the null to the separatrix:

$$\Phi_p \equiv -\int_0^R 2\pi r B_z(r)dr = \int_R^{r_s} 2\pi r B_z(r)dr. \tag{2.2}$$

A given x_s and B_e do not uniquely determine the poloidal flux. The azimuthal current distribution must also be specified. One such current distribution model, the rigid rotor profile, assumes that the ions are stationary while the electrons rotate as a rigid body, i.e. $j_\theta = -en_e(r)\omega r$, where ω is the rigid rotation frequency. With the further assumption that the plasma temperature is uniform, this yields the self-consistent magnetic field profile $B_z(u) = B_e \tanh(Ku)$, where K is a fitting parameter and u is the dimensionless radial coordinate $u \equiv (r/R)^2 - 1$. The plasma pressure profile is then $p(u) = p_m \mathrm{sech}^2(Ku)$, where p_m is the maximum pressure at the null, set by the external field $p_m = B_e^2/2\mu_0$. The rigid rotor profile yields a poloidal flux $\Phi_p \approx 0.61 x_s(\pi R^2 B_e)$. The rigid rotor profiles are shown in Fig. 2.2 for a typical K value of 1.5.

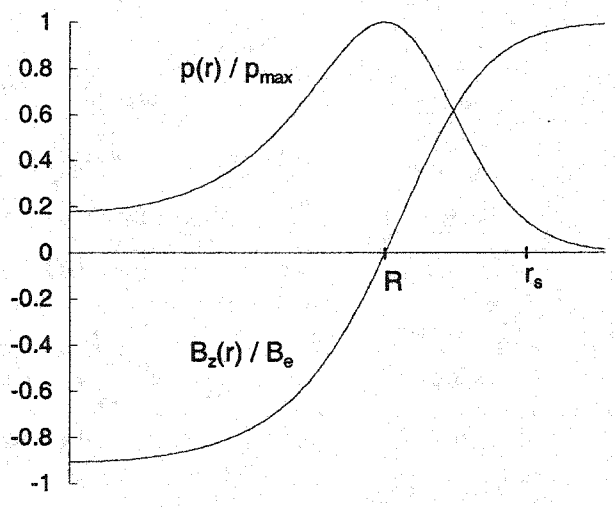

***Figure 2.2**: Rigid Rotor Profiles. Normalized magnetic field and plasma pressure are shown for K = 1.5 (corresponding to x_s = 0.89), typical for an RMF-sustained FRC.*

2.2 Stability

The FRC has proven to be remarkably stable. This is most evident in the TCS translation experiments, where an FRC is translated super-Alfvénically into the

confinement chamber. After multiple reflections off of the end cones, the FRC converts a large fraction of its kinetic energy into thermal energy. The FRC recovers from these violent reflections to form a stable, quiescent equilibrium.

Stability is examined using the MHD model. The tokamak nomenclature for ideal MHD modes is used, with n and m being the toroidal and poloidal mode numbers, respectively. The FRC is neutrally stable to the m = 1, n = 0 axial shift, but this "Roman Candle" shift can easily be stabilized with modest end mirrors. MHD theory predicts the FRC to be unstable to the m =1, n = 1 internal tilt mode[2]. However, this mode has been absent in experiment. One of the leading theories for the apparent stability of this mode relies on Finite Larmor Radius (FLR) effects[4]. This is quantified by the kinetic s parameter, defined as the number of ion gyroradii between the field null and the separatrix. Specifically,

$$s \equiv \int_{R}^{r_s} \frac{rdr}{r_s \rho_i(r)} \tag{2.3}$$

where ρ_i is the ion gyroradius. The Large s Experiment[7] (LSX) was designed specifically to investigate the stability of FRCs at high s values. LSX successfully formed high-quality FRCs with s values as high as four. The apparent stability of the FRC to the internal tilt mode even at such high s values is still not completely resolved but is not the subject of the present research. In the present experiment, TCS plasmas are typically formed with s of the order unity, (depending on ion temperature) and have a lifetime of up to 2 ms, limited by the charging capacitor in the RMF circuit. The TCS plasmas are therefore assumed stable to the internal tilt mode.

The only MHD modes observed in modern FRC experiments are the rotational instabilities. The m = 1, n = 1 wobble saturates at finite amplitude and is typically not destructive. The m = 1, n = 2 rotating flute, however, can be destructive and was the limiting factor in early FRC experiments. The centrifugal force per unit volume of a spinning fluid is simply

$$f_c(r) = \rho\Omega^2 r, \tag{2.4}$$

where ρ and Ω are the fluid density and rotation frequency, respectively. The centrifugal pressure is then the integral:

$$p_c = \int_0^{r_s} f_c(r)dr = \frac{1}{2}\rho\Omega^2 r_s^2 \tag{2.5}$$

Rotational modes, then, are a type of pressure-driven instability. Research at Osaka University demonstrated that the centrifugal pressure can be balanced by magnetic pressure applied with multipole fields[8]. The n = 2 rotational instability has been shown to be suppressed using this technique[9].

To determine if a given rotation rate will lead to instability, a small initial disturbance ξ is expressed as a Fourier mode

$$\xi = \tilde{\xi} e^{i(n\phi + m\theta - \omega_r t)} e^{\gamma t}, \tag{2.6}$$

where the complex mode frequency has been split into a real part ω_r and an imaginary part representing the growth rate γ. The change in system energy δW due to the disturbance can then be calculated. If the energy change is positive, then the mode will be stable; if the change in energy is negative, then the disturbance releases free energy and the mode will grow. Ideal MHD theory predicts that for any m = 1, n = 2 disturbance the growth rate is always positive and the mode is unstable. However, when kinetic effects are included in the analysis, the n = 2 mode is only unstable beyond a threshold value of ion rotation frequency, or Ω. This is often related to the ion diamagnetic drift frequency Ω_{Di} by the ratio $\alpha \equiv \Omega/\Omega_{Di}$.

The diamagnetic drift is a fluid drift not present in single-particle equations. The fluid momentum equation is

$$mn\left[\frac{\partial \mathbf{v}}{\partial t} + (\mathbf{v}\cdot\nabla)\mathbf{v}\right] = nq(\boldsymbol{E} + \mathbf{v}\times\boldsymbol{B}) - \nabla p \tag{2.7}$$

where drag terms due to resistivity and neutrals have been neglected. The total derivative on the left-hand side of the equation may be safely neglected provided that the fluid drift velocity is smaller than the thermal velocity. Taking the cross product with $\boldsymbol{B}$, the diamagnetic drift velocity is then

$$\mathbf{v}_D \equiv -\frac{\nabla p \times \boldsymbol{B}}{qnB^2}. \tag{2.8}$$

This is a real fluid drift due to pressure gradients even though the particle guiding centers are stationary. The actual ion rotation in an FRC depends on the boundary condition of the radial electric field. For example, when an FRC is formed via the FRTP method, it is assumed that the electrons initially carry all of the diamagnetic current and that the ions remain stationary. Then an inward radial electric field

$$E_r = \frac{1}{en}\frac{\partial p_i}{\partial r} \tag{2.9}$$

develops to confine the ions. A different situation occurs if this electric field is shorted at the boundary condition (a conducting wall, for example). Then the ions must carry their own diamagnetic current and will rotate at the diamagnetic drift frequency. This frequency can be calculated if the pressure profile is known; for example, the rigid rotor ion diamagnetic drift frequency is

$$\Omega_{dia}[s^{-1}] = 4\times10^5 \frac{K}{R^2[cm]}\,\frac{T_i[eV]}{B_e[kG]}. \tag{2.10}$$

The effect of the electric field on the radial component of the ion fluid equation will be examined more closely in Sec. 9.2.

Chapter Three

Rotating Magnetic Field Current Drive

Rotating magnetic field (RMF) current drive is a non-inductive method of driving toroidal plasma current, i.e. it does not rely on transformer action. A transverse magnetic field is rotated azimuthally in time by phasing the alternating current in a pair of dipole antennas apart by 90°, as shown in Fig. 3.1. The simplest physical picture of RMF current drive is that the electrons are magnetized in the transverse field, and thus rotate synchronously with the RMF. The ions, on the other hand, are not magnetized and remain stationary. This has often led to the simple requirement that the angular frequency of the RMF be chosen such that $\omega_{ci} \ll \omega \ll \omega_{ce}$, where ω_{ci} and ω_{ce} are the ion and electron cyclotron frequencies in the *transverse* field. It will be seen below that this simple picture is not physically accurate but is useful as a first approximation of how RMF current drive works.

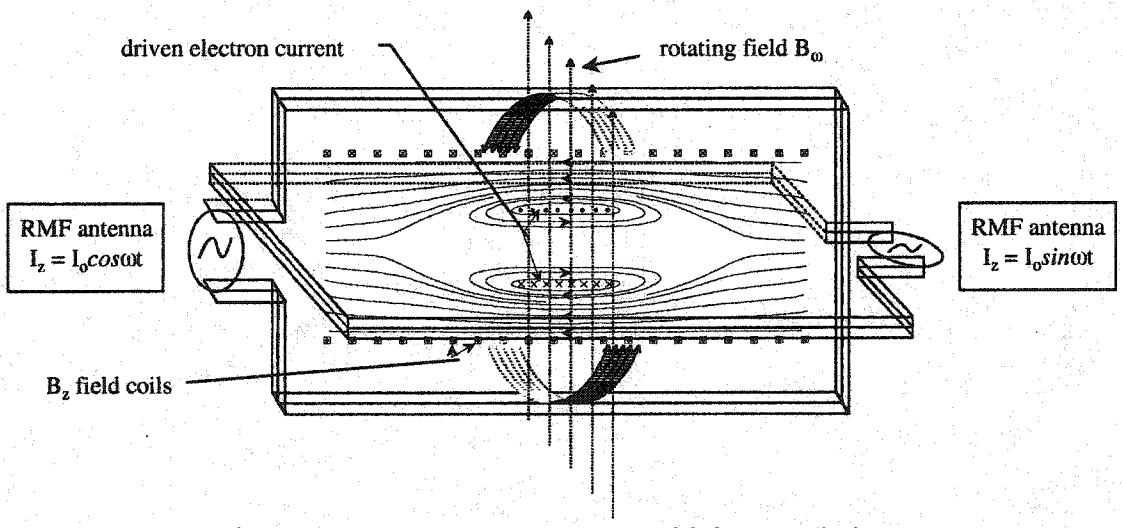

***Figure 3.1:** Rotating Magnetic Field Current Drive*

This chapter will present a more physically accurate model of RMF current drive in an FRC. In Sec. 3.1, the relevant Ohm's law will be made linear by assuming that the electrons rotate as a rigid body and that the ions are immobile. Although this

may not be entirely accurate, the solution will capture the basic physics of partial penetration of the RMF. To calculate the depth of RMF penetration into the FRC, the applied RMF torque is balanced with the resistive torque subject to equilibrium constraints. In Sec. 3.2, the issue of ion rotation is addressed through a much simpler, fully-penetrated RMF model. A steady-state solution for the ion azimuthal velocity is found where the electron-ion friction balances the various drag forces.

3.1 Fixed Ion Model

This section will self-consistently solve for the current distribution and resulting magnetic field profile created in a plasma cylinder subject to a rotating magnetic field. The problem consists of solving the appropriate form of Ohm's law. The problem will be made tractable by assuming that the ions are stationary and the electrons rotate as a rigid body. The same results can be obtained with the less restrictive constraint that the ion azimuthal velocity is zero and that the ion axial oscillation is purely inductive (out of phase with the B_r oscillation). For simplicity, however, the following analysis will assume stationary ions.

As a starting point, the full electron equation of motion is

$$nm_e \frac{D\mathbf{v}_e}{Dt} = -ne\left(\boldsymbol{E} + \mathbf{v}_e \times \boldsymbol{B}\right) - \nabla p_e - nm_e \upsilon_{ei}\left(\mathbf{v}_e - \mathbf{v}_i\right). \tag{3.1}$$

To form a single-fluid Ohm's law, assume that the ions are a fixed background of neutralizing charges. The convective derivative on the left-hand side of Eq. (3.1) can be safely neglected if electron inertia is small compared to the RMF and resistive forces: $(D\mathrm{v}_e/Dt) \approx \omega \ll \omega_{ce}, \upsilon_{ei}$, where hereafter $\omega_{ce} \equiv (eB_\omega/m_e)$ is the cyclotron frequency in the vacuum transverse field unless otherwise specified. Since we will only be solving the axial and azimuthal components of Ohm's law, and the pressure gradient in an FRC is purely radial, the ∇p_e term can be neglected. Defining the scalar resistivity $\eta \equiv m_e \upsilon_{ei}/ne^2$ and the current density $\boldsymbol{j} \equiv -ne\mathbf{v}_e$, Eq. (3.1) can then be written as a single fluid Ohm's law

$$E = \eta j + \frac{1}{ne}(j \times B) \tag{3.2}$$

where the first term is the resistive term and the latter term is the Hall term. Writing the electron momentum equation in this way allows the balance of these two terms to be explored.

Hugrass[10] has shown that in the presence of a rotating magnetic field of the form

$$\boldsymbol{B} = B_\omega \cos(\omega t - \theta)\hat{r} + B_\omega \sin(\omega t - \theta)\hat{\theta}, \tag{3.3}$$

the quantities v_r, v_θ, j_r, j_θ, B_z, E_r, and E_θ can be expressed as infinite sums of odd harmonics, while v_z, j_z, B_r, B_θ, and E_z can be expressed as sums of even harmonics. Neglecting all terms of second order and higher, then only a steady component will remain of the odd terms while a simple oscillating component at frequency ω will remain of the even terms. For example, the resulting velocity field then consists of a steady radial and azimuthal part and an oscillating axial component. With this in mind, we can now express the (steady) azimuthal and (oscillating) axial components of Ohm's law as:

$$\begin{aligned} E_\theta &= \eta_\perp j_\theta + \frac{1}{ne}\langle j_z B_r \rangle + v_{er} B_z \\ E_z &= \eta_\parallel j_z - v_{er} B_\theta - \frac{1}{ne}(j_\theta B_r) \end{aligned} \tag{3.4}$$

where the brackets represent a time-average over an RMF cycle:

$$\langle\ \rangle \equiv \frac{\omega}{2\pi}\frac{1}{2\pi}\int_{t=0}^{2\pi/\omega}\int_{\theta=0}^{2\pi} d\theta dt. \tag{3.5}$$

The azimuthal component of Ohm's law determines if the poloidal flux of the FRC is growing or decaying. For an FRC equilibrium, j_θ is negative and the resistive term leads to decaying poloidal flux. This can be balanced by the azimuthal RMF force due to the $\langle j_z B_r \rangle$ Hall term. Thus, it can be seen that the picture of the electrons being

"tied" to the RMF as it rotates is not physically correct. Instead, the change in transverse field induces an oscillating axial electric field according to Faraday's law. Since we are neglecting electron inertia, the electrons oscillate in this electric field exactly in-phase, or "resistively," with B_r. It is the Lorentz force $\langle v_z B_r \rangle$ that drives the azimuthal current. However, the axial electric field also depends on the resulting azimuthal current because of the $(j_\theta B_r)$ term in the axial equation; this makes Ohm's law coupled and nonlinear.

The radial flow terms have been retained in Eq. (3.4) because we are anticipating only partial penetration of the RMF into the FRC. Equilibrium on inner field lines will then require an inward radial flow. It is unclear whether this radial flow is electron flow or also includes ion flow. For the remainder of this simple analysis, the equations will be linearized by neglecting radial flow and assuming that the electrons are rotating as a rigid body: $j_\theta = -ne\omega_e r$. Eq. (3.4) then simplifies to

$$\begin{aligned} E_\theta &= \eta_\perp (-ne\omega_e r) + \frac{1}{ne}\langle j_z B_r \rangle \\ E_z &= \eta_\parallel j_z + \omega_e r B_r \end{aligned} \tag{3.6}$$

Let us first consider the familiar case of RF penetration into a metal. In metals and plasmas alike the resistivity is low, but for different reasons. Metals have a high υ_{ei} and a high density n. Plasmas have a similar resistivity at much lower density because υ_{ei} is also much lower. In metals, therefore, the Hall term is negligible compared to the resistive term because n is so large. Another way to express this is

$$E = \eta\left[j + (\omega_{ce}/\upsilon_{ei})\, j \times B\right]. \tag{3.7}$$

In metals, the "magnetization" parameter $\gamma \equiv (\omega_{ce}/\upsilon_{ei}) \ll 1$ and Ohm's law is purely resistive. This leads to the familiar resistive skin-depth δ for penetration of an RF field into a metal conductor, $\delta = (2\eta/\mu_o\omega)^{1/2}$. An axial screening current limits the field penetration and there is no azimuthal current drive.

In the opposite extreme of high temperature plasma, the electrons are magnetized in the RMF field. The Hall term then becomes significant in Ohm's law. The $\langle j_z B_r \rangle$ Hall term creates a steady ponderomotive force in the azimuthal direction, driving an azimuthal current not present in the resistive limit. Because the electrons are nearly synchronous with the RMF, the relative frequency $\varpi_e \equiv \omega - \omega_e$ between the two is small and the RMF can penetrate much further into the plasma. This is quantified by an effective skin depth

$$\delta^* \equiv \left(\frac{2\eta}{\mu_o \varpi} \right)^{1/2} \approx \gamma\delta \tag{3.8}$$

which can be much larger than the resistive skin depth.

The solution to Eq. (3.6) was first found by Jones and Hugrass[11] and later applied to the FRC by Hoffman[12]. The electric and magnetic fields are modified Bessel functions

$$\begin{aligned} E_z(r) &= \frac{2\omega}{\sqrt{ik}} \frac{I_1\left(\sqrt{ikr}\right)}{I_0\left(\sqrt{ika}\right)} B_\omega \\ B_r(r) &= \frac{2}{\sqrt{ikr}} \frac{I_1\left(\sqrt{ikr}\right)}{I_0\left(\sqrt{ika}\right)} B_\omega \\ B_\theta(r) &= i\left(B_r - 2\frac{I_1\left(\sqrt{ikr}\right)}{I_0\left(\sqrt{ika}\right)} B_\omega \right) \end{aligned} \tag{3.9}$$

where B_ω is the vacuum field strength, a is the plasma column radius, and $k \equiv \sqrt{2}/\delta^*$. The solutions for various values of ka are plotted in Fig. 3.2 and Fig. 3.3

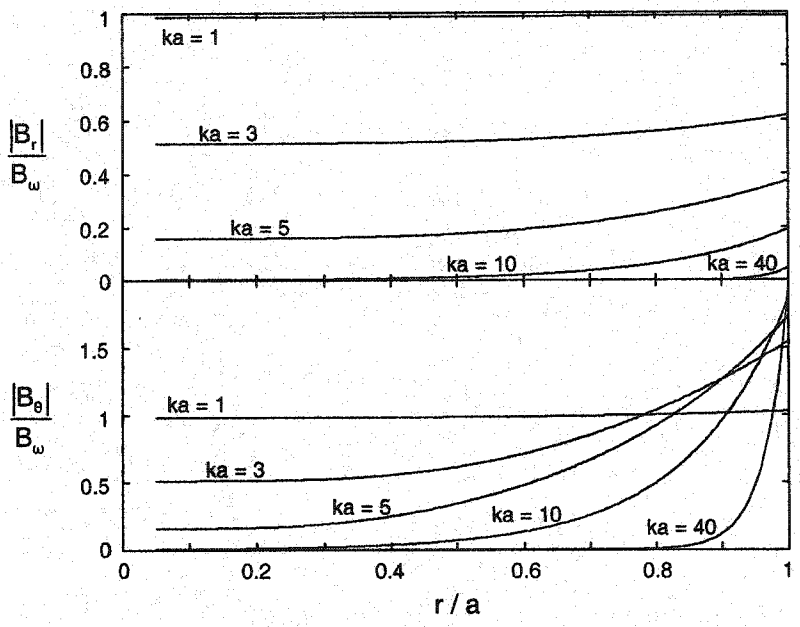

Figure 3.2: RMF Amplitude Profiles.

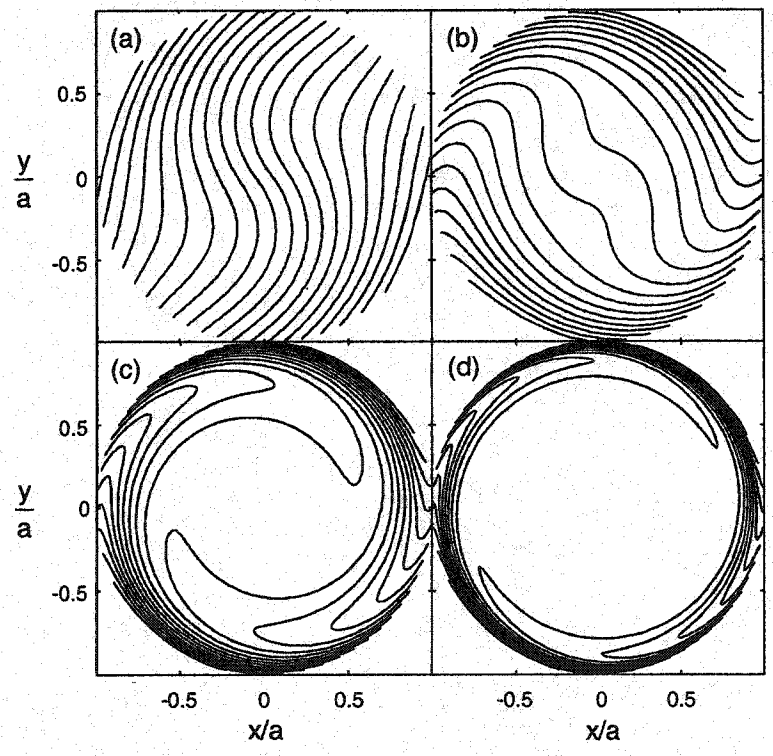

Figure 3.3: Magnetic Field Lines for Various Values of ka. (a) ka=2 (b) ka=5 (c) ka=10 (d) ka=20

The RMF penetration depth δ* will reach an equilibrium value when the net RMF torque balances the resistive friction torque. The applied RMF torque per unit length is

$$T_{RMF} = 2\pi \int_0^a \langle j_z B_r \rangle r^2 dr = T_0 \left(\frac{\sqrt{2} f(ka)}{ka} \right) \tag{3.10}$$

where T_0 and $f(ka)$ are given by

$$T_0 \equiv \frac{2\pi a^2 B_\omega^2}{\mu_0} \tag{3.11}$$

$$f(ka) \equiv \sqrt{2} \left(\frac{\mathrm{ber}_1(ka)\mathrm{bei}_1'(ka) - \mathrm{ber}_1'(ka)\mathrm{bei}_1(ka)}{\mathrm{ber}_0^2(ka) + \mathrm{bei}_0^2(ka)} \right). \tag{3.12}$$

The applied RMF torque thus scales as B_ω^2, and depends on the degree of penetration, represented by the function f(ka)/ka. The resistive torque is

$$T_\eta = 2\pi \int_0^a \nu_\perp n m_e \omega_e r^3 dr = \left(\frac{\lambda^2}{2\gamma^2} \right) \frac{\omega_e}{\omega} T_0 \tag{3.13}$$

where $\gamma \equiv \omega_{ce}/\nu_{ei}$ is the magnetization parameter in the RMF and $\lambda \equiv a/\delta$ is a penetration parameter. The two torques are plotted in Fig. 3.4 for various values of ω_e/ω. For large λ, there can be three solutions to $T_{RMF} = T_\eta$. The lowest crossing is not shown and is of no interest. The other two crossings correspond to "partial" and "full" penetration cases. Analytic work by Hoffman[12], and further numerical work by Milroy[13], has shown that for the case of an FRC in a flux conserver, the partially penetrated case is stable even if the RMF can supply enough torque to go over the "peak" in the resistive curve and reach the fully penetrated case. This partially penetrated solution is particular to the equilibrium constraints of an FRC in a flux conserver, as follows. Assuming that the temperature remains constant, as more RMF torque is applied than needed for the partially penetrated equilibrium, the FRC expands radially, contracts axially, and increases in density. The resistive friction increases even faster than the RMF torque, returning the equilibrium to the partially penetrated solution. The opposite occurs when the RMF torque decreases; the FRC shrinks

radially, expands axially, and decreases in density. This process can only be fully modeled numerically. For most RMF-driven FRCs, the equilibrium ka will be large. In the large ka limit, the following approximations apply:

$$\begin{aligned} E_z &\approx \omega\sqrt{\frac{2a}{r}}\delta^* \exp\left(\frac{r-a}{\delta^*}\right)B_\omega \\ B_r &\approx \frac{E_z}{\omega r} \\ B_\theta &\approx 2\sqrt{\frac{a}{r}}\exp\left(\frac{r-a}{\delta^*}\right)B_\omega \\ T_{RMF} &\approx \left(1-e^{-2a/\delta^*}\right)\frac{\delta^*}{a}T_0 \end{aligned} \tag{3.14}$$

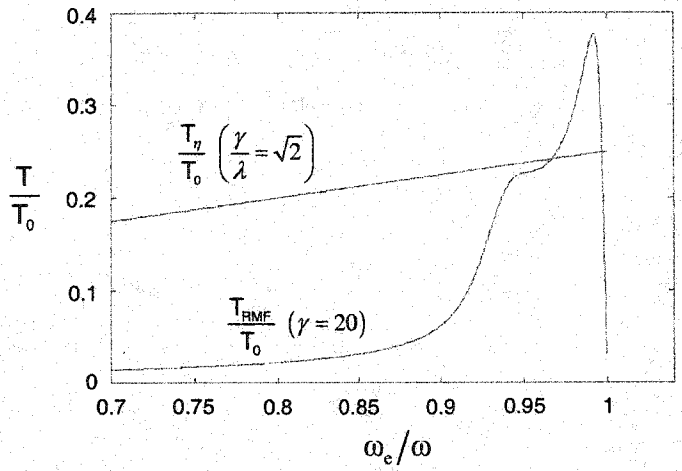

***Figure 3.4**: Normalized RMF and Frictional Torque. Plotted for typical TCS values of $\lambda = 20$ and $\gamma/\lambda = \sqrt{2}$*

The RMF current drive efficiency is characterized by the parameter ζ, defined as the ratio of the driven toroidal current to the maximum possible current (if all electrons were rotating at ω):

$$\zeta \equiv \frac{2B_e/\mu_0}{0.5\langle n\rangle e\omega r_s^2}. \tag{3.15}$$

The maximum achievable temperature is at $\zeta = 1$, dictated by pressure balance to be

$$T_{\max}/B_e = 12.5\langle\beta\rangle\zeta\omega r_s^2. \tag{3.16}$$

In practice, the plasma temperature in TCS is lower than the maximum achievable temperature because of impurity radiation losses.

For the FRC flux to be in steady state, the azimuthal electric field must be zero everywhere. Since the RMF does not penetrate to the internal field lines, an inward radial flow provides a $v_r \times B_z$ Lorentz force to balance the resistive drag on the inner field plasma. This radial flow could be sustained through circulation at the ends of the FRC, which extend beyond the RMF antennas, or by ionization of particles which are then driven inward by the $\langle v_z \times B_\theta \rangle$ RMF force. Schematics of these two flow patterns are shown in Fig. 3.5. In numerical simulations performed by Milroy[13], pressure is forced to be a flux surface quantity and a radial flow develops as shown in Fig. 3.6. In these simulations, the ion azimuthal rotation has been forced to zero. It is not clear whether this would be a fluid flow or simply an electron flow; in the latter case, oppositely directed toroidal fields would develop at the ends of the FRC. Future experiments are planned for the TCS upgrade to search for evidence of toroidal fields.

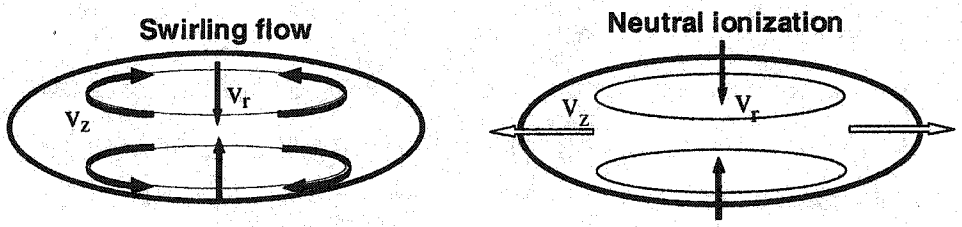

***Figure 3.5**: Possible Radial Flow Patterns.*

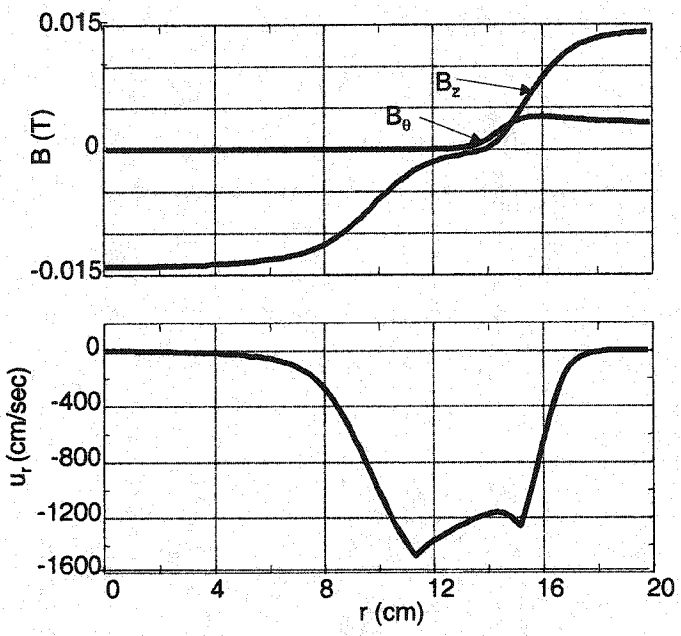

***Figure 3.6**: Numerical Simulations of Radial Flow.*

3.2 Free Ion Model

The previous model solved for the penetration of a rotating magnetic field into a plasma column by assuming stationary ions and rigidly rotating electrons. To study the forces acting on the ions and the resulting ion motion, a much simpler model is used. Rather than self-consistently solving for the field strength, the field is assumed to be given at a specific radius. The two-fluid equations can then be solved. These equations are inherently coupled; in this section, various assumptions are made to decouple the electron and ion equations in order to find a steady-state solution for the ion azimuthal velocity. In Sec. 9.1, a nonlinear least-squares numerical solver is used to find solutions for the fully coupled two-fluid equations.

Assume that the RMF field at a specified radius is given by some fixed value:

$$\boldsymbol{B} = B_r \cos(\omega t - \theta)\hat{\boldsymbol{r}} + B_\theta \sin(\omega t - \theta)\hat{\boldsymbol{\theta}} + B_z \hat{z}\,. \tag{3.17}$$

Hereafter any term with a tilde is an oscillating quantity, represented as a complex quantity and multiplied by $e^{i(\omega t-\theta)}$. For example,

$$\boldsymbol{B}=\tilde{B}_r\hat{\boldsymbol{r}}-i\tilde{B}_\theta\hat{\boldsymbol{\theta}}+B_z\hat{\boldsymbol{z}}. \tag{3.18}$$

Using Faraday's law $(\nabla\times\boldsymbol{E}=-\partial\boldsymbol{B}/\partial t)$ and neglecting any axial derivatives, the electric field is found to be

$$\boldsymbol{E}=E_r(r)\hat{\boldsymbol{r}}+r\omega\tilde{B}_r\hat{\boldsymbol{z}}. \tag{3.19}$$

The electron and ion fluid equations of motion, including the effects of neutral collisions (υ_n) and fueling (s), are

$$\begin{aligned} nm_e\frac{D\mathbf{v}_e}{Dt}&=-ne\left(\boldsymbol{E}+\mathbf{v}_e\times\boldsymbol{B}\right)-\nabla p_e-nm_e\upsilon_{ei}\left(\mathbf{v}_e-\mathbf{v}_i\right)-nm_e\upsilon_{en}\mathbf{v}_e-m_e s\mathbf{v}_e \\ nm_i\frac{D\mathbf{v}_i}{Dt}&=ne\left(\boldsymbol{E}+\mathbf{v}_i\times\boldsymbol{B}\right)-\nabla p_i+nm_e\upsilon_{ei}\left(\mathbf{v}_e-\mathbf{v}_i\right)-nm_i\upsilon_{in}\mathbf{v}_i-m_i s\mathbf{v}_i \end{aligned} \tag{3.20}$$

It is assumed that the neutral particles involved in the momentum transfer and fueling have no directed velocities. The convective derivative in cylindrical coordinates is

$$\frac{D\mathbf{v}}{Dt}=-\frac{\mathrm{v}_\theta^2}{r}\hat{\boldsymbol{r}}+\left(\mathrm{v}_r\frac{\partial\mathrm{v}_\theta}{\partial r}+\frac{\mathrm{v}_\theta\mathrm{v}_r}{r}\right)\hat{\boldsymbol{\theta}}+\left(\mathrm{v}_r\frac{\partial\tilde{\mathrm{v}}_z}{\partial r}-i\frac{\mathrm{v}_\theta}{r}\tilde{\mathrm{v}}_z+i\omega\tilde{\mathrm{v}}_z\right)\hat{\boldsymbol{z}}. \tag{3.21}$$

For reference, the components of $\left(\mathbf{v}\times\boldsymbol{B}\right)$ for the fields given above are

$$\left(\mathbf{v}\times\boldsymbol{B}\right)=\left(\mathrm{v}_\theta B_z-\left\langle\tilde{\mathrm{v}}_z\tilde{B}_\theta\right\rangle\right)\hat{\boldsymbol{r}}+\left(\left\langle\tilde{\mathrm{v}}_z\tilde{B}_r\right\rangle-\mathrm{v}_r\tilde{B}_z\right)\hat{\boldsymbol{\theta}}+\left(\mathrm{v}_r\tilde{B}_\theta-\mathrm{v}_\theta\tilde{B}_r\right)\hat{\boldsymbol{z}}. \tag{3.22}$$

Because this model neglects second order modes and higher, then whenever two oscillating quantities are multiplied together only the steady time-averaged component, denoted by angle brackets $\langle\ \rangle$ and defined in Eq. (3.5), remains. Now, assuming that ∇p is strictly radial, the ion momentum equation can be explicitly written as

$$\hat{r}: -m_i \frac{\mathrm{v}_{i\theta}^2}{r} = e\left(E_r + \mathrm{v}_{i\theta} B_z - \left\langle \tilde{\mathrm{v}}_{iz} \tilde{B}_\theta \right\rangle\right) - \frac{1}{n}\frac{\partial P_i}{\partial r} + m_e \upsilon_{ei}\left(\mathrm{v}_{er} - \mathrm{v}_{ir}\right) - m_i \mathrm{v}_{ir}\left(\upsilon_{in} + \frac{s}{n}\right)$$

$$\hat{\theta}: m_i\left(\mathrm{v}_{ir}\frac{\partial \mathrm{v}_{i\theta}}{\partial r} + \frac{\mathrm{v}_{i\theta}\mathrm{v}_{ir}}{r}\right) = e\left(\left\langle \tilde{\mathrm{v}}_{iz}\tilde{B}_r \right\rangle - \mathrm{v}_{ir}B_z\right) + m_e\upsilon_{ei}\left(\mathrm{v}_{e\theta} - \mathrm{v}_{i\theta}\right) - m_i\mathrm{v}_{i\theta}\left(\upsilon_{in} + \frac{s}{n}\right)$$

$$\hat{z}: m_i\left(i\omega\tilde{\mathrm{v}}_{iz} - i\frac{\mathrm{v}_{i\theta}}{r}\tilde{\mathrm{v}}_{iz} + \mathrm{v}_{ir}\frac{\partial \tilde{\mathrm{v}}_{iz}}{\partial r}\right) = e\left(\tilde{E}_z + \mathrm{v}_{ir}\tilde{B}_\theta - \mathrm{v}_{i\theta}\tilde{B}_r\right) + m_e\upsilon_{ei}\left(\tilde{\mathrm{v}}_{ez} - \tilde{\mathrm{v}}_{iz}\right) - m_i\tilde{\mathrm{v}}_{iz}\left(\upsilon_{in} + \frac{s}{n}\right)$$

(3.23)

To understand some of the basic physics behind these equations, we will first expand upon the assumptions made by Hugrass[10]. Neglect the radial velocity and the friction terms in the ion axial equation. This is justified if electron and neutral friction forces are small relative to the RMF force:

$$\frac{\left(\upsilon_{ie} + \upsilon_{in} + s/n\right)}{\omega} << 1. \tag{3.24}$$

This has the important effect of decoupling the ion and electron axial equations. The ion axial velocity also becomes independent of the azimuthal velocity, allowing the simple solution

$$\tilde{\mathrm{v}}_{iz} = -ir\frac{e\tilde{B}_r}{m_i} = r\left(\frac{eB_r}{m_i}\right)\sin(\omega t - \theta). \tag{3.25}$$

Note that the ion axial velocity lags E_z and B_r by 90 degrees. This is intuitive; a frictionless mass oscillates inductively when subject to a periodic force. The ion azimuthal equation (again neglecting radial velocity but keeping friction terms) is

$$0 = e\left\langle \tilde{\mathrm{v}}_{iz}\tilde{B}_r \right\rangle + m_e\upsilon_{ei}\left(\mathrm{v}_{e\theta} - \mathrm{v}_{i\theta}\right) - m_i\left(\upsilon_{in} + s/n\right)\mathrm{v}_{i\theta}. \tag{3.26}$$

The $\left\langle \tilde{\mathrm{v}}_{iz}\tilde{B}_r \right\rangle$ term is the RMF azimuthal force directly on the ions. Using our purely inductive solution (3.25) for the axial velocity, this drive term is zero. The ion rotation speed is then a balance between friction with faster electrons and drag with stationary neutrals. Defining the ion-electron momentum collision frequency $\upsilon_{ie} \equiv \left(m_e/m_i\right)\upsilon_{ei}$, the ratio α of the ion to electron azimuthal velocity is

$$\alpha \equiv \frac{\mathrm{v}_{i\theta}}{\mathrm{v}_{e\theta}} = \left(1 + \frac{\left(\upsilon_{in} + s/n\right)}{\upsilon_{ie}}\right)^{-1} \tag{3.27}$$

where ν_{in} is the charge-exchange momentum transfer frequency and s is the ionization source rate. Although this model is not applicable to FRCs because it does not self-consistently solve for the equilibrium, the result in (3.27) is still useful. As long as the RMF does not exert a significant azimuthal force directly on the ions, then the ion rotation speed must be a balance between electron and neutral friction.

The particle confinement time is defined as

$$\tau_N \equiv \frac{n}{s - dn/dt}. \tag{3.28}$$

In steady state, $dn/dt = 0$, and thus Eq. (3.27) can be expressed in terms of the particle confinement time

$$\alpha = \left(1 + \frac{(\upsilon_{in} + 1/\tau_N)}{\upsilon_{ie}}\right)^{-1} \tag{3.29}$$

From this equation, one can see why ion spin-up has received so much attention. As machines improve, having fewer neutrals and longer confinement times, the drag terms diminish and the ions will reach an appreciable fraction of the electron rotation velocity.

The previous analysis found the steady-state ion azimuthal velocity. To estimate the spin-up time, we must solve a linear first-order differential equation describing the force balance between electron and neutral friction:

$$\frac{d\omega_i(t)}{dt} = \upsilon_{ie}\left(\omega_e - \omega_i(t)\right) - \upsilon^* \omega_i(t), \tag{3.30}$$

where υ^* is the net ion momentum transfer frequency, in this model consisting of $\upsilon^* \equiv \upsilon_{in} + 1/\tau_N$. The solution to Eq. (3.30) is

$$\omega_i(t) = \omega_e \left(1 + \frac{\upsilon^*}{\upsilon_{ie}}\right)^{-1} \left(1 - e^{-t/\tau_{su}}\right), \tag{3.31}$$

where the spin-up time constant τ_{su} is defined as

$$\tau_{su} \equiv \left(\upsilon_{ie} + \upsilon^*\right)^{-1}. \tag{3.32}$$

The addition of neutrals lowers the steady-state ion rotation velocity but makes the spin-up time to this lower velocity shorter. Typical values in TCS are $\upsilon_{ie} \approx 1\times10^4$ s^{-1} and $\upsilon^* \approx 4\times10^4$ s^{-1}, leading to a spin-up time of only 20 μs.

3.3 Review of Previous RMF Research

There has been considerable theoretical research on RMF current drive. The idea of using a transverse rotating magnetic field to drive azimuthal electron current was first explored by Blevin and Thonemann[14] in 1962. They solved the relevant Ohm's law $E = \eta j + (j \times B)/ne$ by neglecting the resistive term and solving for the hall current. This approach was pursued further by Jones and Hugrass[11] in 1981, who considered the effect of the two terms in Ohm's law separately. They found a resistive solution by assuming that the ηj term dominates with the hall term as a small linear correction. This solution is characterized by partial penetration of the RMF to a depth δ^* greater than the simple resistive skin depth δ. They also considered a second case where the hall term dominates and the resistive term is a small linear correction. This solution leads to full penetration of the rotating field and near-synchronous electron. In 1982, Hugrass[10] expanded upon the fully-penetrated solution to allow for ion rotation. In 1983, Hugrass and Jones[15] solved for the particle trajectories in a fully-penetrated RMF and found that the particles can indeed have closed orbits. In 1986 Hugrass[16] considered the effect of higher-order harmonics in the rotating field produced by realistic antenna geometries. He found that field errors can significantly degrade the current drive efficiency. In 1989 Bellan[17] solved for the particle orbits in a fully-penetrated RMF using Hamiltonian-Lagrangian analysis and found that the electrons are confined in a potential well, while the ions are confined to the conventional FRC flux surfaces. In 1996 Ohnishi[18] expanded the fully-penetrated two-fluid model of Hugrass to include the effects of radial flow. He considered the particular case of central fueling at the field null. In 1998 Hoffman[19] considered the effect of a fully-penetrated RMF on an FRC, with $B_z \gg B_\omega$. In the same year, Clemente[20] proposed an

interesting scheme of counter-rotating magnetic fields, one of which would drive the electrons and the other the ions, as a solution to the problem of ion spin-up. In 1999 Milroy[21] presented the first two-dimensional numerical solution for RMF current drive in an FRC, although this first work assumed a fixed, uniform ion density. This first simulation found complete RMF penetration for $\gamma_c = 1.12\lambda\left[1 + .12(\lambda - 6.5)^4\right]$. This simulation was improved[13] in 2000 to a fully two-dimensional MHD model, including the effects of a flux conserver. The model also included some quasi-three-dimensional effects typical of the FRC equilibrium, such as the average β condition and the equilibration of pressure along a flux line. This model assumed that the n = 0 component of the ion azimuthal velocity was zero (no ion spin-up), and enforced an arbitrary temperature clamp to agree with experiments. However, this simulation was very successful in predicting the partial penetration of RMF into an FRC even when $\gamma > \gamma_c$. A second improvement[22] of this code in 2001 included an edge density pedestal to look at the effects of wall out-gassing. The RMF is found to apply a strong radially- inward force, but if the wall fueling rate is sufficiently high then the RMF loses its drive. The numerical models agree well with an analytic model of RMF current drive in an FRC subject to equilibrium constraints, presented by Hoffman[12] in 2000. In 2001 Steinhauer[23] considered a viscous momentum sink for the ions using classical (Braginskii) shear viscosity as an explanation for the observed rotation results, and in 2002 he proposed end-shorting of the radial electric field as an ion braking mechanism[24].

Unfortunately, there has been considerably less experimental research on RMF current drive. The majority of research in the 1980's was performed in a series of rotamak experiments at Flinders University, Australia. This research is summarized in a review paper by Jones[25]. The rotamak is a spherical compact toroid with no external flux conserver. The RMF is fully penetrated and drives toroidal current until the plasma separatrix reaches the wall. The physics of neutral particles and wall interactions are very important. These experiments reached toroidal currents of over 10

kA with input RMF power of 300 kW at 0.5 MHz. Electron temperatures were typically ~35 eV. A similar experiment was performed at UCLA in the RACETRACK device[26]. A weak, 10- kW, 485-kHz RMF was applied along with an axial field to form a rotamak-type FRC. Again, there was no effective flux conserver. The first real RMF-driven FRC in a flux conserver was created in the STX experiment at the University of Washington[27]. This had a 60-kW IGBT supply that generated a 20-G RMF field at 350 kHz. The RMF was observed to penetrate only to the field null even though $\gamma > \gamma_c$. STX reported $T_e \approx 40$ eV, cold ions, a very low separatrix density, and a flat field profile at the null that is inconsistent with the rigid rotor model. These results were explained by Hoffman's analytic work and Milroy's numeric model that include the unique equilibrium constraints of the FRC. However, the STX experiment had difficulty maintaining current drive in steady-state. This may have been because of three-dimensional flow effects. The RMF antennas were relatively long compared with the length of the flux conserver and may have inhibited the development of a steady radial flow pattern.

Chapter Four

The TCS Experiment

The goal of the Translation, Confinement, and Sustainment (TCS) experiment is to study the physics of RMF current drive, in both pre-existing FRCs as well as RMF-formed FRCs. The TCS experiment[28] is an improvement over previous RMF current-drive experiments in that it has a multi-megawatt RMF power supply, has a large flux conserver radius (47-cm), and has the capability to form a high-quality conventional FRC in a separate chamber and then translate it into the RMF section. The physics of the plasmas formed in the TCS device are less dominated by wall interactions, neutral particles, and impurities than in previous RMF current-drive experiments, although it will be seen that these effects still play a significant role.

This chapter describes the TCS experimental setup. Sec. 4.1 briefly describes the TCS coil set and vacuum vessel. The RMF power supply, built by Los Alamos National Laboratory, is described in Sec. 4.2. Sec. 4.3 summarizes the diagnostics on TCS, with the exception of the Doppler spectroscopy diagnostic which will be presented in Ch. 5. Emphasis is placed on how these diagnostics will contribute to the study of plasma rotation.

4.1 The TCS Device

The TCS experiment consists of three sections, as shown in Fig. 4.1. The formation and translation sections are built from the LSX/mod device used in the TRAP experiments[29]. The formation section is used to form high-temperature FRCs using the conventional FRTP technique. The translation section then compresses and accelerates the FRC into the larger sustainment section. After several reflections, the FRC reaches a stable equilibrium in the sustainment section but has expanded to a much lower density. Rotating magnetic field current drive is then applied in an attempt to sustain the poloidal flux. Additionally, the TCS experiment can be operated in an RMF startup

mode, where the formation and translation sections are used solely as a preionization source for the sustainment section. In this mode, the RMF system drives enough toroidal current to reverse the bias field and form an FRC in the sustainment section from scratch, avoiding the FRTP technique altogether.

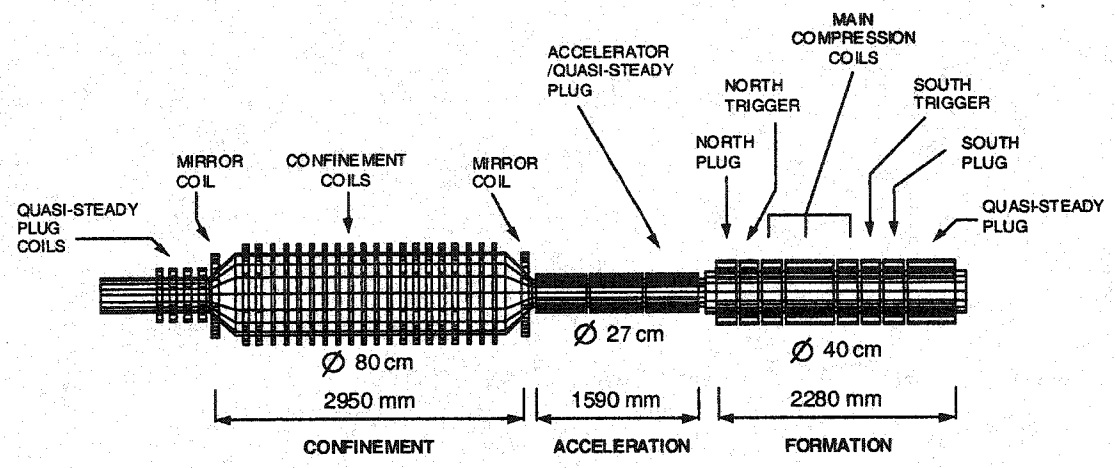

Figure 4.1: *The TCS Device and Coil Set*

The formation section is a 40-cm diameter quartz vacuum tube surrounded by eight 46-cm diameter axial field coils. All coils are individually powered by 43-kJ, ±25 kV high voltage modules from the original LSX experiment[7]. A high temperature FRC can be formed using the conventional FRTP technique. Using the "slingshot" programmed formation technique, a typical FRC with 5 mWb of poloidal flux and density of 10^{21} m^{-3} can be formed in a one tesla axial magnetic field.

The translation section is a 27-cm ID quartz vacuum tube originally used in the TRAP experiment. Three 30-cm diameter 3-turn coils are independently powered by similar high-voltage modules as in the formation section. The initial temperature in the formation section is converted into kinetic energy during the transit, but conservation of enthalpy dictates that most of the temperature is recovered after the first reflection in the sustainment chamber[30].

The sustainment section is a 2.5-m long, 80-cm diameter quartz vacuum vessel. The quartz tube consists of two 1.25 meter sections joined in the center by a plastic ring covered with a thin layer of stainless steel with ports for midplane diagnostics. The quartz tube is surrounded by twenty 47-cm radius 56-turn coils. The center 14 coils are connected in parallel to act as the main flux conserver and are powered by a 4-mF, 10-kV capacitor bank. Three coils on each end of the center flux conserver are connected in parallel and serve as an independently programmable edge field. Each end of the sustainment tube tapers down to 27-cm diameter via 45-degree conical sections made of stainless steel bonded to fiberglass. The upstream end attaches to the acceleration section while the downstream end terminates in a stainless plug tube. Each cone has a single 35-cm radius mirror coil, while the downstream plug has four 40-turn plug coils connected in parallel. Early on in the translation experiments, it was noticed that the reflection of the FRC off of the downstream mirror and stainless steel cone introduced a large number of impurities into the plasma. To minimize this problem, a tantalum insert has been placed over the downstream cone. Even with the addition of this insert, translated FRCs still pick up silicon impurities through interaction with the quartz vacuum vessel.

The TCS device does not have any wall-conditioning capability with the exception of a helium glow-discharge system. However, since the quartz tube walls are non-conducting, it does not appear that the glow-discharge is effective at removing adsorbed gases. Additionally, the TCS device does not have a pre-ionization source in the sustainment chamber. Even when operated in RMF-startup mode, preionized gas must still be introduced from the formation section. These two factors make precise control of the particle inventory impossible. The neutral density in the confinement chamber will be estimated in Ch. 7.

4.2 RMF System

A transverse rotating magnetic field is created in the TCS sustainment section by a set of four Helmholtz-type saddle antennas, as shown in Fig. 4.2. These antennas are 7.62-cm diameter copper pipes that run horizontally exterior to the axial field coils at a radius of 54-cm. This arrangement effectively generates a dipole field, but minimizes the field errors in the vacuum chamber. The analytic vacuum field solution for the TCS antenna system is shown in Fig. 4.3. The RMF antennas are 1.5 m long, considerably shorter than the 3-m confinement chamber to allow for three-dimensional flow effects at the ends of the FRC. The antennas are hooked up in pairs, with each pair having a combined inductance of 1.6 μF. This antenna arrangement can generate a vacuum field of 6.4 G/kA of antenna current; the field is typically 40-60 Gauss. The plasma resistance dominates the circuit resistance in determining the decay of the antenna current, limiting the pulse length to about 2 ms.

The RMF antennas are powered by a multi-megawatt tube-driven RF supply built by Los Alamos National Laboratory[31]. A 200-μF main capacitor bank is charged before the shot, typically to 14 kV. A waveform generator in the control room then sends a train of voltage pulses to a deck of Eimac triodes. These triodes control a set of six parallel Machlett 8618 magnetically beamed triodes that switch the current through a 1:1 air-core transformer primary. The transformer secondary is connected to a tank circuit, which consists of RF capacitors and the RMF antennas. By varying the amount of capacitance, the tank circuit can be tuned to oscillate at the desired frequency. TCS has been operated over a range of RMF frequencies from 258 kHz ($\omega=1.6\times10^6$ s^{-1}) to 81 kHz ($\omega=5\times10^5$ s^{-1}). At lower frequency, the circuit impedance ωL is lower and stronger transverse fields can be applied. The RF tube system can deliver a maximum of ~5 MW of absorbed power to the plasma.

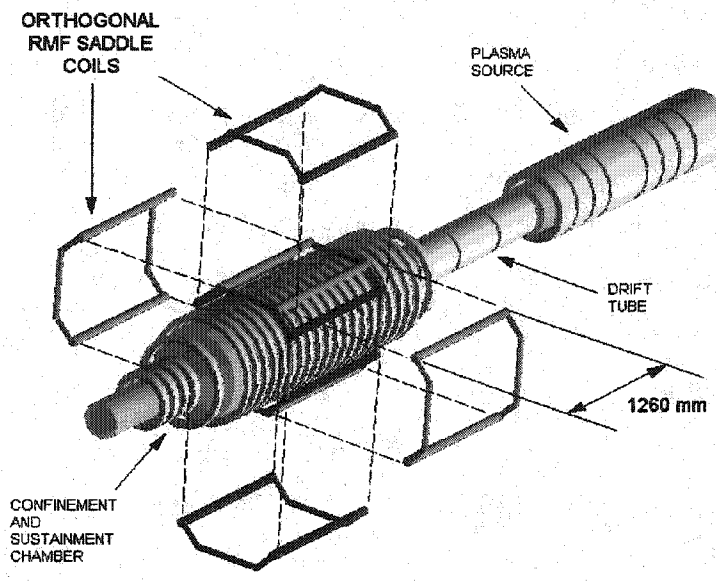

Figure 4.2: *RMF Antennas. Two pairs of Helmholtz-type saddle antenna; each are 7.6-cm diameter and at 54-cm radius.*

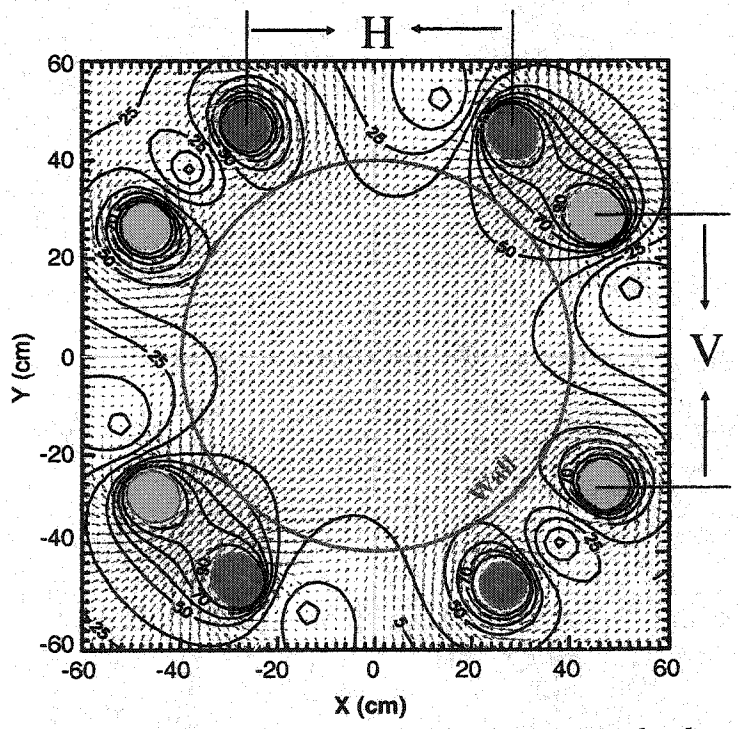

Figure 4.3: *RMF Vacuum Field. Vacuum field solution is solved numerically at one instant in time. The quartz vacuum tube is shown at 40-cm radius. The flux-conserver coils at 47-cm are not shown.*

4.3 General Diagnostics

The TCS experiment has a set of 39 excluded flux arrays at various axial locations along with several measurements of the external field B_e. These allow determination of the excluded flux radius, equivalent to the separatrix radius if there is no open field-line pressure, at each of the loop locations. Of course, this is an average value of the separatrix at each axial location; rotational modes can cause the local separatrix to exceed the average value. The FRC length, volume, and total energy are also calculated using the flux array.

The plasma temperature in the RMF-formation mode is low enough that the magnetic field profile can be measured directly with an internal magnetic probe. The probe is inserted radially at the axial midplane. The probe contains 31 individual flux loops, all oriented in the same plane. The loops are wound inside a thin electrostatic shield enclosed in a beryllium oxide tube 42-cm long and 3-mm in diameter. The probes are spaced at 2-cm intervals from r = 0 to r = 20 cm radius, and at 1-cm intervals from r = 20 to r = 40 cm. The probe has a time resolution of 100 ns. The probe can be rotated to measure either the axial or toroidal field or a combination of both. The magnetic field profile is used to reconstruct the plasma pressure and current density profiles.

A double-pass heterodyne Mach-Zender CO_2 interferometer is located at the axial midplane and measures line-of-sight electron density $\int_{-r_w}^{r_w} n_e(r)dl$ at zero impact parameter. Based on previous FRC experience, the total temperature is assumed to be uniform throughout the plasma. With this assumption, the total temperature can be deduced from the interferometer and internal magnetic probe data, as described in Ch. 7.

A floating double Langmuir probe is located at the axial midplane and is inserted a few cm into the plasma. The probe jacket is beryllium oxide while the probe

tips are made of tungsten wire. The probe typically measures ion saturation current, which is used to measure the edge electron density. Although the probe voltage is not swept during a shot, the probe bias can be changed shot-to-shot to estimate the electron temperature. This information is used extensively in interpreting the emission diagnostics.

TCS has two wideband silicon photodiode bolometers[32] that ideally detect all incident photons from line radiation as well as plasma bremsstrahlung emission. The bolometers, both located at the axial midplane with zero impact parameter, measure the chord-integrated total radiated power $\int_{-r_w}^{r_w} P_{rad}(r)dl$. Individual impurity lines are measured with three photomultiplier-tube monochrometers. A Jarrell-Ash 0.5-meter visible spectrometer views the plasma at the axial midplane with zero impact parameter. This spectrometer typically monitors Si III emission at 455.262 nm. Two ultraviolet spectrometers are lens-coupled to the plasma near the midplane at zero impact parameter. A McPherson 0.3-m monochrometer typically monitors O III emission at 326.53 nm from the colder RMF-startup plasmas and helium-like C V emission at 227.089 nm from the hotter translated plasmas. An Acton 0.2-m monochrometer monitors C III emission at 229.687 nm. Although none of the monochrometers are absolutely calibrated, they can be used in doping experiments to estimate the impurity content of the FRC. The Si III signal in particular is a useful indication of whether a rotational mode has caused wall contact and ablation of the quartz tube wall.

The TCS experiment has several arrays of visible light diagnostics at the axial midplane, as shown in Fig. 4.4. A radial array of eight Dα (656.103 nm) detectors views the plasma in 5-cm increments from y = 0 to y = 35 cm impact parameter. The system is absolutely calibrated to give (chord-integrated) photons/m^2/s. As described in Ch. 7, the chordal measurements can be Abel-inverted to find the neutral emission profile. From this, the neutral density, ionization rate, and charge-exchange rate can all

be calculated. A 34-chord tomography system is also installed near the axial midplane. Visible light collected by the system passes through a pair of gel filters with a bandpass of 500-600 nm. This region of the spectrum is relatively free of impurity line radiation and is hoped to be dominated by plasma bremsstrahlung emission. The tomographic data is inverted using a modal algorithm, where the structure is limited to a few radial and azimuthal modes. Ideally, this is representative of the plasma density profile, although impurity line radiation may contaminate the signal. Actual spectra taken through the filters indicate[33] that the ratio of continuum bremsstrahlung radiation to impurity line radiation is only about 44%, so the tomographic inversion is not used to determine the plasma density profile in this thesis. However, it does provide an excellent picture of the rotation mode structure and frequency.

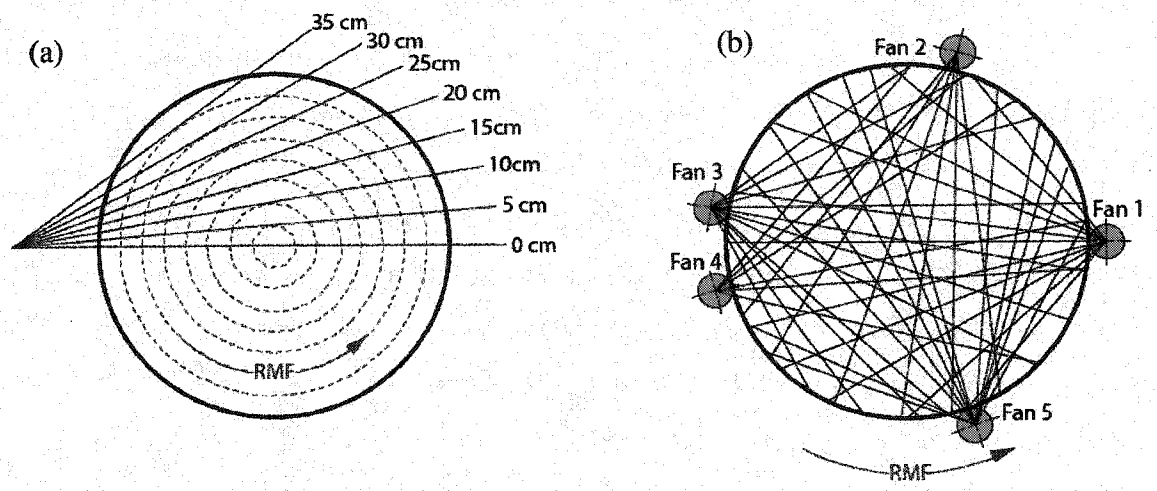

***Figure 4.4**: Visible Light Emission Arrays. (a) 8-chord D-α array. Light is collected by 12-mm diameter f/3.5 collimating lenses, focused onto fiber optics, and passed through a 10-nm wide filter. The system collects both D-α and H-α emission. (b) 34-chord visible light tomography array.*

Chapter Five

Doppler Spectroscopy Diagnostic

Doppler spectroscopy is a standard diagnostic used to measure the parallel velocity of a radiating species. If a radiating particle is moving relative to an observer, then the radiation wavelength and frequency will appear Doppler shifted to the observer. The Doppler effect equation for non-relativistic ($v \ll c$) motion is

$$\frac{\Delta\lambda}{\lambda_o} = \frac{v}{c}\cos\theta, \tag{5.1}$$

where $\Delta\lambda$ is the shift in observed wavelength from the rest wavelength λ_o, v is the velocity of the emitter relative to the observer, c is the speed of light in the medium, and θ is the angle between the velocity vector of the emitting particle and the observer's line of sight, as shown in Fig. 5.1. Since the natural wavelength of bound-bound transition line radiation for most plasma impurities is known with great precision, the line-of-sight drift velocity of these impurities can be deduced from the shift in observed wavelength of the line radiation.

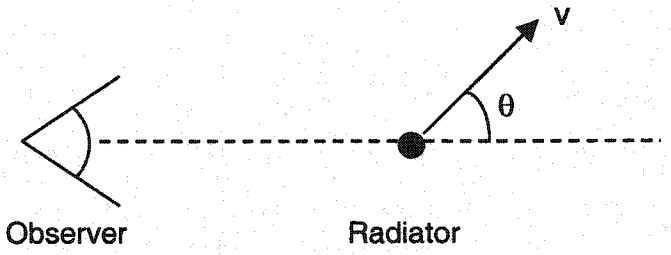

Figure 5.1: *The Doppler Effect*

There are several complications when making Doppler spectroscopy measurements. First, only neutrals and ions with bound electrons emit spectral line radiation; therefore, the Doppler effect cannot be used to determine the velocity of fully ionized atoms or free electrons. The majority species in TCS is deuterium, which for the most part is fully ionized inside the separatrix. In order to study plasma rotation, spectral lines from partially ionized impurities such as carbon or silicon are used

instead. These heavier impurities may not have the same drift velocity or temperature as the main plasma species. This concern will be addressed in Sec. 6.1. Second, spectroscopy is inherently a chord-integrated measurement. As with all such measurements, the data must be spatially inverted to obtain a radial profile. Finally, all spectrometers have imperfect optics. Aberration and coma broaden a spectrally narrow line. The spectrometer output for an input delta function is the instrument profile, sometimes referred to as the point spread function (PSF). Deconvolution is the process of removing the instrument function from the experimentally observed spectrum. The data presented in this thesis has been both spatially inverted and spectrally deconvolved, as described in this chapter.

To measure the ion azimuthal velocity, TCS is equipped with a multi-chord Intensified Charge-Coupled Device (ICCD) spectrometer. This takes a snapshot of the spectral distribution of line radiation at a single point in time but at six chords, allowing determination of the spatial profile of the plasma velocity. This chapter summarizes the experimental setup of the ICCD spectrometer, as well as the calibration, deconvolution, and spatial inversion techniques used to analyze the data.

5.1 ICCD Spectrometer

The Intensified Charge-Coupled Device (ICCD) spectroscopy system used on TCS will be described in this section, although more detail can be found elsewhere[34]. A two-dimensional CCD chip provides both spectral and spatial resolution. The system can effectively resolve line radiation down to about a tenth of a pixel on the CCD. For a line at 500 nm this corresponds to 0.0025 nm, equivalent to the Doppler shift of a particle with 1.5-km/s velocity. The system has a reasonable efficiency over the range from 200 to 800 nm. The maximum gain is about 80 digital counts per photoelectron. A 25-μs exposure usually yields a good signal-to-noise ratio. Spatially, the system can collect light from six chords simultaneously.

Electromagnetic radiation emitted from the plasma is collected and collimated by 12-mm diameter, 42-mm focal length quartz plano-convex lenses. A fiber optic bundle is placed at the focal length of each lens. Each fiber bundle consists of seven individual 200-μm diameter UV fibers. At the input end of each fiber bundle, the seven fibers are in a hex-close-packed geometry, as shown in Fig. 5.2, to maximize the collecting area. At the output end, the fibers are randomly ordered into a single vertical line. This geometry allows the narrowest entrance slit to the spectrometer possible. The CCD chip is large enough to image all six bundles simultaneously. An example of a raw image of the C-III line at 229.687 nm is also shown in Fig. 5.2. The horizontal dimension on the CCD is converted to a wavelength while the vertical axis is the imaging axis along the slit height.

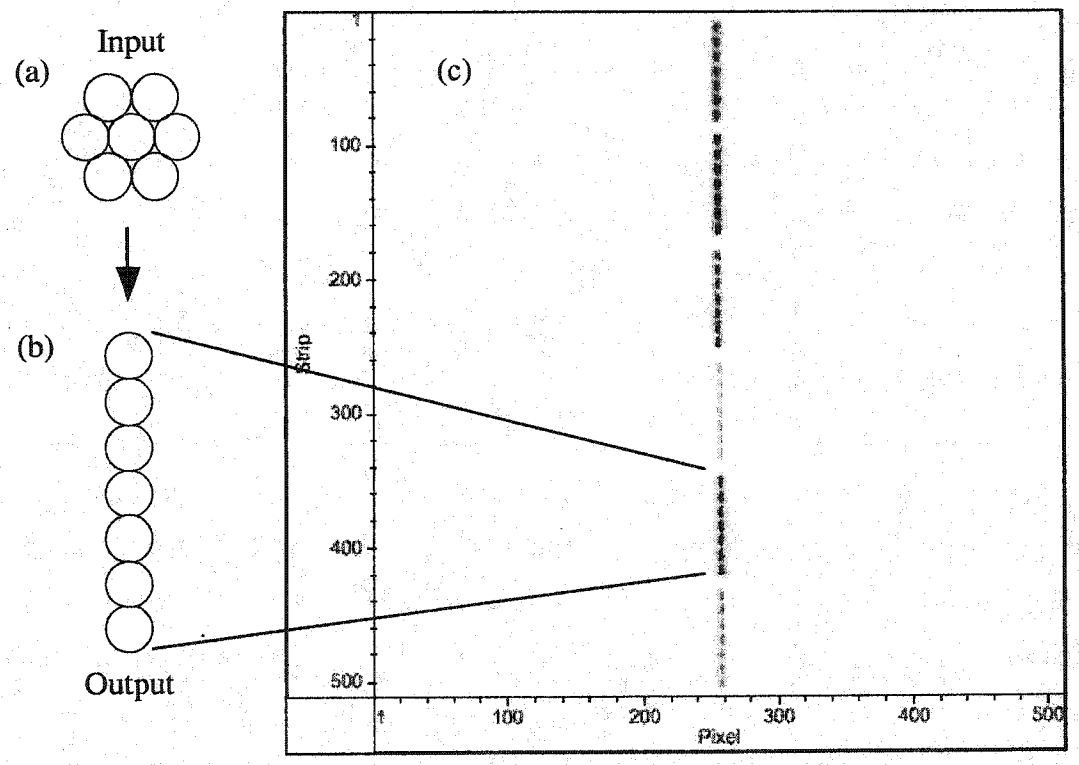

***Figure 5.2**: ICCD Fiber Optic Bundles and Raw Image. (a) Fiber bundle geometry at the light input end. (b) Fiber bundle geometry at the light output end. (c) Raw ICCD image of the C-III line at 229.687 nm in inverted grayscale.*

The six fiber bundles typically view the plasma near the axial midplane. The fibers have been arranged in a variety of fans, as shown in Fig. 5.3. For detailed velocity profiles, the fibers are positioned in a radial array, in 5-cm increments from y = 10 to y = 35 cm impact parameter.

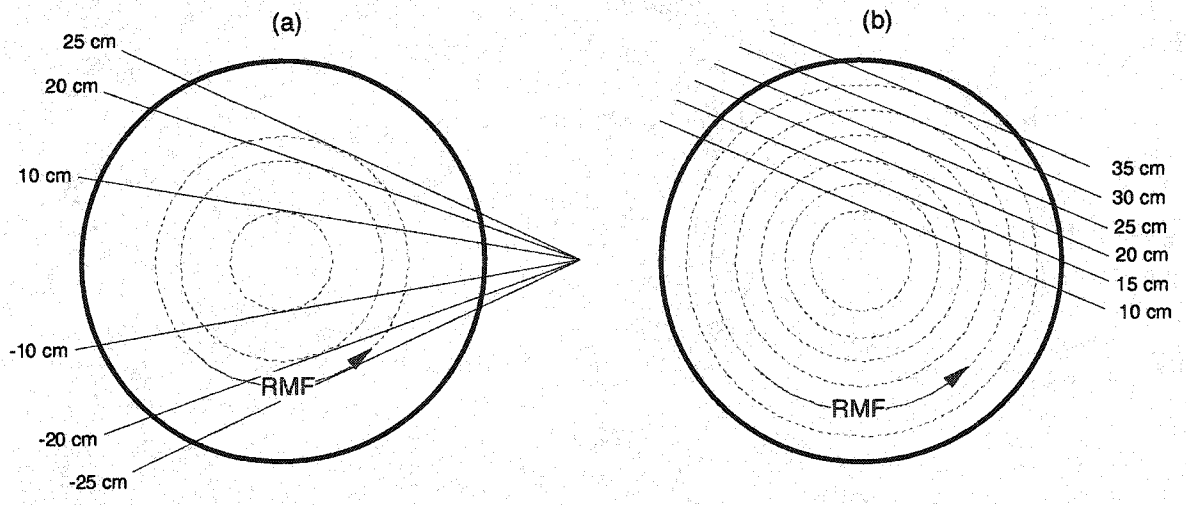

***Figure 5.3**: ICCD Fiber Optic Array Layouts. (a) Symmetric fan used for chord-integrated velocity measurements. (b) Radial fan used for Abel inversion.*

The spectrograph in the ICCD system is an Acton Research SpectraPro 500i Czerny-Turney type spectrograph. It has a focal length f of 500 mm and an aperture ratio of f/6.5. The spectrometer slit is typically 25-μm wide. Toroidal mirrors in the spectrometer provide the necessary horizontal (spectral) accuracy while maintaining sufficient vertical resolution to image six fibers simultaneously. The spectrometer has a stepper-motor controlled turret that holds three different 68 x 68 mm gratings. This allows both high spectral resolution and wide range because different gratings can be used for lines in different wavelength ranges. For Doppler effect studies, two high dispersion gratings are used, both with 1800 g/mm. One is a ruled grating with a blaze wavelength of 500 nm; the other is a holographic grating with a 250-nm blaze wavelength. Both gratings have a nominal dispersion of 0.9 nm/mm, equivalent to 0.022 nm per pixel and an 11.5-nm field of view.

A Princeton Instruments PI-MAX 512RB camera is located at the exit plane of the spectrometer. This camera contains a photocathode, microchannel plate (MCP), tapered fiber bundle, rear phosphor, and CCD chip. Incident photons are converted into electrons by an 18-mm diameter Gen-II photocathode with a relatively constant quantum efficiency of about 10% from ultraviolet wavelengths through the visible spectrum. The MCP is a slightly conducting glass plate with hundreds of thousands of 6-μm pores that can provide a maximum gain of about 560 electrons per incident photoelectron. The intensifier also acts as a very fast shutter. The intensifier is gated by switching the accelerating voltage between the photocathode and the MCP, as well as by bracketing the voltage across the MCP. Bracketing gives the intensifier a nearly flat on/off ratio of about 10^7:1, even for high-energy incident photons in the UV that can pass through the photocathode and strike the MCP directly. Because of this high on/off ratio, no mechanical shutter is needed. The rear phosphor is type P43 (Gd_2O_2S:Tb) with a decay time (down to 1%) of 3 ms. Light from the rear phosphor is brought to the CCD chip via a 1.27:1 reducing fiber-optic bundle. The CCD is a Thomson 7895 square array with 512 x 512 imaging pixels. The CCD pixel size is 19 μm, but because of the tapered fiber optic coupling, the spectrograph sees an effective pixel size of 24.13 μm. The effective field of view focused onto the CCD chip is then 12.4 x 12.4 mm. The CCD well capacity is 450,000 electrons per pixel. A thermoelectric cooler keeps the CCD at a stable –20° C to reduce the CCD dark current to a nominal value of eight electrons per pixel per second.

The PI-MAX camera is controlled by a Princeton Instruments ST-133A controller. This unit contains an A/D converter for the CCD array output as well as a Programmable Timing Generator (PTG) that gates the intensifier. The PTG has a nominal insertion delay of 25 ns. The ST-133A also controls the intensifier gain and the grating stepper-motor. A 16-bit, 100-kHz digitizer converts the CCD well charge to digital counts, with one count equaling about seven electrons. The data is pre-

processed by Roper Scientific Winspec software that arranges the CCD data back into its geometric order and applies basic grating equations to create a wavelength scale. Final processing is performed with MATLAB.

The ICCD system has not been absolutely calibrated. Based on the manufacturer specifications for the fiber optics, the gratings, and the photocathode[35], the total system sensitivity versus wavelength can be estimated, as shown in Fig. 5.4. By using different gratings, the spectrometer has a reasonable efficiency from 200 to 800 nm.

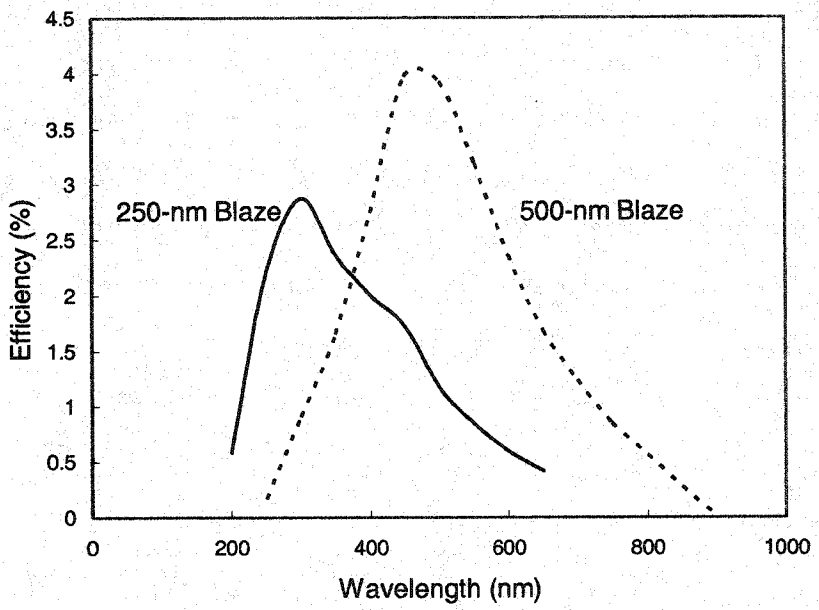

***Figure 5.4:** ICCD Total System Sensitivity*

5.2 Calibration

The first step in processing the raw ICCD image is to create a wavelength scale. The wavelength calibration is based on the Czerny-Turney grating equation:

$$\lambda = \frac{1}{kn}(\sin\alpha + \sin\beta) \tag{5.2}$$

where k is the diffraction order, n is the number of grooves per mm for the grating, α is the angle of the incident beam relative to the grating normal, and β is the angle of the

exit beam, as shown in Fig. 5.5. α and β are related to the inclusion angle γ, which is a property of the grating, by $\gamma = \beta - \alpha$. The wavelength at the midplane of the CCD chip can then be written solely as a function of inclusion angle and the rotation angle of the grating ψ:

$$\lambda = \frac{2}{kn} \sin\psi \cos\left(\frac{\gamma}{2}\right). \tag{5.3}$$

To find the wavelength at a location other than the CCD midplane, the focal length f, and the detector angle δ, must be taken into account. Both are determined through a calibration process that involves looking at spectral lines from a known source, such as a mercury lamp, at different locations on the CCD. The focal length is calculated to be within a few mm of the nominal value of 500 mm, while the detector angle has been aligned to within one degree of perpendicular. The equation for the wavelength at any point x on the CCD is then

$$\lambda(x) = \frac{1}{kn}\left\{\sin\left(\psi - \frac{\gamma}{2}\right) + \sin\left(\psi + \frac{\gamma}{2} + \xi(x)\right)\right\} \tag{5.4}$$

where the angle ξ is related to f and δ by the formula

$$\tan\xi = \frac{x\cos\delta}{f + x\sin\delta}. \tag{5.5}$$

The next step in calibrating the raw image is to correct for the instrument curvature induced by errors in the aspheric mirrors. Line radiation from a stationary calibration source should appear as a perfectly vertical line on the CCD. In reality, the line radiation is bent in varying amounts along the vertical imaging axis, forming a curved image. Since this error is of the same order as the Doppler shift being measured, it must be corrected for. The curvature correction factor is generated as follows. An image of a known calibration line is obtained from a calibration lamp. The peak wavelength of each row is found from a Gaussian fit. A second-order polynomial is then fit through the peaks. If there were no curvature effects in the optics, then this fit would be a perfectly straight vertical line. The curvature varies with

wavelength so the process is repeated for different calibration lines. A typical curvature fit is shown in Fig. 5.6.

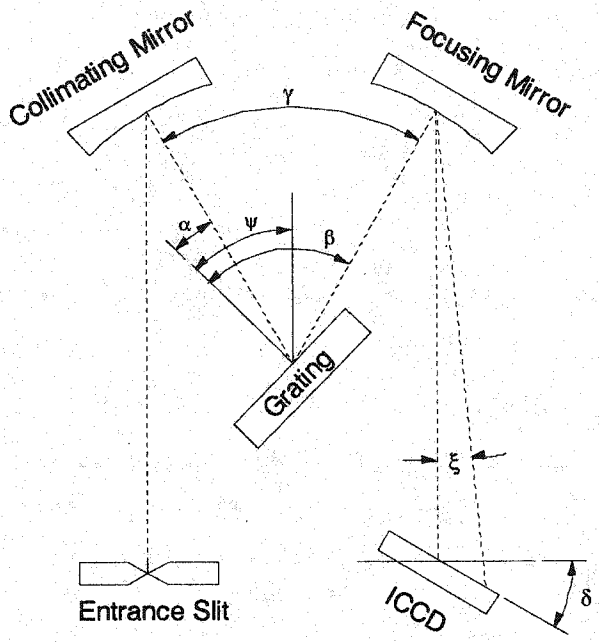

Figure 5.5: *Grating Geometry*

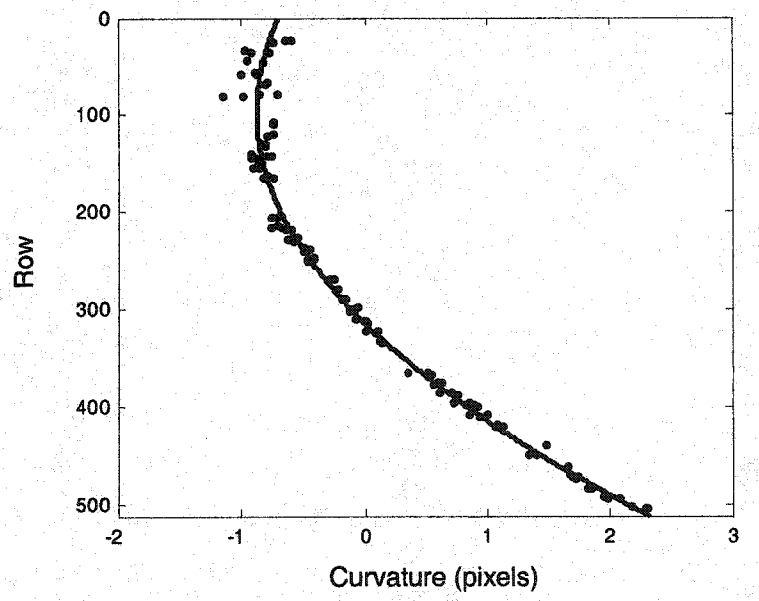

Figure 5.6*: ICCD Instrument Curvature. Fit shown is for the Hg I line at 404.656 nm viewed with an 1800-g/mm 250-nm blaze grating.*

Once the curvature has been removed from the image, the data for each fiber bundle can be averaged in a process called binning. The row numbers for each fiber bundle image are identified as a region of interest, or ROI. Once the rows for each ROI are determined, the columns are "binned" or summed and averaged, producing a single spectrum for each ROI. There are typically six fiber bundles and thus six ROIs, so the binning process reduces a 512 x 512 image into six individual spectra, each with 512 points on the wavelength axis.

If the curvature correction is applied back to the calibration images, a nearly perfectly vertical image should be produced. A comparison of binned spectra produced with and without the curvature correction is shown in Figure 5.7. In the data produced without curvature removal, the spectra are clearly shifted. The lower set of data, with the curvature calibration applied, are not only centered but also are narrower, because the curvature within each ROI has been removed before binning.

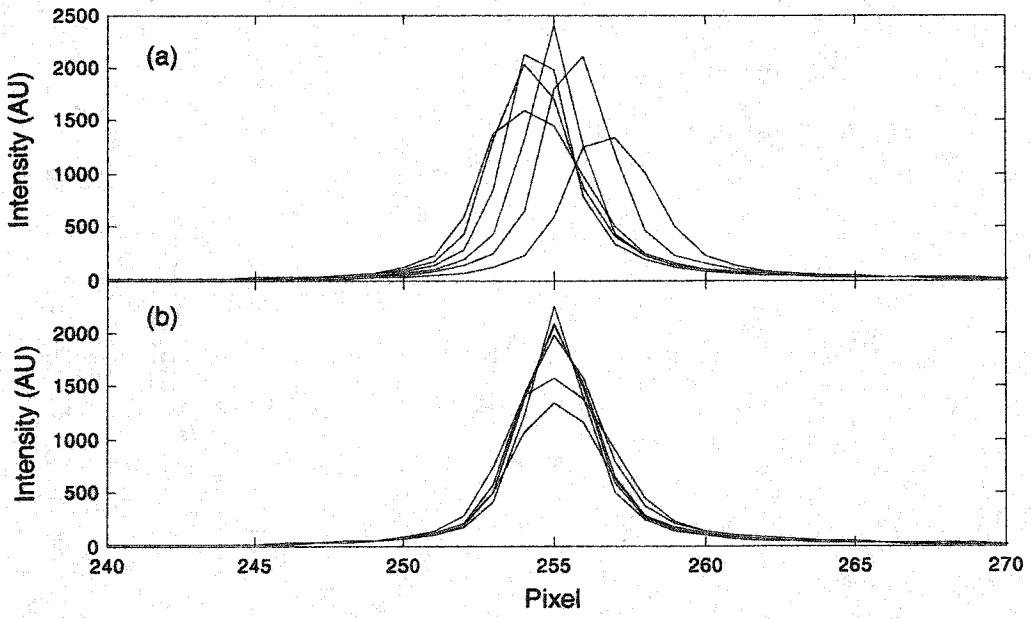

Figure 5.7: *Binned Calibration Spectra. (a) Hg I line at 404.656 nm binned without the curvature correction. (b) Same line but with the curvature removed before binning.*

5.3 Deconvolution

Even with the instrument curvature removed, line radiation is still broadened due to finite slit width and optical imperfections in the grating and mirrors. The output spectrum for a perfectly narrow delta function input is called the instrument function or point spread function (PSF). An input spectrum F is convolved with the instrument function G, resulting in the observed output spectrum H:

$$H(\lambda) = F(\lambda) * G(\lambda). \tag{5.6}$$

The process of inferring the input spectrum F from the known instrument function G and the observed spectrum H is deconvolution. Several deconvolution techniques were attempted, and will be described briefly.

The simplest method attempted was analytic deconvolution. Assume that the instrument function G can be modeled by a simple analytic function such as a Gaussian, Lorentzian, or Voigt function. A Gaussian function is of the form

$$G(\lambda) = A_1 \exp\left(-z^2/2\right); \qquad z \equiv \frac{\lambda - A_2}{A_3}, \tag{5.7}$$

where A_1 is the peak intensity, A_2 is the central wavelength, and A_3 is the standard deviation. A Lorentzian function is of the form

$$G(\lambda) = \frac{A_1}{\pi} \frac{A_3}{(\lambda - A_2)^2 + A_3^2}, \tag{5.8}$$

where A_1 is the area under the spectrum, A_2 is the central wavelength, and A_3 is the half-width at half-maximum (HWHM). A Voigt function is a combination of the two. Similarly, if the input spectrum F is also assumed to be one of these analytic functions, then the deconvolution can be performed analytically[36]. Unfortunately, the instrument function is not well-modeled by any of these analytic functions, as shown in Fig. 5.8.

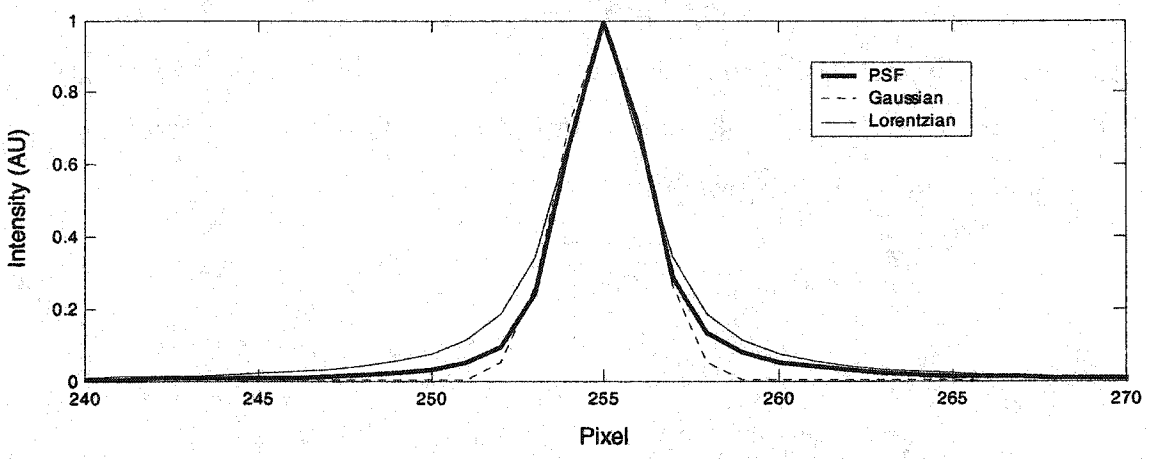

Figure 5.8: *ICCD Instrument Function. Instrument function for Hg I line at 405 nm compared with Gaussian and Lorentzian functions having the same FWHM.*

The second method attempted was Fourier deconvolution. Taking the Fourier transform $\mathcal{F}$ of Eq. (5.6) yields

$$\mathcal{F}(\mathrm{H}) = \mathcal{F}(\mathrm{F})\mathcal{F}(\mathrm{G}). \tag{5.9}$$

The input spectrum is then found by rearranging and taking the inverse transform $\mathcal{F}^{-1}$

$$\mathrm{F} = \mathcal{F}^{-1}\left[\frac{\mathcal{F}(\mathrm{H})}{\mathcal{F}(\mathrm{G})}\right]. \tag{5.10}$$

This method is sensitive to noise in the spectrum. Even using a Weiner filter[37] to minimize the effect of high-frequency noise, a satisfactory result could not be obtained with this method. A possible reason is the poor signal-to-noise ratio in the wings of the spectrum, particularly as the exposure time is shortened and single-photon statistics become important.

The final method attempted and finally adopted was to restrict the input spectrum to be a pure Gaussian, given by Eq. (5.7). Different input Gaussians are convolved with the known instrument function and compared with the observed output spectrum. The process is repeated until the coefficients A_1, A_2, and A_3 are found that result in the minimum least-squares error between the calculated output spectrum and

the observed spectrum. The error between the actual data and the convolved Gaussian is computed using a weighting function w as shown in Fig. 5.9 with a half-width of 4σ. This weighting function lowers the relative importance of the error in the wings of the spectrum, where the signal-to-noise ratio is low.

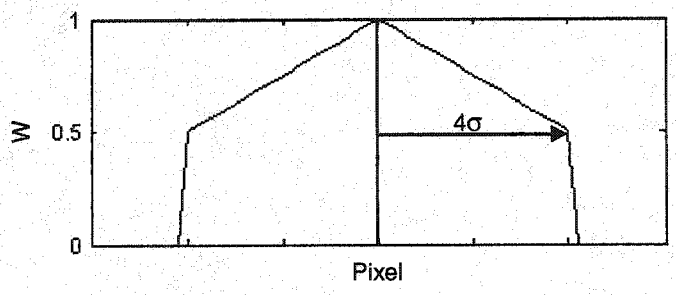

Figure 5.9: *Weighting Function for Least-squares Fit*

5.4 Abel Inversion

The ICCD system makes chord-integrated measurements of the emission spectrum. The line-of-sight spectra must be spatially inverted in order to obtain the local emission and velocity profiles. The system has only six viewing chords, too few to make a good analytic or spline fit. Instead, the data is spatially inverted using a shell model.

Following the notation of Bell[38], assume that plasma is axisymmetric and is divided into j radial zones, as shown in Fig. 5.10. Each zone is assumed to have a uniform emission ε_j and rotational frequency ω_j. The path length L_{ij} for sightline i with impact parameter y_i through shell j is given by:

$$\begin{aligned} &\text{for i < j:}\quad Lij = 2\sqrt{y_{j+1}^2 - y_i^2} - 2\sqrt{y_j^2 - y_i^2} \\ &\text{for i = j:}\quad Lij = 2\sqrt{y_{j+1}^2 - y_i^2} \\ &\text{for i > j:}\quad Lij = 0 \end{aligned} \tag{5.11}$$

θ_{ij} is defined as the angle between chord i and the tangent of shell j. The apparent Doppler shift $(v_j/c)\cos\theta_{ij}$ is then constant along sightline i through shell j as long as ω_j is uniform. The measured brightness B_i is related to the emission profile ε_j by

$$B_i = \sum_j L_{ij} \varepsilon_j \,. \tag{5.12}$$

Eq. (5.12) can be inverted to obtain the emission ε_j from the measured B_i:

$$\varepsilon_j = \sum_i L_{ji}^{-1} B_i \,. \tag{5.13}$$

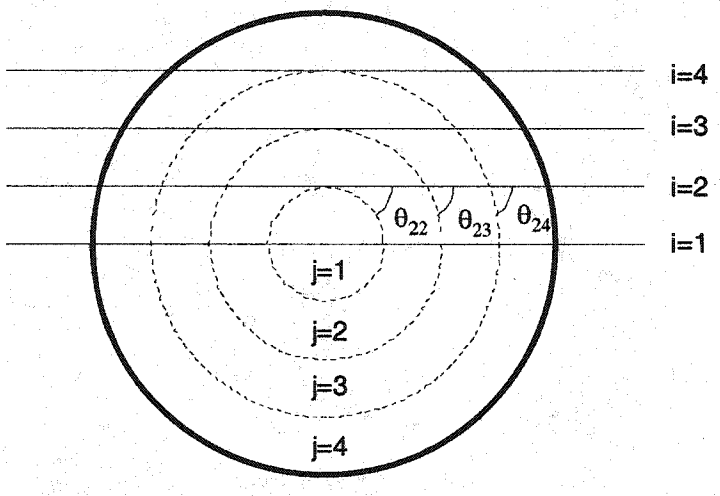

***Figure 5.10**: Abel Inversion Geometry. Only four chords and shells are shown for clarity. The actual experiment has six chords and six shells.*

The brightness B_i is found by integrating the observed spectrum and does not require deconvolution. Before inverting, the brightness is corrected by the relative transmission of each fiber. The transmission through the quartz tube at varying impact parameters must also be considered. Approximating the quartz wall as a flat plane, then the transmission angle θ_t through the quartz can be related to the incidence angle θ_i by Snell's law $n_1 \sin\theta_1 = n_2 \sin\theta_2$, where n_1 is the index of refraction of vacuum (and air) and n_2 is the index of refraction for quartz, as shown in Fig. 5.11. The transmission for light polarized in the parallel and perpendicular planes relative to the quartz is

$$T_{\parallel} = 1 - \left[\frac{n_1 \cos\theta_t - n_2 \cos\theta_i}{n_1 \cos\theta_t + n_2 \cos\theta_i} \right]^2$$
$$T_{\perp} = 1 - \left[\frac{n_1 \cos\theta_i - n_2 \cos\theta_t}{n_1 \cos\theta_i + n_2 \cos\theta_t} \right]^2 \qquad (5.14)$$

The transmitted intensity, shown in Fig. 5.12, is then given by

$$I_{out} = \frac{1}{2}\left(T_{\parallel}^2 + T_{\perp}^2\right) I_{in} . \qquad (5.15)$$

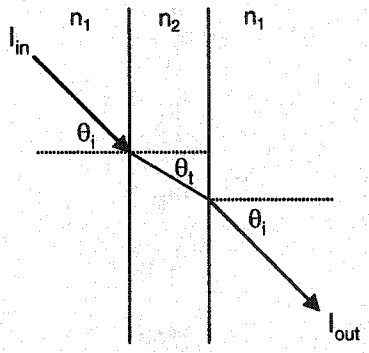

***Figure 5.11**: Quartz Transmission Geometry.*

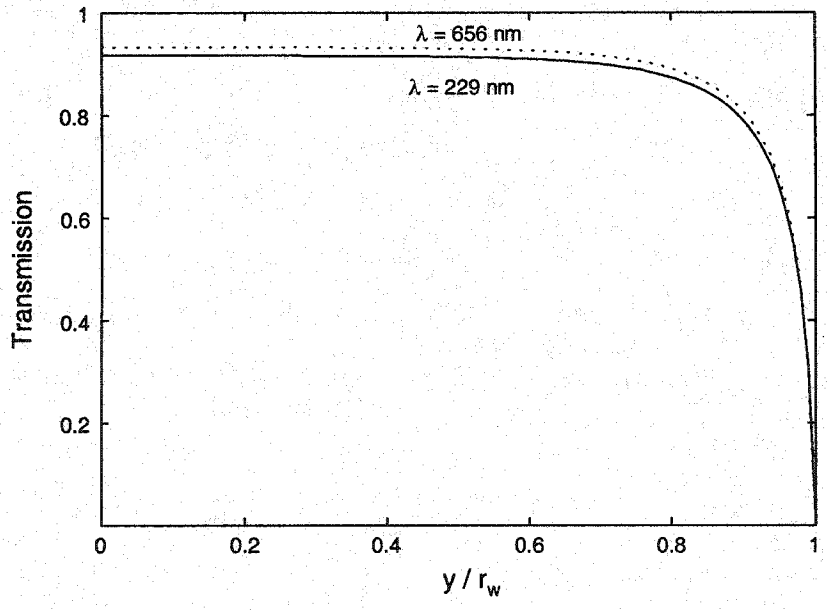

***Figure 5.12**: Quartz Transmission. Intensity transmission is plotted versus impact parameter y normalized by the wall radius r_w.*

The ion temperature in TCS is often low enough that there is no significant Doppler broadening of the impurity line radiation. In this case, deconvolution is not necessary and the velocity profile can be obtained via a matrix inversion as well. The apparent velocity u_i, found from the Doppler shift of the centroid wavelength of the observed spectrum, is then

$$B_i u_i = \sum_j M_{ij} \varepsilon_j v_j \tag{5.16}$$

where $M_{ij} \equiv L_{ij} \cos\theta_{ij}$. This can be inverted to obtain the local velocity v_j

$$v_j = \frac{\sum_i M_{ji}^{-1} B_i u_i}{\varepsilon_j}. \tag{5.17}$$

The velocity inversion thus depends on the emission inversion; any errors in the emission inversion will propagate into the velocity inversion.

When the observed line radiation is broader than the instrument function, either from Doppler broadening or turbulent broadening, then the simple matrix inversion scheme presented above is inconsistent with the deconvolution method presented in Sec. 5.3. The deconvolution method assumes that the input spectrum for each chord is a pure Gaussian distribution. If the shells viewed by a chord are rotating at varying frequencies, then the actual input spectrum will be a sum of Gaussians, each with a different Doppler shift. The inversion scheme is modified slightly to take this into account, as follows. Instead of solving for all shells simultaneously, the shell properties are solved for individually starting with the outermost shell. The spectrum from shell j = n, where n is the total number of chords and shells, is assumed to be a pure Gaussian and can be deconvolved as in Sec. 5.3. The emission has already been obtained through Abel inversion and puts a constraint on the deconvolution:

$$\sqrt{2\pi} A_1 A_3 = \varepsilon_j \tag{5.18}$$

The contribution of the spectrum observed by chord n-1 from shell n can then be estimated by convolving the Gaussian distribution for shell n with the instrument function for chord n-1:

$$H(\lambda) = F_{i=n-1}(\lambda) * G_{j=n}(\lambda) . \tag{5.19}$$

The calculated spectrum is subtracted from the observed spectrum for chord n-1. The remaining spectrum must have come from shell n-1 and can be deconvolved to solve for ε_{n-1} and ω_{n-1}. This method is then repeated for each successive shell.

Chapter Six

Ion Rotation Measurements

The experimentally measured azimuthal velocity of various plasma species is presented in this chapter. The bound-bound transition lines used for Doppler shift measurements are summarized in Table 6.1. Lines from neutrals as well as impurities of varying mass and ionization state were studied. In Sec. 6.1, the Doppler shift of these lines is presented without spatial inversion. Chord-integrated velocity measurements may not provide the true rotation profile but are useful for comparing the edge rotation velocity of different species. The ion temperature is estimated in Sec. 6.2. In Sec. 6.3, the spectra are spatially inverted to obtain local emission, velocity, and ion temperature profiles. In Sec. 6.4, a rigid rotation frequency is fit to the chord-integrated velocity profile. The rotation frequency is then plotted against different plasma parameters such as RMF frequency, field strength, and antenna length. The effect of RMF antenna length is examined in Sec. 6.5. Finally, in Sec. 6.6, the plasma rotation is compared with the n = 2 rotational mode frequency.

***Table 6.1**: Spectral Lines Used for Doppler Effect Measurements*

Species	Wavelength (nm)	Atomic Mass (AMU)	Ionization Energy (eV)
Dα	656.103	2	13.6
Dβ	486.003	2	13.6
He I	388.865	4	24.6
He II	468.570	4	54.4
C III	229.687	12	47.9
O III	326.533	16	54.9
Si III	455.262	28	33.5

6.1 Chord-integrated Velocity

The chord-integrated velocity for various neutral and ion species is presented here. These results are obtained without a spatial inversion. Therefore, these results may not represent the actual velocity profile. Only through a spatial inversion can slight differences in rotation frequency at dimmer, inner radii be detected. Nevertheless, these chord-integrated results are a useful way of comparing the edge rotation velocity of various species without the complications of spatial inversion.

Chord-integrated velocity profiles for the C-III impurity line at 229.687 nm, viewed in third order, are shown in Fig. 6.1 for two repeatable shots. The collection optics have been positioned in both a symmetric fan and an asymmetric fan, as shown in Fig. 5.3, for comparison. The results are similar, proving that the inferred rotation is not due to a systematic error in the curvature calibration. Another proof of the validity of the calibration is shown in Fig. 6.2, a comparison of the ion rotation of C-III 229-nm radiation viewed at both first order and at third order (689.061 nm). These orders are viewed by different gratings with independent calibrations, yet the results are the same.

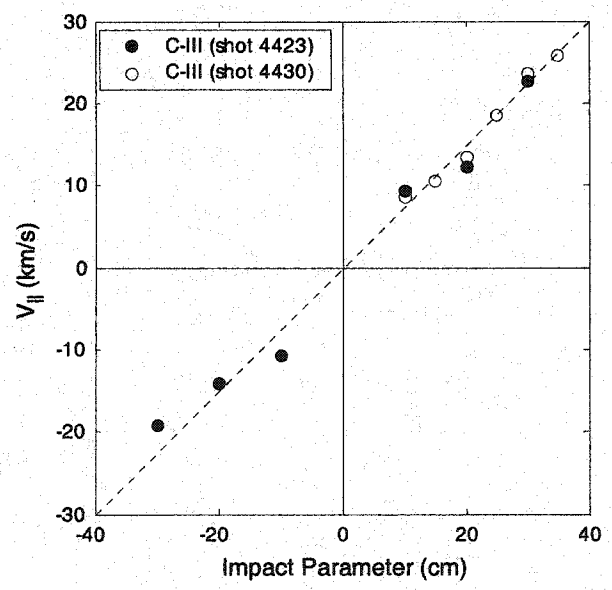

***Figure 6.1**: Chord-integrated Carbon Azimuthal Velocity. C-III line at 229.687 viewed at third order (689.061 nm) at t=600 μs with RMF frequency $\omega=0.5\times10^6\ s^{-1}$.*

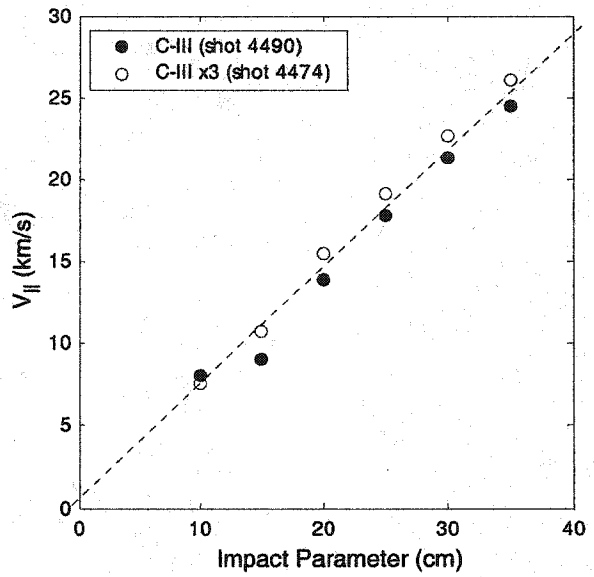

***Figure 6.2**: C-III Velocity Viewed at Different Orders. C-III 229.687 nm line viewed at first order and third order at t=1000 μs. RMF frequency $\omega=0.5\times10^6\ s^{-1}$.*

Carbon is a minority species in the deuterium plasma, with a typical impurity fraction of a few percent[39]. A key question is how well the carbon impurity corresponds with the motion of the bulk plasma. The plasma majority species is fully-ionized deuterium, which does not emit bound-bound line radiation and cannot be used for Doppler effect studies. There is promising evidence that carbon is a good tracer for the deuterium plasma motion. In Fig. 6.3, C-III azimuthal velocity is compared with both heavier and lighter ion species to see if ion mass has any effect on rotation. Si-III is typically present in TCS due to ablation of the quartz vacuum wall, and has an ionization energy similar to carbon. Silicon has an atomic mass of 28, more than double that of carbon at 12. A comparison of the rotation profiles in Fig. 6.3 indicates that carbon and silicon rotate synchronously. Further evidence that all plasma species rotate at the same speed comes from operation in pure helium. Helium has an atomic weight of 4 and has two electrons so it may not fully ionize. He-II has an ionization potential of 54.4 eV, higher than the C-III ionization energy. Comparison of the rotation profiles of C-III and He-II also show synchronous rotation.

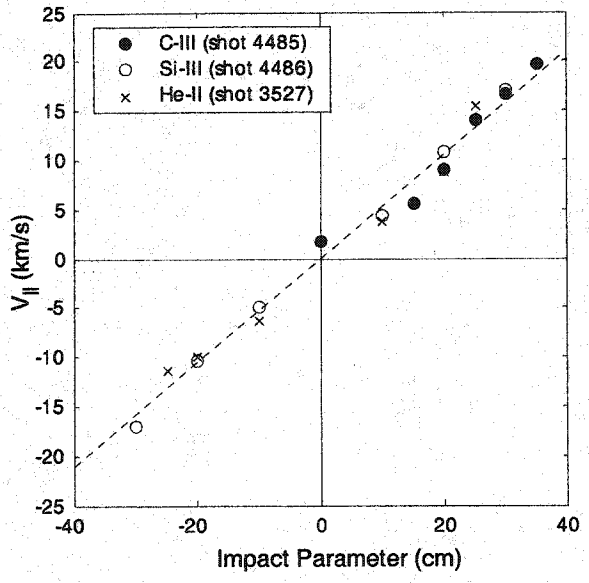

***Figure 6.3**: Chord-integrated Rotation of Various Ion Species. Doppler shift of C-III x3 (689.061 nm), Si-III (455.262 nm), and He-II (468.570 nm) lines for $\omega=0.5\times10^6\ s^{-1}$.*

No Doppler shift is observed for the chord-integrated line radiation of neutral species, shown in Fig. 6.4. Dα and Dβ lines from neutral deuterium atoms and neutral He-I radiation from pure helium operation show no significant azimuthal rotation.

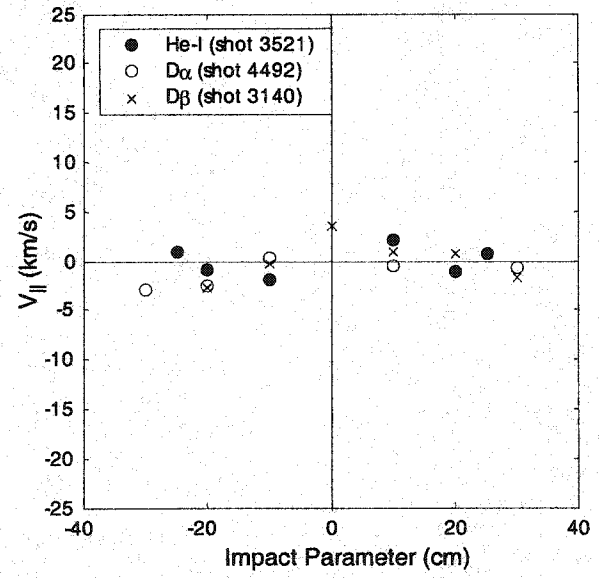

***Figure 6.4**: Chord-integrated Rotation of Various Neutral Species. Data obtained from He-I (388.865 nm), Dα (656.103 nm), and Dβ (486.003 nm) lines for $\omega=0.5\times10^6\ s^{-1}$.*

6.2 Ion Temperature

Determination of the plasma total temperature is relatively easy in FRCs because they are high β and the total temperature can be calculated from pressure balance, as described in Sec. 7.1. The ratio of the electron temperature T_e to the ion temperature T_i will be very important for the power balance and torque balance models to follow. However, with the limited diagnostics on TCS it is difficult to determine T_e and T_i. Presently, TCS does not have a Thomson scattering system to determine electron temperature. A double Langmuir probe has been developed for TCS, but the voltage cannot be swept during a shot because of RMF pickup. Instead, the DC bias across the probe tips can be varied from shot to shot, and an estimate of the electron temperature can be made from the variation of the ion saturation current. Results for a series of repeatable shots are shown in Fig. 6.5. The electron temperature seems to be roughly half of the total plasma temperature.

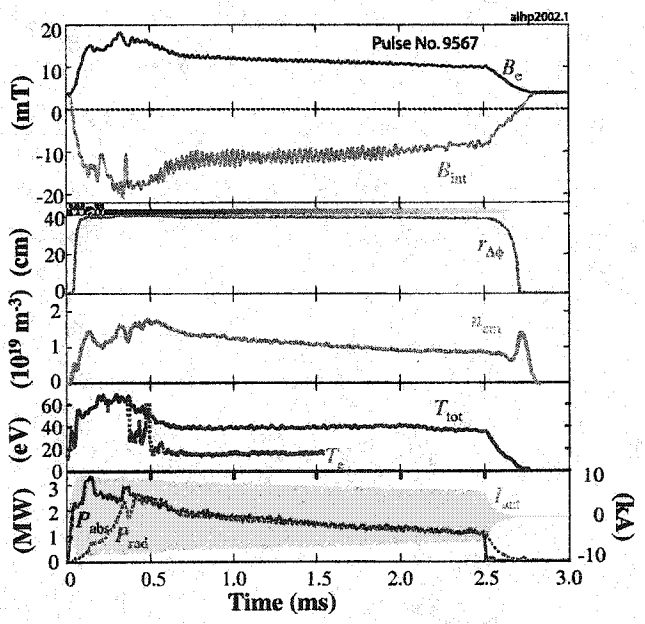

***Figure 6.5**: Electron Temperature from Double Langmuir Probe. Langmuir probe data (blue line) is from a series of repeatable shots. RMF frequency $\omega = 0.72\times10^6\ s^{-1}$.*

The neutral temperature can be obtained from the Doppler broadening of the Balmer α line (656.103 nm) of neutral deuterium. The Dα line is preferable to Dβ

(486.003 nm) because Dβ is also Stark broadened. Interpretation of the Dα spectrum is difficult because TCS contains a significant fraction of hydrogen. The Hα line is at a slightly different wavelength (656.285 nm) and the two lines overlap. The neutral temperature has been obtained using a Gaussian deconvolution as described in Sec 5.3 with the following modifications. Instead of a single Gaussian, a double Gaussian (one for Dα, one for Hα) is convolved with the instrument function and compared with the observed spectra. The separation between the two Gaussians is fixed at 0.179 nm, implying no relative drift between the two isotopes. The temperature of the two isotopes is also assumed equal at each radius. The H:D fraction and the neutral temperature are allowed to vary with radius. At this point, the data is not spatially inverted. A typical observed spectrum and the convolved fit are shown in Fig. 6.6. Early in the discharge shown in Fig. 6.7, the total plasma temperature is found from pressure balance to be about 50 eV. The neutral temperature profile, shown in Fig. 6.8, varies from ~25 eV at the center of the plasma to ~7 eV at the edge. The H:D fraction also varies, from a low of 17% at the center of the plasma to nearly 30% at the edge, presumably due to outgassing of the walls. Later in the discharge (t=1300 μs), the plasma has developed a n=2 instability and the hydrogen fraction is much more uniform (~18%). The total plasma temperature has decreased to ~27 eV, and the neutral temperature, shown in Fig. 6.9, has decreased to a more uniform value of ~8 eV.

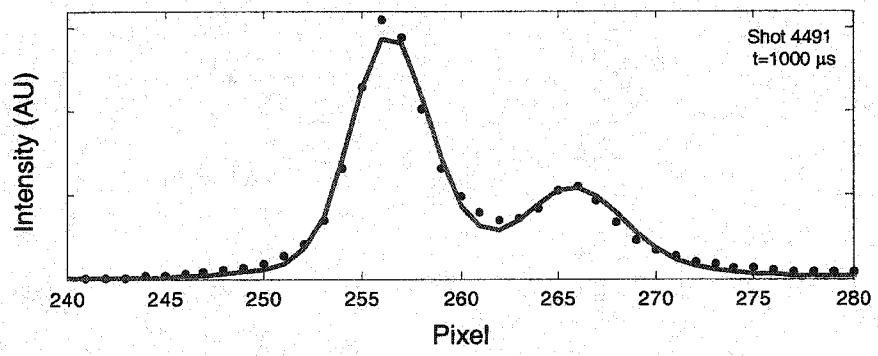

***Figure 6.6**: Dα Spectrum and Convolved Fit. Black dots: observed spectrum. Red line: convolved double Gaussian fit.*

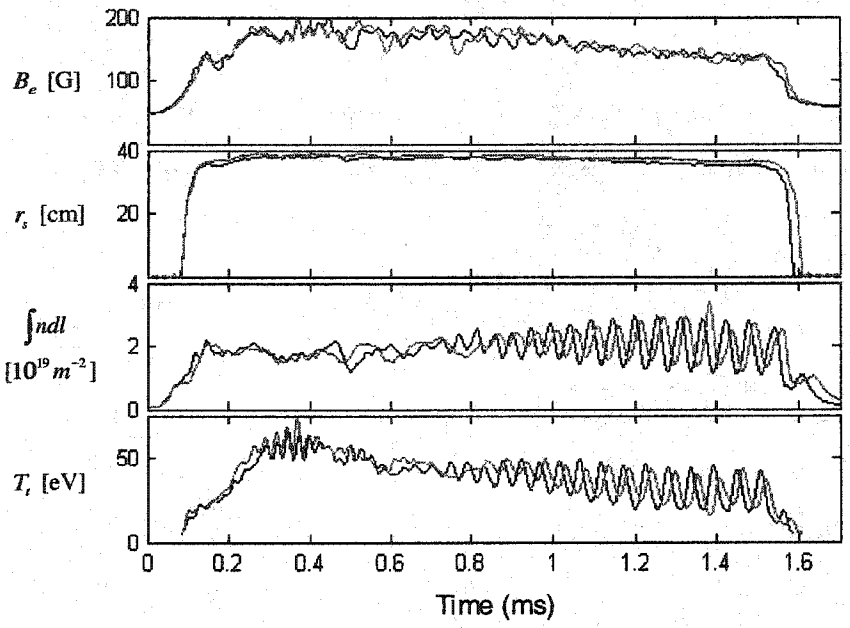

***Figure 6.7**: Plasma Parameters for Dα Deconvolution. Black line: 8636. Red: 8637.*

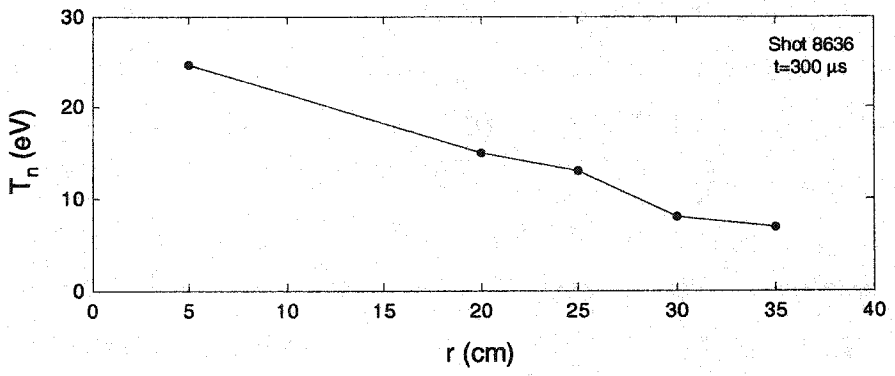

***Figure 6.8**: Neutral Temperature Profile at t=300 μs.*

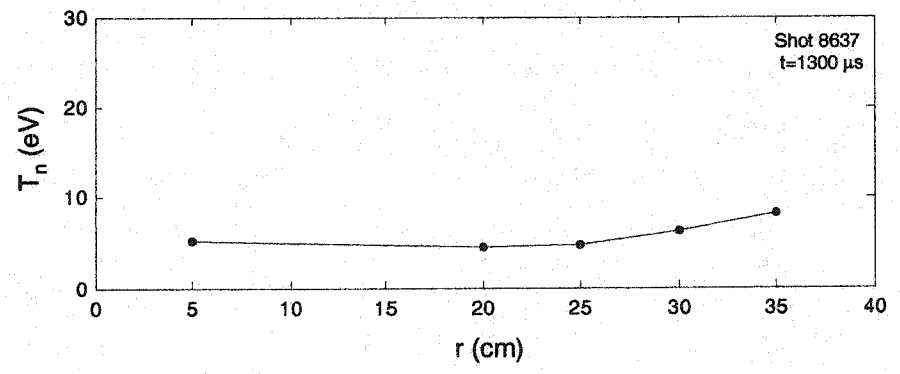

***Figure 6.9**: Neutral Temperature Profile at t=1300 μs.*

The ion temperature should be obtainable from the Doppler broadening of impurity line radiation. Surprisingly, nearly all the C-III and Si-III spectra collected are as narrow as, or even narrower than, the instrument function for calibration lines at similar wavelengths. These impurities should be in rapid thermal equilibrium with the deuterium plasma, as given by the classical ion-ion thermal equilibrium time:

$$\tau_{\alpha\beta} = 5.5\times10^{18}\frac{\left(m_\alpha T_\beta + m_\beta T_\alpha\right)^{3/2}}{\sqrt{m_\alpha m_\beta} Z_\alpha^2 Z_\beta^2 n_\beta \ln\Lambda_{\alpha\beta}} \quad [\mathrm{s}] \tag{6.1}$$

where all quantities are in cgs units except temperature, which is in eV. Computing the $C^{+2} - D^{+1}$ equilibration time with T_D=15 eV, T_C=1 eV, n_D=1×10^{13} cm^{-3}, and n_C=2% n_D yields a short equilibration time of 1 μs. If the bulk plasma ions have any significant temperature, then the carbon impurity should be in thermal equilibrium. Although Doppler broadening is diminished for heavier impurities by $\sqrt{m}$ and the "instrument temperature," or instrument-induced broadening, for the C-III line is about 20 eV, additional broadening for ~15 eV carbon should be discernable. Several possible explanations for the lack of Doppler broadening in the carbon spectra are proposed. One, the ion temperature could truly be cold, although this is not indicated by the Langmuir probe or the neutral temperature measurements. Two, bremmstrahlung continuum radiation often dominates the emission in the wings of the line spectrum. When this background radiation is subtracted, the resulting line spectrum appears narrower. Third, the instrument functions obtained from Hg and Cd lamps may also be slightly pressure broadened or temperature broadened and may not represent true delta function inputs. Four, the number of photons collected in the wings of the spectrum is small for these low density, low temperature plasmas, especially when the exposure time is short (less than 50 μs). Finally, errors in calibration, curvature removal, and deconvolution may simply overwhelm the slight ~10 eV temperature broadening.

6.3 Rotation Profile

In the previous section, chord-integrated Doppler shift results for various plasma species were presented. Although the ion rotation profile appears to be that of a

rigid rotor based on these results, a spatial inversion must be performed to prove this. As described in Sec. 5.4, a "peel" method of Abel inversion has been developed that deconvolves the asymmetric instrument profile from the measured spectra by assuming that each shell radiates with a Gaussian distribution. For this method to be successful, however, the measured spectra must be broader than the instrument function; otherwise the deconvolution will fail. Furthermore, if the velocity profile is anything but rigid rotor it must lead to apparent broadening of the chord-integrated spectra.

As described in Sec. 6.2, spectra for C-III and Si-III do not typically show any significant broadening. A handful of shots have been obtained where the observed spectra for all chords are broader than the instrument function. Fig. 6.10 shows plasma parameters for two such shots. These plasmas exhibit a mild n=2 distortion even though the separatrix is near the wall. These plasmas therefore do not strictly satisfy the inherent assumption of axisymmetry required for an Abel inversion. Nevertheless, an inversion and deconvolution is attempted. The error associated with the non-axisymmetry will be calculated in Appendix A.

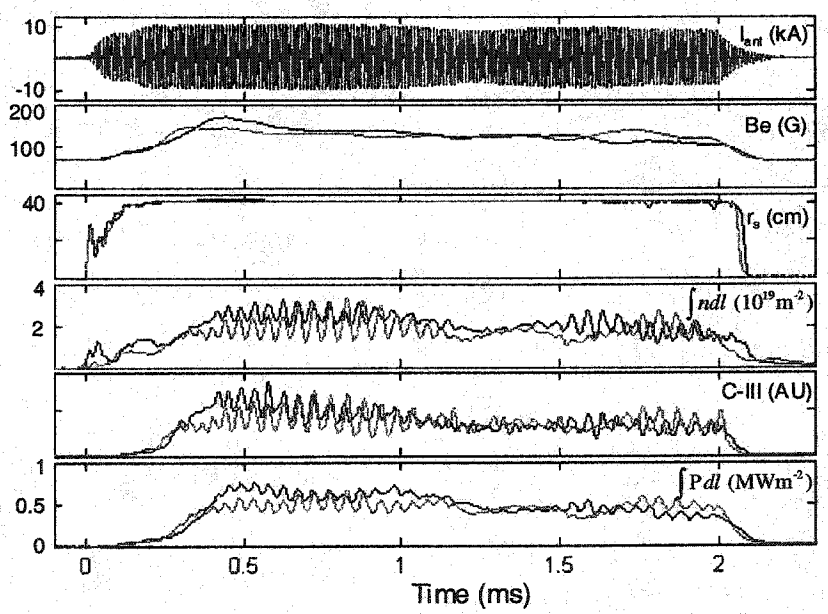

Figure 6.10: *Plasma Parameters for Shots 4430 and 4438. Red line: shot 4430. Black line: shot 4438.*

The chord-integrated spectra have been spatially inverted and deconvolved using both the peel method and the simple matrix inversion technique described in Sec. 5.4. In Figs. 6.11 and 6.12, inverted profiles for the C-III line at 229.687 nm viewed in third order are shown. Both results are taken at t = 600 μs with a 25 μs exposure. The RMF frequency $\omega = 0.52\times10^6$ s^{-1}, the bias field B_0 = 66 G, and the total temperature T_t = 32 eV are the same for both cases. In Fig. 6.11, the vacuum RMF field strength B_ω = 50 G and the average electron density $\langle n_e \rangle = 1.3\times10^{19}$ m^{-3}. In Fig. 6.12, the RMF field is higher at B_ω = 65 G, resulting in a higher density $\langle n_e \rangle = 1.7\times10^{19}$ m^{-3}. Despite these differences, the results are similar. The top graph in each figure shows the chord-integrated brightness data as black points, and the Abel-inverted emission profile as a blue line. In Fig. 6.11 the emission is peaked at the null, while the higher-density shot shown in Fig. 6.12 has a much broader emission profile. In the middle graph, the chord-integrated velocity profile is shown as black points, the matrix-inverted velocity profile is shown in blue, and the deconvolved velocity profile is shown in red. The deconvolved results indicate that the plasma may not be truly rigid, but rather that the plasma near the geometric axis rotates more slowly. Finally, the bottom graph shows the deconvolved temperature profile in red, along with the instrument temperature for each chord as a black point. The plasma total temperature is shown as a dashed line. The carbon ion temperature is roughly equal to half the total temperature, although the temperature resolution below the instrument temperature is poor. The inverted spectra from each shell are shown in Fig. 6.13 in black, along with the convolved Gaussian fit for each shell in red. From the close agreement, it can be claimed that although the inversion and deconvolution may not be a unique solution, it is certainly a valid solution.

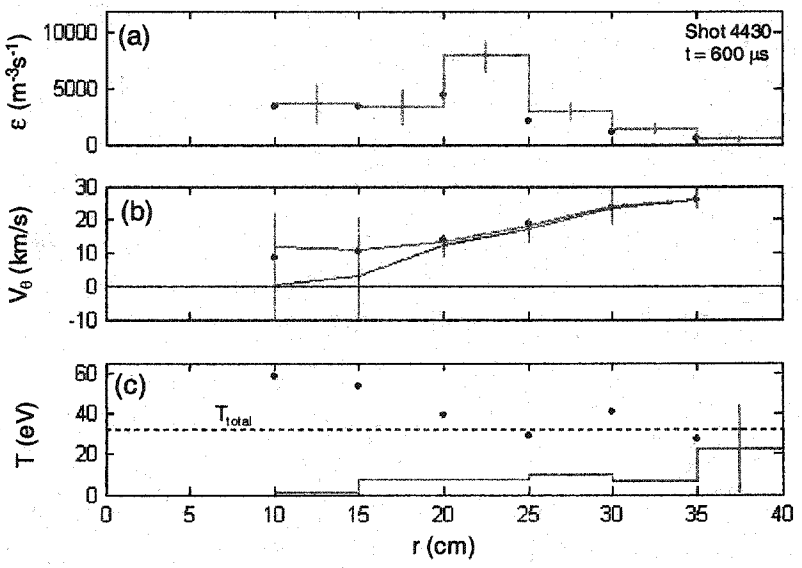

Figure 6.11: *Inverted C-III Profiles for Shot 4430. Data from C-III 229 nm line at third order. (a) black dots: chord-integrated brightness. Blue line: matrix inverted emission. (b) black dots: chord-integrated velocity. Blue line: matrix inverted velocity. Red line: deconvolved velocity. (c) black dots: Instrument temperature. Red line: deconvolved temperature.*

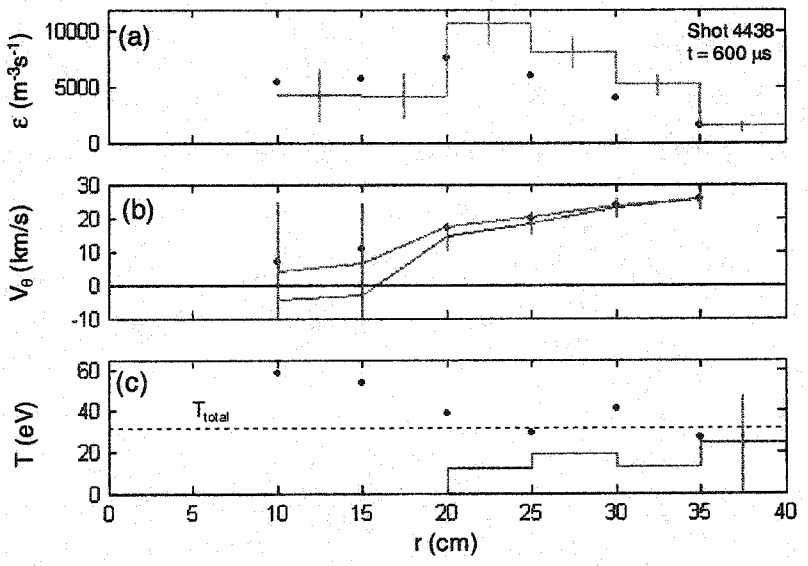

Figure 6.12: *Inverted C-III Profiles for Shot 4438.*

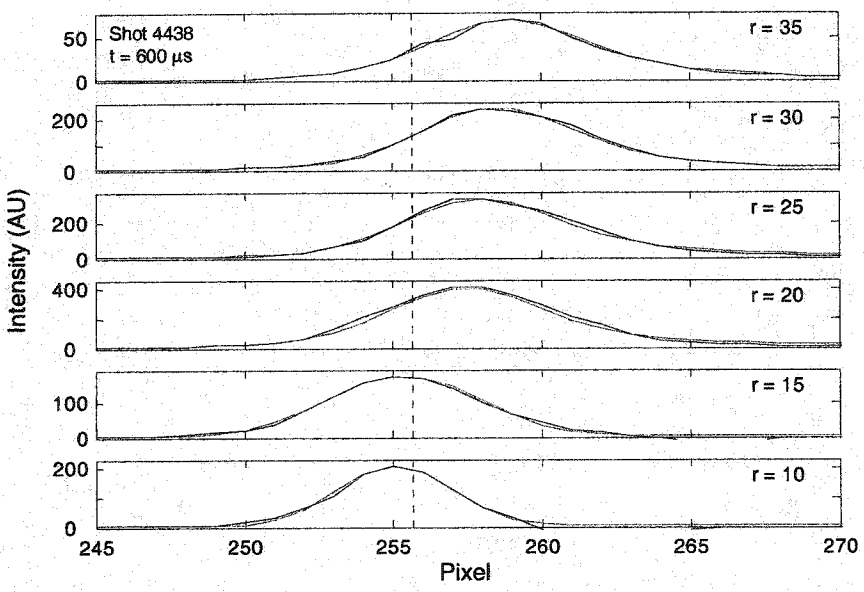

***Figure 6.13**: Inverted Spectra and Convolved Fit for Shot 4438. Black line: inverted spectra. Red line: Convolved gaussian fit. Dashed line: rest wavelength λ_0.*

Inverted profiles obtained from the Si-III line at 455.3 nm for similar plasma conditions are shown in Fig. 6.14. The emission profile is very similar to that of C-III and roughly follows the plasma density profile. The velocity profile, however, is quite different in that ions at the edge (35 cm) are rotating more slowly than plasma further in. This could be due to the fact that Silicon is introduced at the plasma edge due to wall ablation, and because of its large mass takes longer than carbon to spin up.

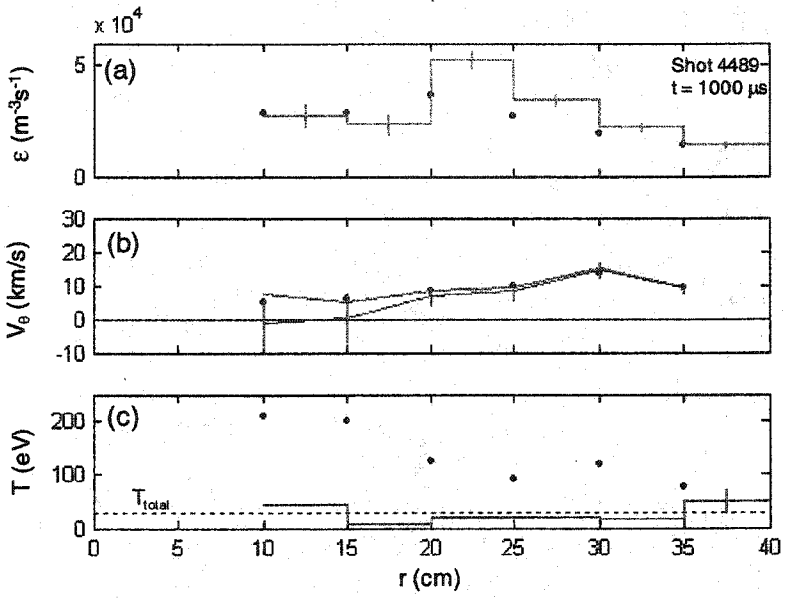

Figure 6.14: Inverted Si-III Profiles for Shot 4489.

6.4 Rotation Frequency

In Sec. 6.3, the ion azimuthal velocity profile was seen to be very close to rigid rotor. Ions near the geometric axis may be rotating more slowly, but the error bars in the spatial inversion are too large to make a definitive claim of this. In order to compare the ion rotation for different plasma conditions, the ion velocity profile is assumed to be rigid rotor and the chord-integrated velocity is fit to a rotation frequency ω_i:

$$v_{i\theta}(r) = \omega_i r . \tag{6.2}$$

The time evolution of the carbon ion rotation frequency is shown in Fig. 6.15 for a series of repeatable shots with RMF frequency $\omega = 0.52\times10^6$ s^{-1}. The ICCD camera can only take a single exposure during a shot, so each data point was obtained from a different shot, triggered at a different time. C-III does not begin radiating until t = 300 μs, by which time it has already spun up to the steady-state value of $\omega_i \approx 6.5\times10^4$ s^{-1}, or 12.5% of the RMF frequency.

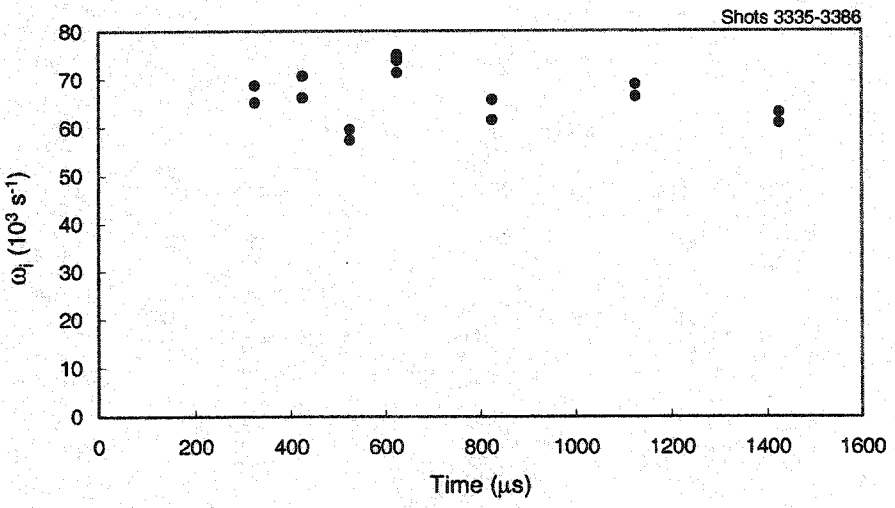

***Figure 6.15**: C-III Rotation Frequency for $\omega = 0.52\times10^6$ s^{-1}. All data taken with 50-μs exposure.*

The time evolution of the carbon ion rotation frequency is shown in Fig. 6.16 for a series of repeatable shots with higher RMF frequency $\omega = 0.72\times10^6$ s^{-1}. Carbon again reaches a steady-state rotation frequency of $\omega_i \approx 6.0\times10^4$ s^{-1}, or 8.5% of the RMF frequency. At this drive frequency, however, the spin-up behavior is slightly different. Early in the discharge the impurity ions are rotating even faster, up to nearly $\omega_i \approx 9.0\times10^4$ s^{-1} at t = 200 μs. Either a higher RMF torque is applied early in the discharge or else the drag torque is lower. The reasons for the slowdown of the ion azimuthal velocity will be examined more carefully in Sec. 8.3 where a torque balance will be carried out.

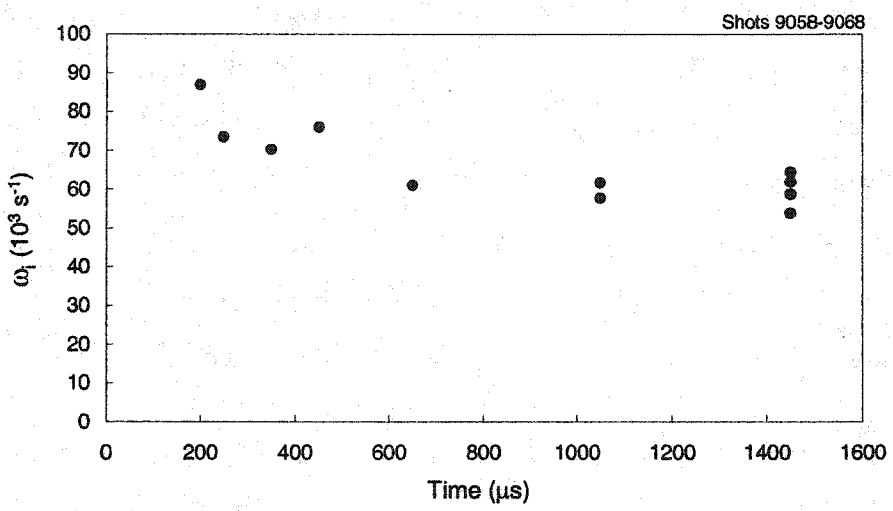

***Figure 6.16**: C-III Rotation Frequency for $\omega = 0.72\times10^6$ s^{-1}. All data taken with 100-μs exposure.*

The plasma spin-up is different at the highest RMF frequency $\omega = 1.62\times10^6$ s^{-1}. The ion rotation is much slower at $\omega_i \approx 2.5\times10^4$ s^{-1}, or only 1.5% of the RMF frequency. The antenna impedance ωL is higher at this RMF frequency, and the applied field B_ω is lower, under 30 G. Thus, the applied torque and the plasma density are much lower. The torque balance will be examined more carefully in Sec. 8.3.

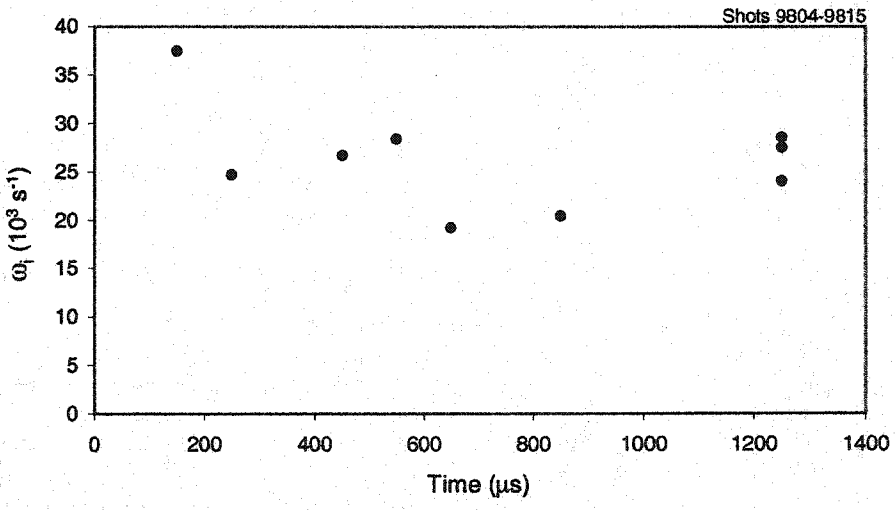

***Figure 6.17**: C-III Rotation Frequency for $\omega = 1.62\times10^6$ s^{-1}. All data taken with 100-μs exposure.*

The ion rotation is plotted versus RMF frequency for a wide range of bias and RMF field strengths in Fig. 6.18. Contrary to what one might expect, the plasma rotation is actually slower at higher RMF frequencies. This trend is even more pronounced when the ratio of the ion rotation frequency to the RMF frequency ω_i/ω is plotted versus the RMF frequency. At low RMF frequency (ω=0.5×10^6 s^{-1}), the ion rotation ranges from 10% to 18% of the RMF frequency, while at the highest RMF frequency (ω=1.6×10^6 s^{-1}) the ion rotation is only 2% of the RMF frequency.

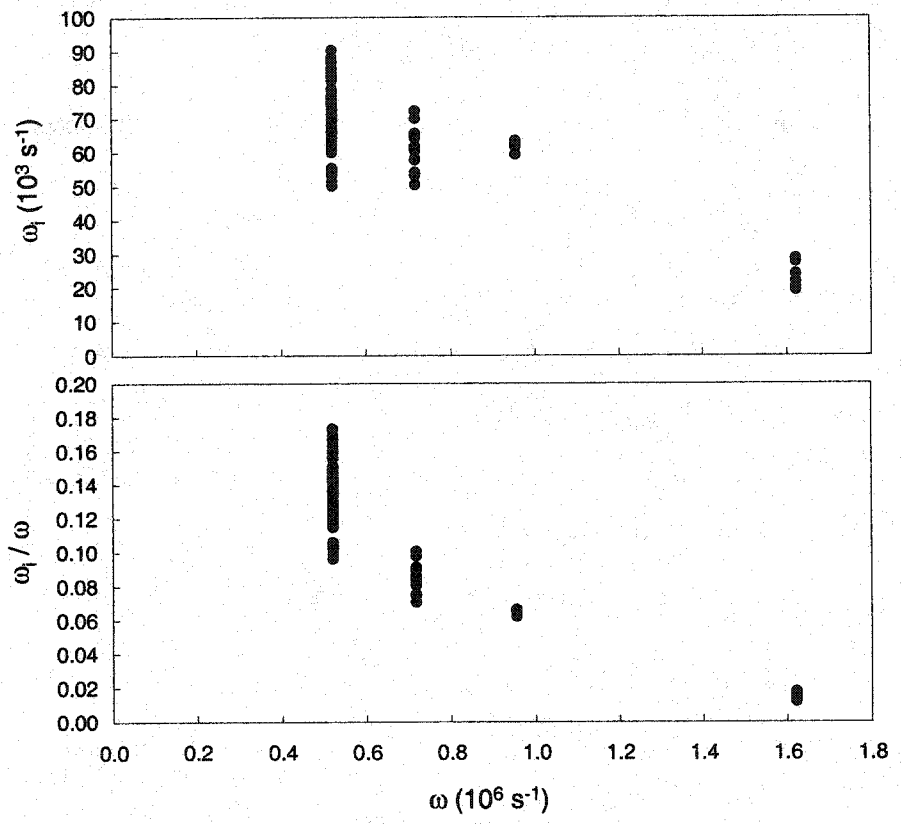

***Figure 6.18**: C-III Rotation Frequency vs. RMF Frequency. t=600-1200 μs.*

In the limit $\omega_{ci} << \omega$, where ω_{ci} is the ion cyclotron frequency in the rotating field, the RMF torque is not applied directly to the ions but rather drives the electrons. If the poloidal flux is steady-state, then the azimuthal electric field must be zero everywhere and the electron azimuthal velocity is steady-state. The applied torque on the electrons must be balanced by electron-ion resistive drag. The ion azimuthal

velocity will reach a steady state when the resistive torque balances the drag torque on the ions, as examined in Sec. 8.3. The scaling of the ion rotation frequency with these torques can be crudely estimated here. The applied RMF torque depends on the field strength B_ω^2 and the penetration depth δ* according to the analytic expression

$$T_{RMF}^{'} \approx \left(1 - e^{-2a/\delta^*}\right)\frac{\delta^*}{a}T_0^{'}; \qquad T_0^{'} \equiv \frac{2\pi r_s^2 B_\omega^2}{\mu_0}. \tag{6.3}$$

Numerically, the penetration depth has been found[40] to vary as $\frac{\delta^*}{a} \approx 0.86\frac{\zeta^{0.2}}{\lambda^{0.6}}$. The applied torque will then be approximately equal to

$$T_{RMF}^{'} \approx 0.86\frac{\zeta^{0.2}}{\lambda^{0.6}}T_0^{'}. \tag{6.4}$$

The ion rotation is plotted against the applied torque, as shown in Fig. 6.19. At the highest RMF frequency, the applied torque is small because B_ω is low. Even if the antenna impedance could be lowered and B_ω at high frequency could be raised to match the field strength at lower frequency shots, the applied torque would still be lower because the penetration depth would be smaller. The fact that the ion rotation does not scale linearly with the applied torque at lower RMF frequencies means that the drag torque is increasing as well.

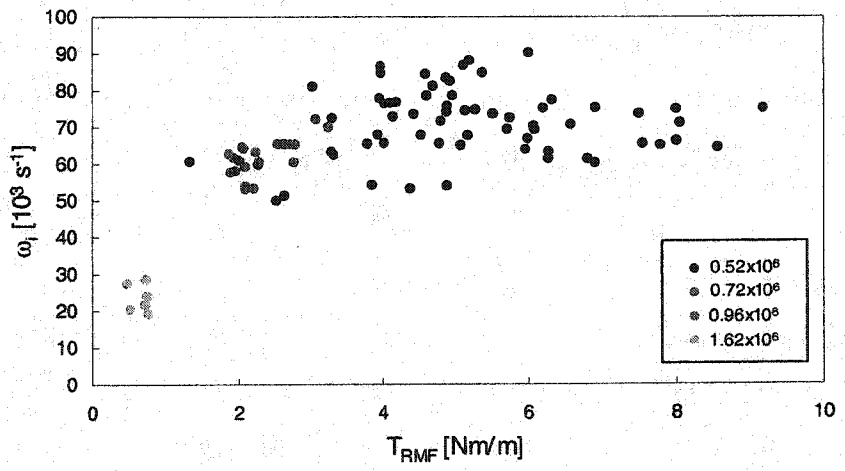

***Figure 6.19**: Ion Rotation Versus Applied Torque. RMF frequencies are shown as different colors. All rotation data for C-III.*

The drag torque due to ion-neutral collisions will roughly scale as

$$T_{in} \approx \frac{\pi}{2}\langle S_{in}\rangle m_i \omega_i r_s^4 \tag{6.5}$$

where the neutrals are assumed stationary and $\langle S_{in}\rangle$ is the average ion-neutral momentum transfer rate. Assuming that ion-neutral collisions are the sole drag mechanism on the ions, then the ion rotation frequency is found by balancing the torques:

$$\omega_i \approx \frac{4B_\omega^2 \zeta^{0.2}}{\mu_0 \langle S_{in}\rangle m_i r_s^2 \lambda^{0.6}}. \tag{6.6}$$

At this point in the analysis, $\langle S_{in}\rangle$ is unknown, although it will be calculated from the neutral Dα emission in Ch. 7 and a much more thorough torque balance will be performed in Ch. 8 including ion viscosity and particle loss.

Continuing with the assumption that ion-neutral drag is the sole braking mechanism on the ions, the required ion-neutral collision rate can be calculated from Eq. (6.6). Defining the ion-neutral collision rate as

$$\langle S_{in}\rangle = n_i n_0 \langle \sigma \mathrm{v}\rangle_{in} \tag{6.7}$$

and using a total ion-neutral collision rate coefficient of $\langle \sigma \mathrm{v}\rangle_{in} \approx 2\times10^{-14}$ m^{-3}, the required neutral density to provide the necessary drag can also be calculated, plotted in Fig. 6.20 versus the plasma density. The required neutral density would be about 2×10^{18} m^{-3}, resulting in a momentum transfer rate $\langle S_{in}\rangle$ of about 5×10^{23} m^{-3}s^{-1}. Neutrals can immediately be ruled out as the sole ion braking mechanism from a simple estimation of the required power to sustain a neutral density this high. Assuming that the ionization and charge-exchange rate coefficients are roughly equal and that the plasma volume is approximately 1 m^3, the required power to sustain an ion-neutral collision rate of this magnitude is about 8 MW, much larger than the input power (calculated in Sec. 7.4). This will be shown conclusively in Ch. 7, where the neutral

density will be independently calculated from the Dα emission. A more thorough torque balance including profile effects and ion viscosity is presented in Ch. 8.

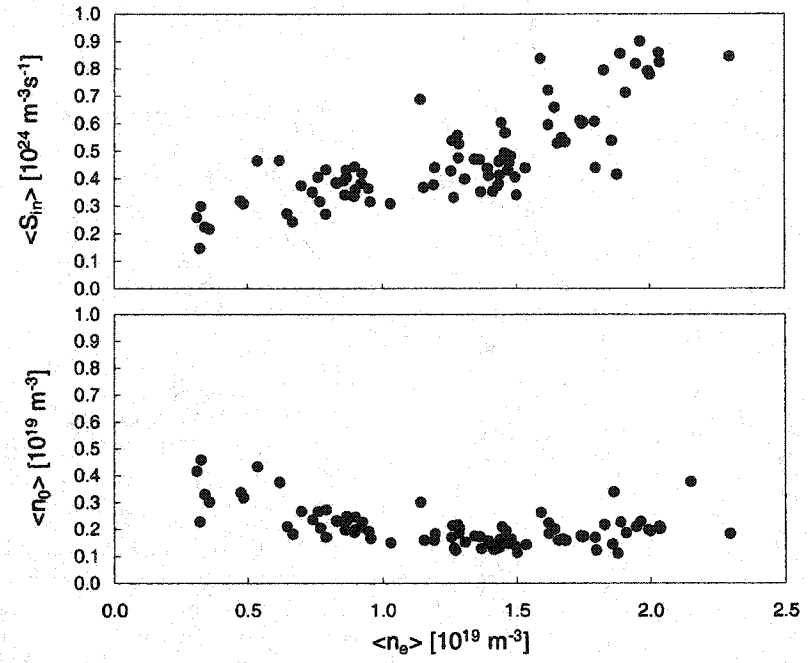

***Figure 6.20**: Required Neutral Drag and Neutral Density. Assumes that neutral drag is the sole ion braking mechanism.*

The ion rotation velocity also appears to scale with the plasma density, as shown in Fig. 6.21. An initial proposed explanation for this was that the total particle inventory is fixed. As the plasma density increases, the neutral particle density decreases along with the corresponding neutral drag torque. This line of reasoning is seen to be faulty, however. As seen in Fig. 6.20, the required neutral density is roughly a constant, independent of the plasma density, while the ion-neutral collision rate scales linearly with plasma density. The reason for the apparent correlation of ion rotation with plasma density is that they both depend on the RMF field B_ω. Balancing the applied torque and the resistive torque, the driven plasma density scales linearly with the RMF strength, given by the empirical formula

$$n_{em}\ [10^{20}\ m^{-3}] = \frac{0.01 B_\omega\ [mT]}{\left(\omega r_s^2\right)^{1/2}}, \tag{6.8}$$

as shown in Fig.6.22. Assuming that the neutral density and ion-neutral rate coefficient are constant, and substituting n_{em} for B_ω in Eq. (6.6) yields the following relationship

$$\frac{\omega_i}{\omega} \propto \frac{n_{em}\zeta^{0.2}}{n_0 \langle \sigma v \rangle_{in} m_i \lambda^{0.6}} \tag{6.9}$$

The ion rotation will appear to scale with plasma density if the neutral density is fixed.

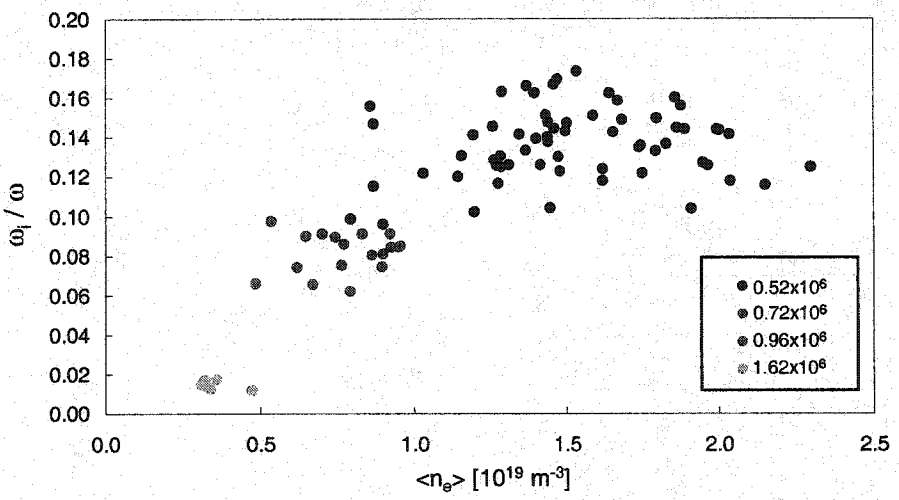

***Figure 6.21**: Apparent Scaling of Rotation with Plasma Density.*

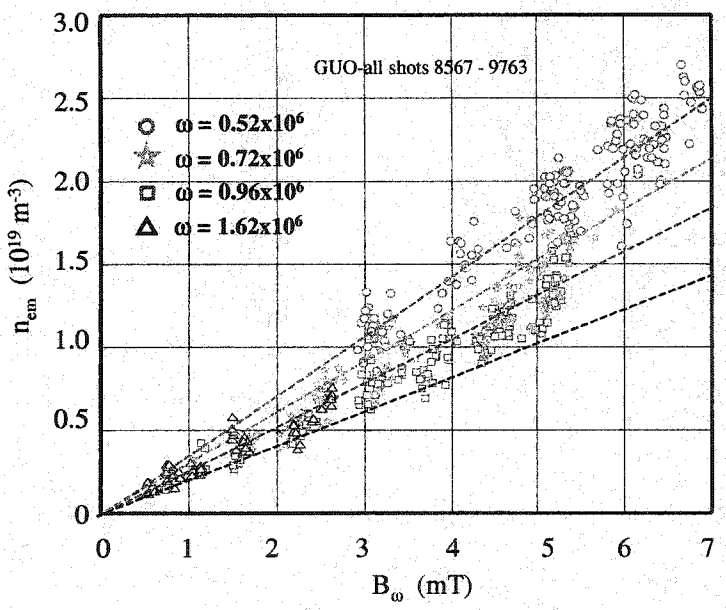

***Figure 6.22**: Peak Density as a Function of RMF Magnitude. Dashed lines are for $n_{em} = 0.01x10^{19} B_\omega(mT)/(\omega r_s^2)^{1/2}$ m^{-3}.*

6.5 Effect of RMF Antenna Length

A series of experiments with varying RMF antenna length was performed on TCS. Three different antenna lengths were used: 0.7 m, 1.0 m, and 1.6 m. Typical plasma conditions for the three antenna lengths are shown in Fig. 6.23. Despite considerable variation in the antenna length, the plasma conditions are similar. The one variable that clearly varies with antenna length is the FRC length, which is always about 20-30 cm longer than the RMF antennas. The FRC length automatically adjusts to be slightly longer than the antennas, presumably to maintain the circular flow pattern necessary for steady-state operation.

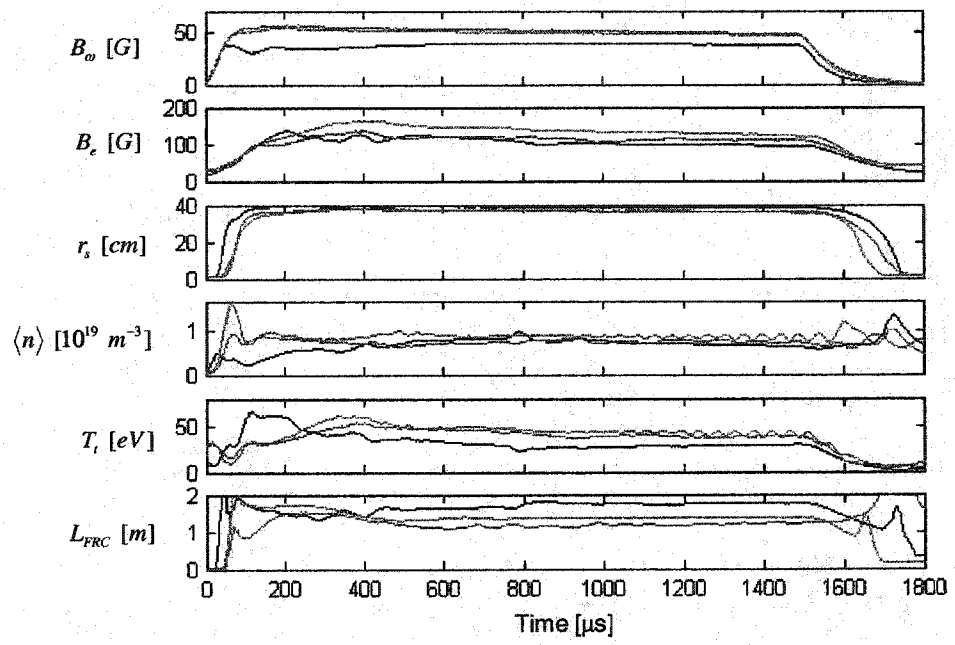

Figure 6.23: *Plasma Properties for Various Antenna Lengths. Black line: 1.6 m (shot 10204). Blue line: 1.0 m (shot 10363). Red line: 0.7 m (shot 10503).*

The resulting ion rotation measured from the Doppler shift of C-III line radiation for the various antenna lengths is shown in Fig. 6.24. There does not seem to be any correlation of ion rotation frequency with RMF antenna length. This can be understood from Fig. 6.25, a plot of the total applied RMF torque for the different antenna lengths. The two short antennas (0.7 m and 1.0 m) both apply the same total

torque, even though B_ω is nearly identical. This implies that the penetration depth for the 0.7 m antenna case has increased and the torque per unit length is higher. The opposite is true for the longest antenna (1.6 m) case, where the total applied torque is actually lower (although B_ω is lower as well). The penetration depth is smaller, as seen in Fig. 6.26. It is clear that the total applied torque does not scale linearly with antenna length, as one might expect. Instead, as the antenna length is shortened, the RMF penetrates the plasma further and applies more torque per unit antenna length.

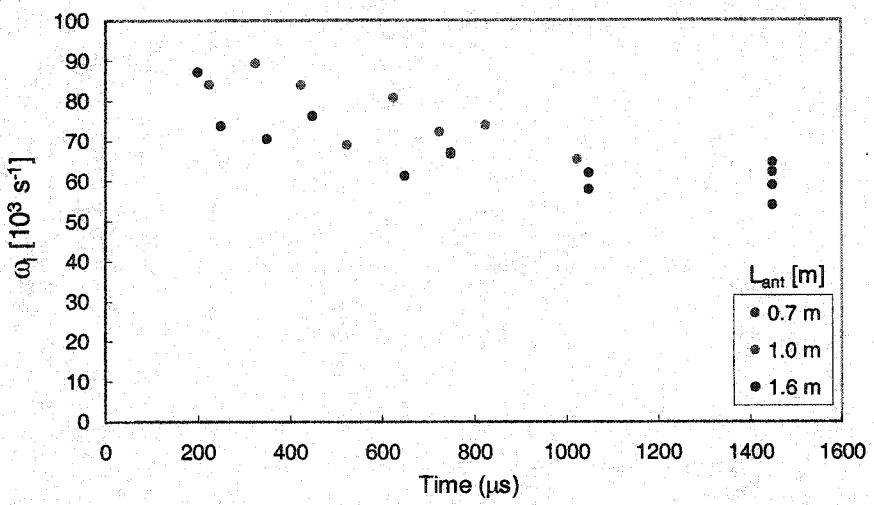

Figure 6.24: *Ion Rotation for Various RMF Antenna Lengths. Rotation data for C-III.*

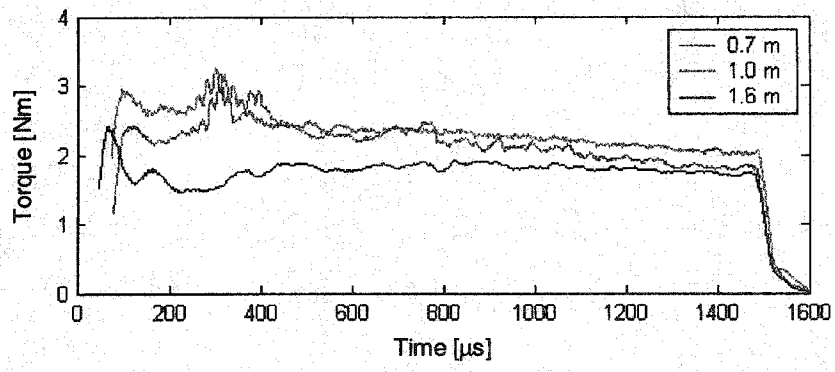

Figure 6.25: *Applied Torque for Various RMF Antenna Lengths.*

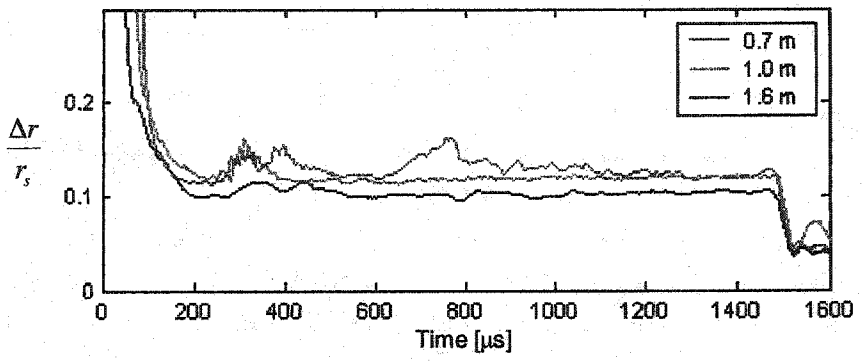

Figure 6.26: *Penetration Depth for Various RMF Antenna Lengths.*

6.6 Rotational Instability

The n=2 rotational instability often develops in the TCS plasma when the separatrix is compressed to more than a few centimeters from the wall. The mode is observed by chord-integrated diagnostics such as the interferometer, monochrometers, and bolometer. Typical results from these diagnostics are shown in Fig. 6.27 for an FRC that developed a rotational instability. A tomographic reconstruction, shown in Fig. 6.28, proves that the instability is indeed the n=2 rotational mode, rotating in the ion paramagnetic direction (the same direction as the RMF). This is in contrast to conventional FRTP-formed FRCs, where the n=2 mode is observed to rotate in the ion diamagnetic direction. The tomographic reconstruction has been limited to three radial and three toroidal modes.

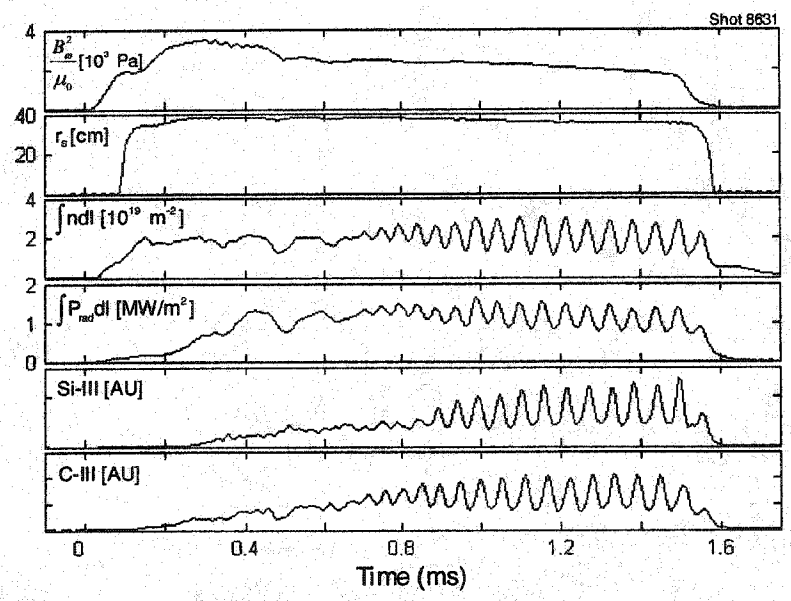

Figure 6.27: *Plasma Parameters During Rotational Instability.*

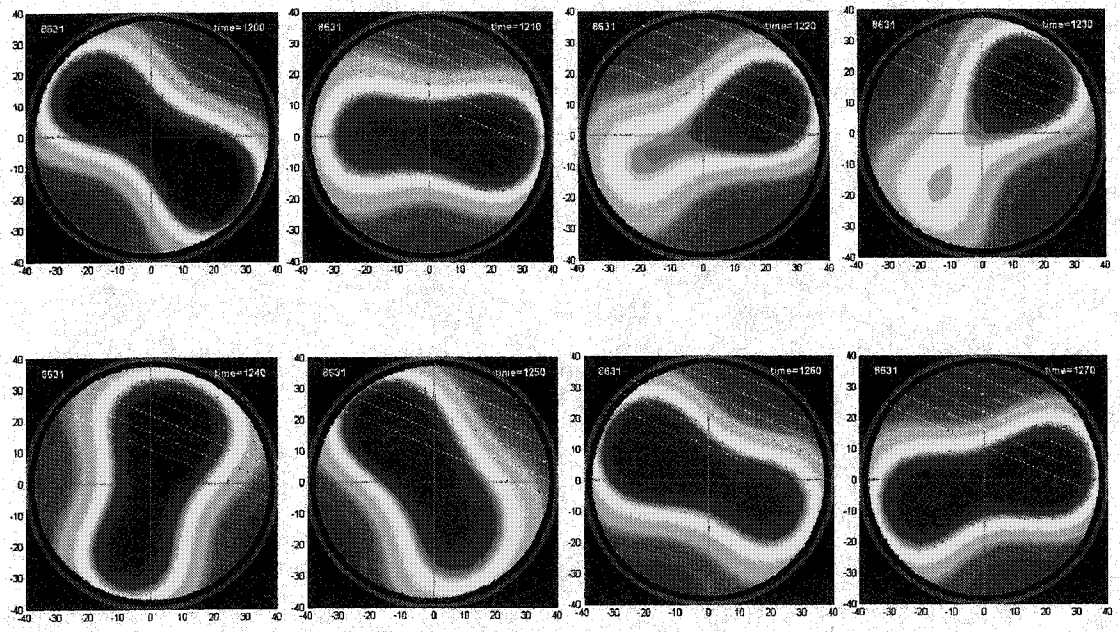

Figure 6.28: *Tomographic Reconstruction of the Rotational Instability. Time advances in 10 μs intervals from left-to-right, top-to-bottom. Reconstruction limited to l=3 radial modes and n=3 toroidal modes. ICCD viewing chords are shown as white dashed lines.*

The rotation frequency of the mode structure is calculated from the power spectral density (PSD) of the chord-integrated brightness measured by a monochrometer viewing the C-III line at 229.687. The PSD shown in Fig. 6.29 was obtained using a fast Fourier transform (FFT) with a window of 256 μs, providing a spectral resolution of ±980 Hz. Also shown is twice the carbon rotation frequency, obtained from the Doppler shift of the same C-III line. The plasma rotation frequency has been doubled to compare with the mode frequency because the chord-integrated diagnostics see two oscillations for every mode rotation. Several things can be inferred from this figure. First, the plasma rotation and the mode rotation are nearly synchronous. Second, the plasma is rotating well before the rotational instability develops. This either is an indication of the growth time of the mode (at least 450 μs), or else that the plasma was wall stabilized early in time and only became unstable as the separatrix radius moved inwards from the wall. Third, the ion rotation and the mode frequency both slow with time. This is because the applied torque decreases as the antennas are loaded and the RMF tank capacitor rings down.

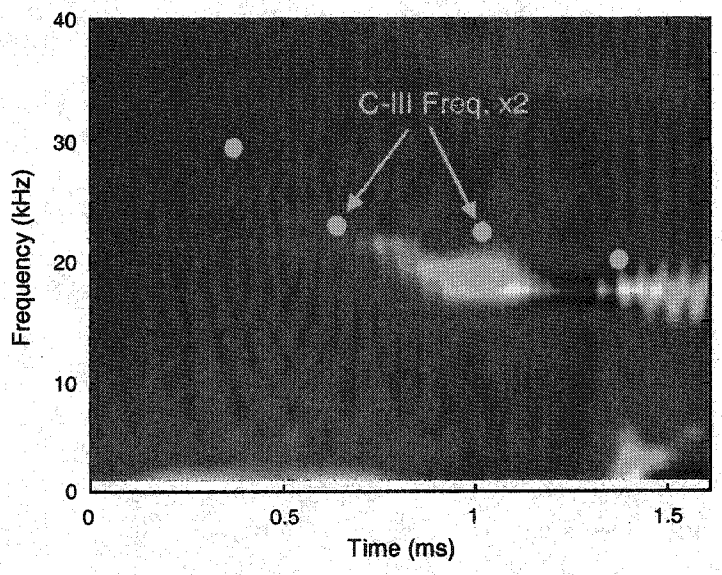

Figure 6.29: *Power Spectral Density of the Rotational Instability. Orange points: Ion rotation frequency x2 to compare with the n=2 mode frequency. Shot 8631.*

The plasma rotation frequency and the n=2 mode frequency are systematically compared in Fig. 6.30. This data was obtained from many different shots, with varying plasma conditions and RMF frequencies. The mode frequency was obtained from the peak of the power spectral density of the interferometer signal, with a spectral resolution of ± 980 Hz, and has been divided by two since the observed mode frequency is twice the actual rotation frequency. In all cases, the plasma rotation and the mode rotation are compared at the same point in time. Although there is considerable scatter, the plasma rotation frequency lies within a standard deviation of 0.87 to 1.20 times the mode frequency. This data rules out any instability theory that predicts a rotational mode with a frequency that differs by more than 20% from the plasma rotation frequency.

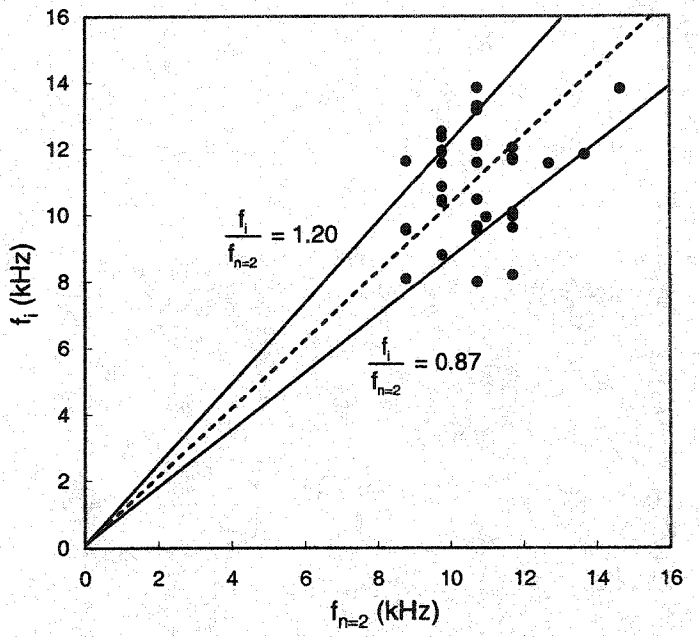

Figure 6.30: *Comparison of Plasma Rotation and Mode Rotation.*

The ion rotation frequency is compared with the ion diamagnetic drift frequency for a rigid rotor current distribution, given in Eq. 2.10. Since these plasmas are wall-stabilized, no definitive conclusions can be made about the stability criterion for RMF-driven FRCs.

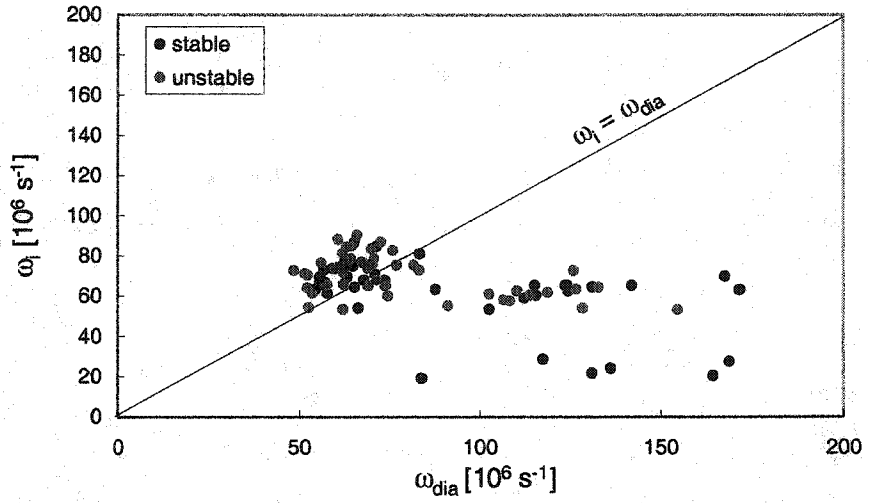

Figure 6.31: *Comparison of Ion Rotation with Diamagnetic Drift Frequency. Black points: plasma remained stable for duration of shot. Red points: n=2 instability developed at some point during the shot.*

Chapter Seven

Neutral Density

Neutral particles can have a strong influence on the plasma rotation rate, especially in these low-density experiments. Unfortunately, the background neutral density is not directly measured. A fast ion gauge at the axial midplane of the confinement chamber cannot provide neutral pressure measurements during the experiment because of interference from the RMF. Gas is puffed in and pre-ionized several meters away in the source section and then allowed to flow along open field lines into the confinement section. Wall loading of deuterium in the quartz vacuum vessel precludes a precise control of the particle inventory. Indeed, experimental results are often insensitive to the puff fill pressure in the source section. The neutral particle density can, however, be estimated from the measured neutral deuterium line radiation. This is a standard technique that relates Balmer series Dα (656.103 nm) emission to the ionization rate. The ionization rate is used to estimate the particle confinement time. If the plasma density profile is known as well, then the neutral density profile can be inferred. The resulting charge-exchange rate can then be calculated.

This chapter is organized as follows. First, the plasma density profile is calculated from the internal magnetic probe data. This calculation includes the effect of radial RMF pressure as well as plasma rotation. In Sec. 7.2, the Dα emission array data is spatially inverted to obtain a Dα emission profile. Combined with the plasma density profile and the appropriate rate coefficients, this yields a neutral density profile. In Sec. 7.3, the net ionization rate and charge exchange rate are calculated. These rates will be used in Sec. 7.4 for a global power balance to check the validity of the neutral density measurement. These results will then be used in Ch. 8 for a global torque balance.

7.1 Plasma Density Profile

In order to calculate the neutral density profile, the plasma density profile will first be needed. The plasma pressure profile is found from the radial component of the MHD momentum equation:

$$\rho \frac{D\mathbf{v}}{Dt} = \boldsymbol{j} \times \boldsymbol{B} - \nabla p \,, \tag{7.1}$$

where ρ is the fluid density and D/Dt is the convective derivative. In a non-rotating, steady-state FRC, the convective derivative is zero. Furthermore, if the axial magnetic field lines are assumed to be straight (no curvature) at the axial midplane, then the $j_\theta \times B_z$ term can be simplified using Ampere's law to substitute for j_θ:

$$j_\theta \times B_z = \frac{(\nabla \times B_z) \times B_z}{\mu_0} = -\frac{\partial}{\partial r}\left(\frac{B_z^2}{2\mu_0}\right). \tag{7.2}$$

In a conventional FRC with no applied RMF, the radial component of Eq. (7.1) can then be integrated to give the traditional radial pressure balance equation for an FRC:

$$p(r) + \frac{B_z^2(r)}{2\mu_0} = \frac{B_e^2}{2\mu_0} \tag{7.3}$$

where B_e is the external axial field.

RMF current drive adds two complications to the calculation of a radial pressure profile. First, there is an additional $j_z \times B_\theta$ term due to the RMF, where j_z and B_θ are both oscillating quantities and so the phase between them must be taken into account. Second, because the RMF torque tends to spin the plasma, centrifugal pressure may become significant and the convective derivative in Eq. (7.1) is no longer negligible. We will deal with the $j_z \times B_\theta$ radial force term first and then calculate the effect of plasma rotation.

The internal magnetic probe provides a direct experimental measurement of the $B_\theta(r)$ profile. However, there is no such direct measurement of $j_z(r)$. It can be calculated from ampere's law,

$$j_z = \frac{1}{\mu_0 r}\left[\frac{\partial(rB_\theta)}{\partial r} - \frac{\partial B_r}{\partial \theta}\right], \tag{7.4}$$

but this requires knowledge of the $B_r(\theta)$ profile. Unfortunately, the internal probe does not measure radial fields. The radial field could be calculated from $\nabla \cdot \boldsymbol{B} = 0$, yielding

$$B_r(r) = -\frac{1}{r}\int \frac{\partial B_\theta}{\partial \theta} dr, \tag{7.5}$$

yet this still requires an azimuthal measurement of B_θ. We could perhaps use the fact that the plasma is rotating past the fixed internal probe. Effectively, this would convert the time history of $B_\theta(t)$ measured at one azimuthal angle into a $B_\theta(\theta)$ profile. This can be very misleading, however, as the plasma rotation is relatively slow compared to the plasma dynamics and oscillations in $B_\theta(t)$. Therefore, this approach is not taken here, and j_z must be estimated from other measured quantities.

Two methods of estimating the oscillating axial current j_z will be presented and then compared. The first solves for j_z from the internal probe data by assuming that the $\partial B_r/\partial\theta$ term in Eq. (7.4) is negligible compared with the $\partial(rB_\theta)/\partial r$ term. This may be justifiable for two reasons. First, in the partially-penetrated case, the magnitude of B_r is much smaller than B_θ. Second, the gradient length scale of $\partial B_r/\partial\theta$ is of the order of the circumference of the FRC, much larger than the gradient length scale of $\partial(rB_\theta)/\partial r$ which may only be a few cm. If the $\partial B_r/\partial\theta$ term in Eq. (7.4) is neglected, then $j_z(r)$ can be solved directly from the internal probe data. The instantaneous RMF radial force is then averaged over an RMF cycle, denoted as $\langle j_z B_\theta \rangle$ and calculated as

$$\langle j_z B_\theta \rangle = \frac{|j_z||B_\theta|}{2}\cos\left(\phi_{j_z} - \phi_{B_\theta}\right) \tag{7.6}$$

where ϕ is the phase of the first order mode of the oscillating quantity.

The second method of estimating j_z is to use an analytic model. Simple analytic expressions for the penetration of a transverse rotating field into a plasma column were presented in Sec. 3.1. Taking the average over an RMF cycle, the RMF radial force using the large ka (small penetration) expressions given in Sec. 3.1 is

$$\langle j_z B_\theta \rangle \approx \frac{2(a/r)B_\omega^2}{\mu_0 \delta^*} e^{-\frac{2(a-r)}{\delta^*}} . \tag{7.7}$$

The vacuum RMF field B_ω is found from the measured antenna current by the relation $B_\omega(\mathrm{G}) = 6.4 I_{ant}(\mathrm{kA})$. Values for a and δ^* are found by fitting the experimentally measured B_θ profile with the analytic expression given in Eq. (3.9). The experimentally measured B_θ profile from the internal magnetic probe and the corresponding fit are shown in Fig. 7.1. The analytic model is only valid up to r = a. Beyond this, assume that j_z is small, thus $\langle j_z B_\theta \rangle_{r>a} = 0$.

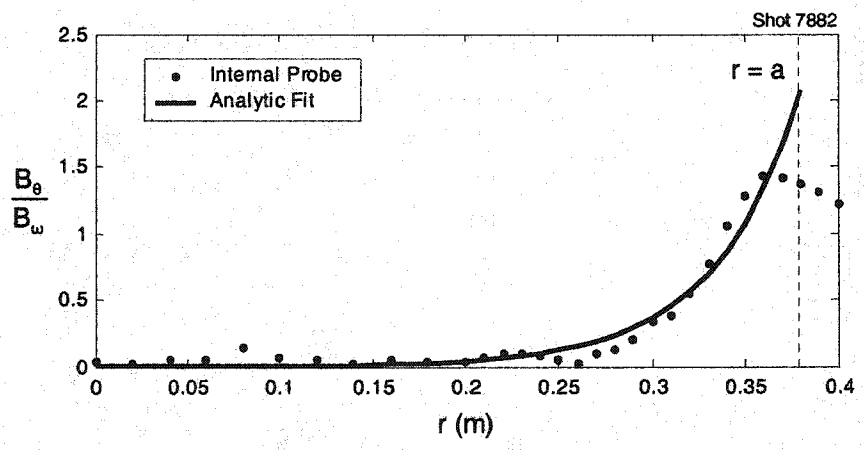

Figure 7.1: *B_θ Profile and Analytic Fit. Also shown is r = a, beyond which the analytic model is no longer valid.*

These two methods of estimating the RMF radial force yield slightly different profiles, as shown in Fig. 7.2. The net pressure contribution for both methods is shown in Fig. 7.3, along with the simple approximation that the net RMF pressure is equal to $\left(B_\omega^2/\mu_0\right)$. The RMF pressure inferred from the internal probe is about 20% lower than

the other two pressure estimates. The discrepancy is small compared with the radial pressure due to the axial magnetic field, which can amount to several hundred Pa.

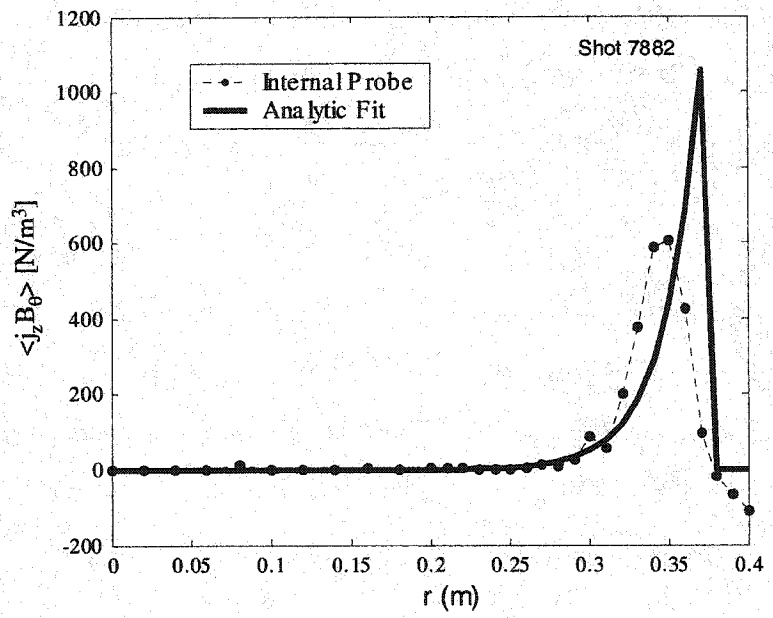

***Figure 7.2**: Comparison of RMF Radial Force Profiles. Dashed line is directly from the internal magnetic probe. Solid line is from the analytic model.*

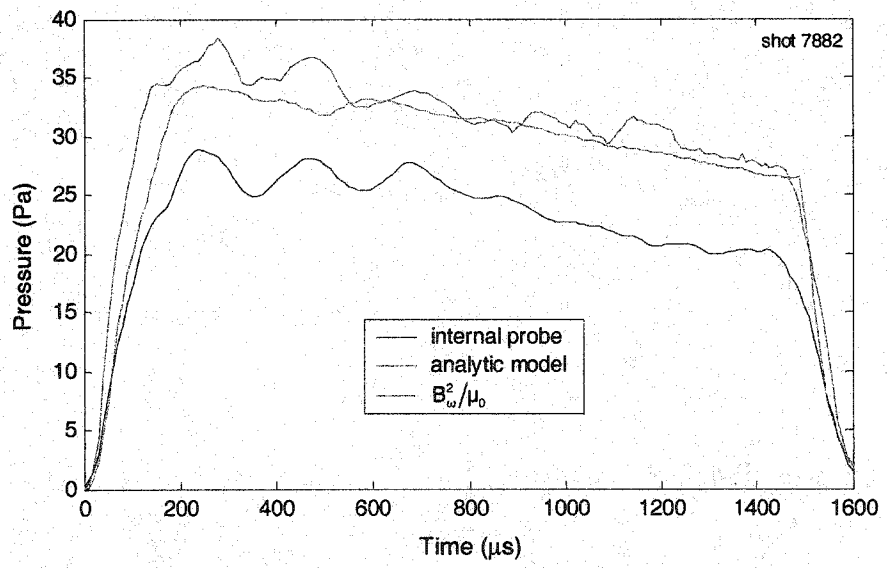

***Figure 7.3**: Net RMF Pressure. Black: estimated from internal magnetic probe. Red: Analytic expression for large ka. Blue: Simple approximation B_ω^2/μ_0*

The second complicating factor in a radial pressure balance is the effect of plasma rotation. The convective derivative in Eq. (7.1) now has a nonzero centrifugal component $(-v_\theta^2/r)$. Assuming that the total temperature T_t is uniform and that the plasma rotates as a rigid body, Eq. (7.1) can now be written as a first order linear inhomogeneous differential equation:

$$k_b T_t \frac{\partial n(r)}{\partial r} = m_i \omega_i^2 n(r) r - \frac{\partial}{\partial r}\left(\frac{B_z^2(r)}{2\mu_0}\right) - \left\langle j_z(r) B_\theta(r)\right\rangle \qquad (7.8)$$

where m_i is the ion mass and ω_i is the plasma rotation frequency. The equation is solved numerically using a second-order Runge-Kutta shooting method. A typical result is shown in Fig. 7.4. The density profile calculated without considering the effect of plasma rotation (by setting $\omega_i = 0$) is also shown for comparison. Including plasma rotation in the analysis lowers the resulting density profile in the center of the FRC and raises the peak density.

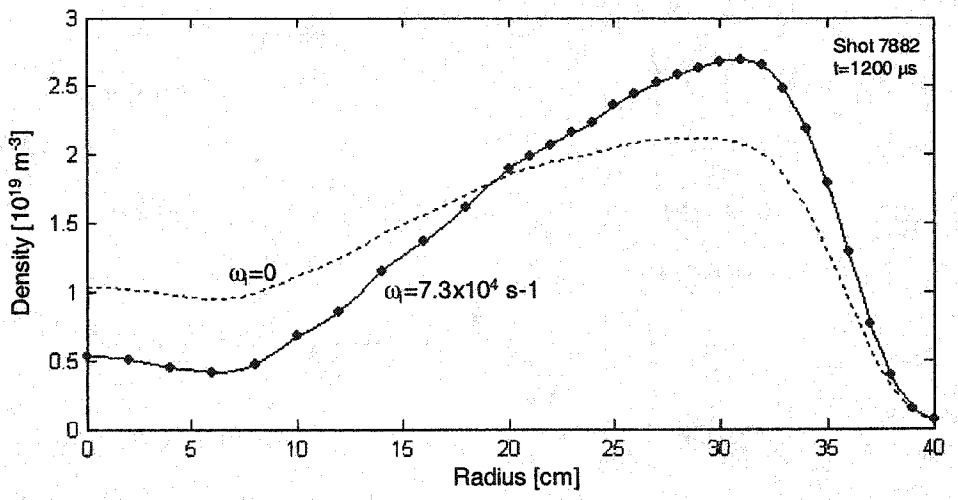

***Figure 7.4**: Typical Plasma Density Profile. Solid line: density profile including the effect of plasma rotation. Black points are actual solution at internal probe data points. Dashed line: density solution without including the effect of ion rotation. Both solutions assume uniform plasma temperature.*

The density profile calculated from Eq. (7.8) can then be integrated as $\int_{-r_w}^{r_w} n(r)dr$, where r_w is the wall radius, and compared with the chord-integrated density obtained from the interferometer. The total temperature is then adjusted iteratively until the computed density integral matches the interferometer data.

7.2 Neutral Density Profile

With the plasma density in hand, the neutral density profile can now be calculated from the measured Dα emission. As described in Sec. 4.3, TCS has an eight-chord array of absolutely calibrated Dα emission detectors. The chord-integrated brightness can be spatially inverted and combined with the density profile and excitation rate coefficient to obtain a neutral density profile.

The Dα detectors measure the chord-integrated brightness at varying impact parameters. Assuming that the Dα emission is axisymmetric and centered at r=0, then the chord-integrated brightness B at impact parameter y is given by

$$B(y) = 2\int_y^{r_w} \varepsilon(r)\frac{rdr}{\left(r^2 - y^2\right)^{1/2}} \tag{7.9}$$

where ε is the local emission and r_w is the wall radius. Eq. (7.9) is the standard Abel transform. The inverse transform is

$$\varepsilon(r) = -\frac{1}{\pi}\int_r^{r_w} \frac{dB}{dy}\frac{dy}{\left(y^2 - r^2\right)^{1/2}}. \tag{7.10}$$

The measured brightness profile B(y) is fit with a smoothing spline with the brightness at the wall forced to zero, as shown in Fig. 7.5. The derivative dB/dy is then computed using center differencing, with a Neumann boundary condition at the geometric axis $\left(dB/dy\right)_{y=0} = 0$. Eq. (7.10) is integrated numerically to give the Dα emission profile, as shown in Fig. 7.6. It should be noted that the profile beyond the outermost chordal

measurement (35 cm) is dependent upon the shape of the spline fit from the last data point to the wall boundary condition.

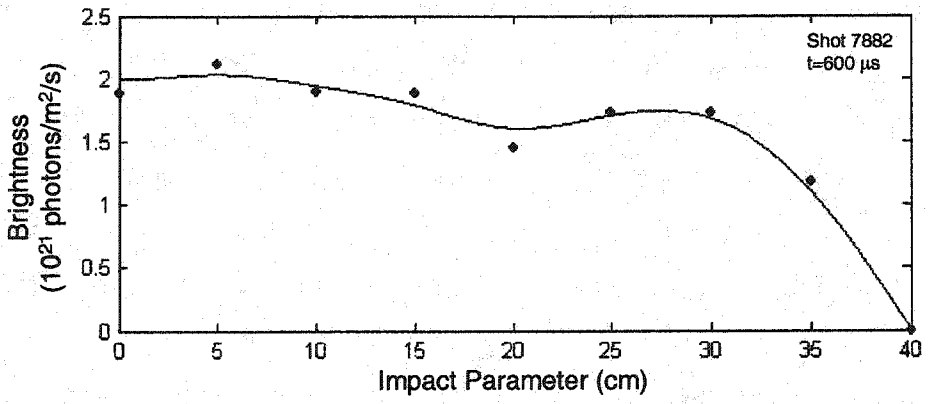

***Figure 7.5**: Dα Brightness Profile. Also shown is a smoothing spline fit to the experimental data with the brightness at the wall set to zero.*

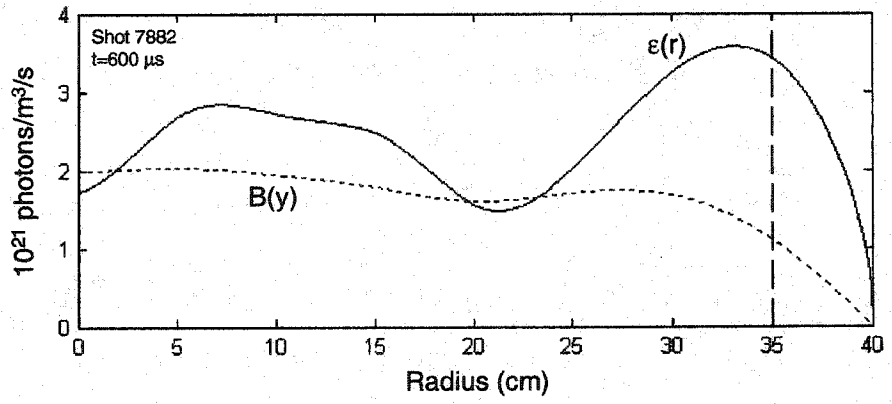

***Figure 7.6**: Abel Inverted Dα Emission Profile. Solid line: Emission profile. Dashed line: Measured brightness. The impact parameter of the outermost detector at 35 cm is shown as a dashed line.*

Assuming that electron-impact excitation is the sole source of Dα emission, then the neutral density can be found from

$$n_0(r) = \frac{\varepsilon(r)}{n_e(r)\langle \sigma v \rangle_{exc}} \tag{7.11}$$

where n_e is the electron density and $\langle \sigma v \rangle_{exc}$ is the rate coefficient for this particular transition. The TCS plasmas are too dense to be in the coronal regime and $\langle \sigma v \rangle_{exc}$ is a function of both electron density and electron temperature. The excitation rate coefficient is obtained from the Johnson-Hinnov factor[41] from the ADAS database, relating the ionization rate coefficient to the excitation rate coefficient as shown in Fig. 7.7. The ionization rate coefficient is assumed to be dominated by single-step ionization in the coronal regime, and is solely a function of electron temperature, as shown in Fig. 7.10. Assuming that the electron temperature is half the total temperature, then Eq. (7.11) can be solved and a typical neutral density profile is shown in Fig. 7.8. The neutral density profile outside of the last viewing chord at 35 cm depends on the slope of the chord-integrated brightness profile. In this analysis, the brightness at the wall (40 cm) has been forced to zero and the gradient scale length is 5 cm. In reality, the brightness gradient may be much shorter, raising the edge neutral density. The average neutral density is the area integral to the wall radius r_w:

$$\langle n_0 \rangle \equiv \frac{2}{r_w^2} \int_0^{r_w} n_0(r) r dr . \tag{7.12}$$

The evolution of the average neutral density is shown in Fig. 7.9. Once steady-state is reached, the average neutral density is about 4.0×10^{17} m^{-3}, or less than 4% of the plasma density.

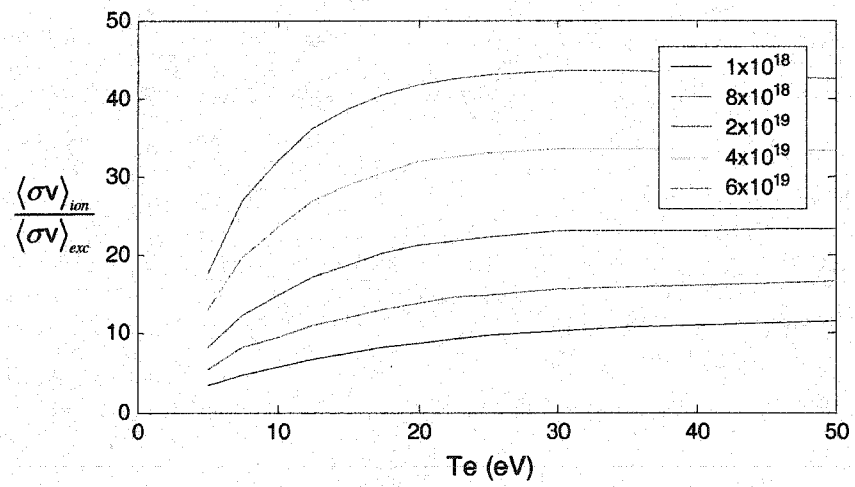

***Figure 7.7**: Johson-Hinnov Factor for Dα. Plotted for various electron densities (m^{-3}).*

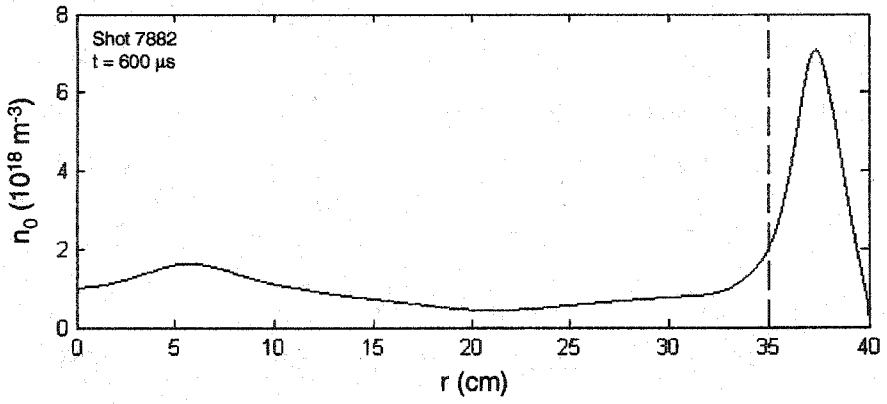

***Figure 7.8**: Neutral Density Profile. Outermost viewing chord at 35-cm impact parameter is shown as a dashed line.*

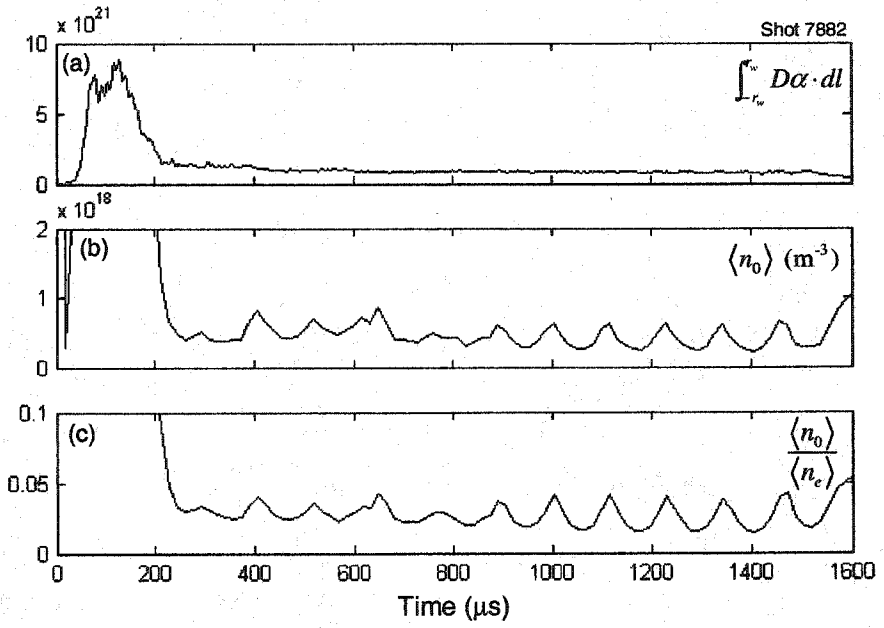

***Figure 7.9**: Average Neutral Density and Neutral Fraction. (a) Chord-integrated Dα emission at the axial midplane and 0 impact parameter. (b) Average neutral density. (c) Average neutral fraction.*

7.3 Ionization and Charge Exchange

With the plasma density and neutral density in hand, the rate of ionization by the reaction $D + e \xrightarrow{ion} D^+ + 2e$ can be found. The local ionization rate S_{ion} is simply

$$S_{ion} = n_e n_0 \langle \sigma v \rangle_{ion} \tag{7.13}$$

where $\langle \sigma v \rangle_{ion}$ is the electron-impact ionization rate coefficient. Using the fact that the ionization rate coefficients for hydrogen and deuterium are equal[42], the ionization rate coefficient for electron-impact ionization of atomic hydrogen from the ground state is shown in Fig. 7.10 versus electron temperature[43]. Likewise, the charge-exchange rate S_{cx} for the reaction $D^+ + D \xrightarrow{cx} D + D^+$ is

$$S_{cx} = n_i n_0 \langle \sigma v \rangle_{cx}, \tag{7.14}$$

where $\langle \sigma v \rangle_{cx}$ is the rate coefficient given in Fig. 7.10 assuming 1 eV neutrals[44].

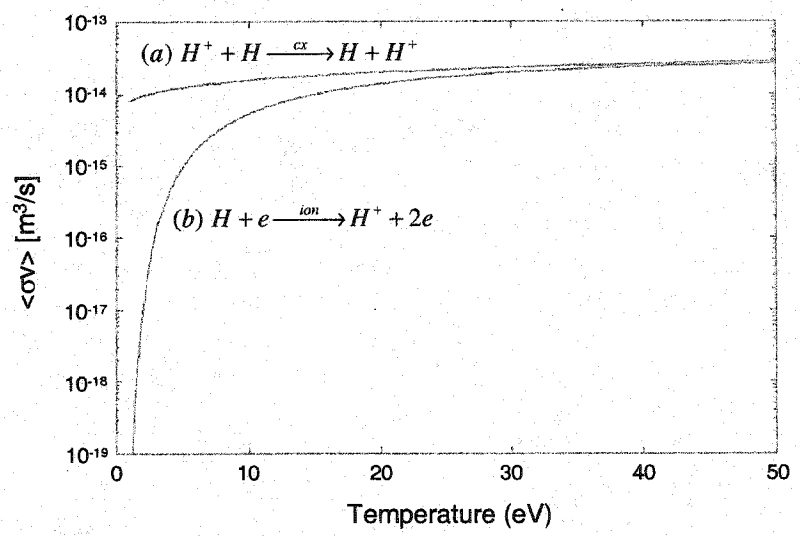

***Figure 7.10**: Hydrogen Rate Coefficients. (a) $\langle \sigma v \rangle_{cx}$ vs. T_i (b) $\langle \sigma v \rangle_{ion}$ vs. T_e*

The local source rates are shown in Fig. 7.11. Assuming axisymmetry, the average source rates are:

$$\begin{aligned} \langle S_{ion} \rangle &\equiv \frac{2}{r_w^2} \int_0^{r_w} S_{ion}(r) r dr \\ \langle S_{cx} \rangle &\equiv \frac{2}{r_w^2} \int_0^{r_w} S_{cx}(r) r dr \end{aligned} \tag{7.15}$$

Because this calculation involved an Abel inversion with high uncertainty outside of 35 cm, the results are compared with a simple zero-dimensional estimate taken from the center Dα chord at 0-cm impact parameter with rate coefficients based on the average

plasma density. The average source rates calculated by both methods are shown in Fig. 7.12. There is good agreement between the chord-integrated value and the average value computed from the spatial inversion. The average ionization rate is about 2.0×10^{22} $m^{-3}s^{-1}$, while the charge-exchange rate is between 0.5×10^{23} and 1×10^{23} $m^{-3}s^{-1}$.

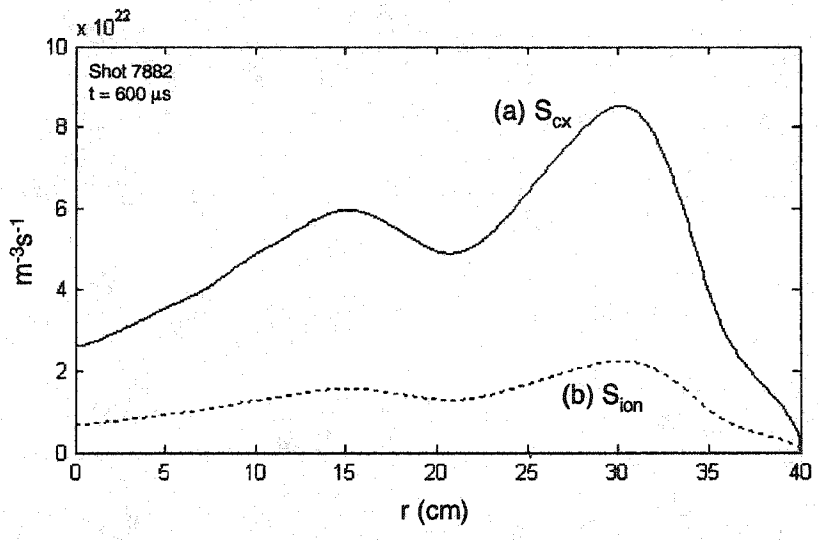

***Figure 7.11**: Plasma Source Rate Profiles. Assumes that $T_i=T_e$*

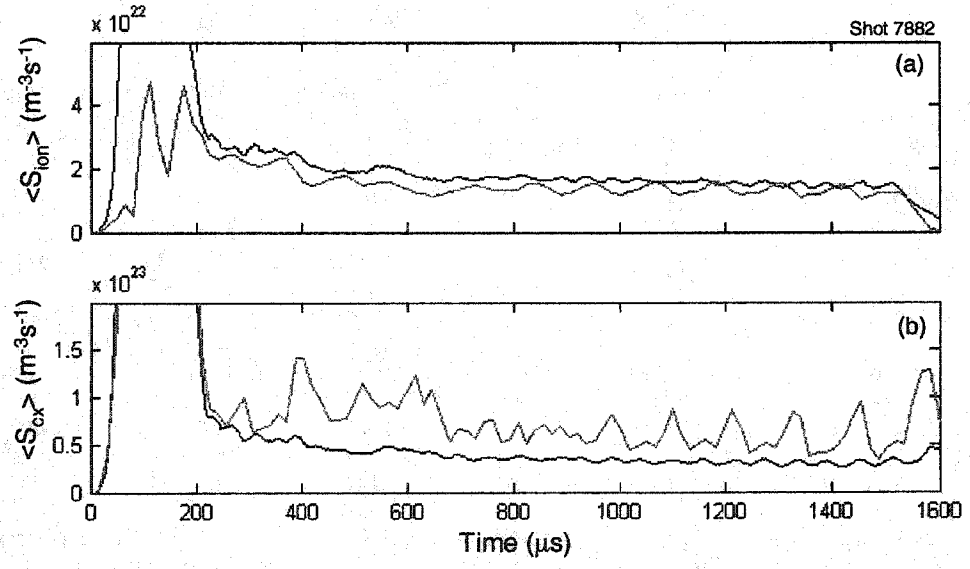

***Figure 7.12**: Average Source Rates. Black curve: chord integrated value. Red curve: Abel Inverted average. (a) Ionization source rate. (b) Charge-exchange rate.*

From the ionization rate, the particle confinement time can be estimated. In steady state, the particle inventory is unchanging and so the particle loss rate must equal the ionization source rate. The particle confinement time τ_N is then

$$\tau_N = \frac{\langle n \rangle}{\langle S_{ion} \rangle} \tag{7.16}$$

where we have assumed axial uniformity. The particle confinement time is found to be quite long at nearly 600 μs, as shown in Fig. 7.13.

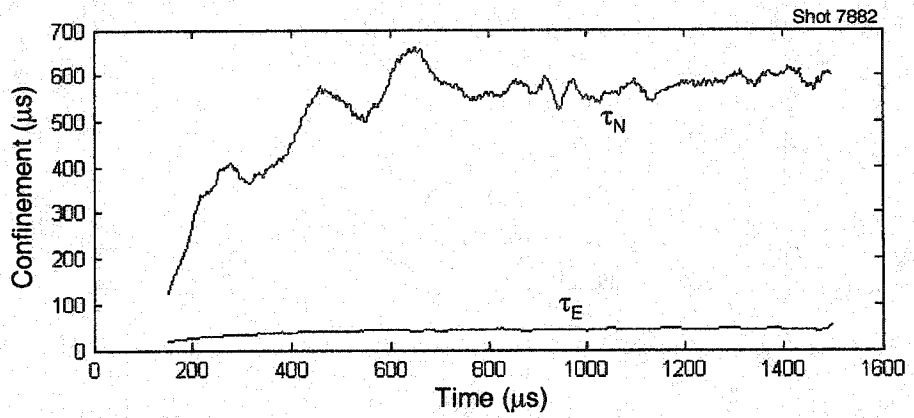

***Figure 7.13**: Typical Confinement Times.*

The above analysis assumed that the background neutral population was atomic hydrogen. If a significant fraction of the neutrals are instead molecular hydrogen, then the resulting ionization rate could be higher. The Johnson-Hinnov factor relating the number of ionizations to the number of Dα photon emissions is an order of magnitude higher for molecular hydrogen than for atomic hydrogen[45]. The above results are thus a lower bound on the ionization rate and an upper bound on the particle confinement time. In the limit where the background neutral gas was pure molecular deuterium, then the ionization rate would be an order of magnitude higher and the particle confinement time would be an order of magnitude shorter. To rule out this possibility, the neutral density and ionization rate based on atomic deuterium are used in a global power balance in the next section.

7.4 Global Power Balance

A global power balance is made to verify the accuracy of the neutral density, ionization rate, and charge exchange rate inferred from the Dα emission. Energy loss rates are based on the neutral density and then balanced with the measured input power from the RMF antennas. The model is zero-dimensional (globally uniform), and includes radiation, ionization, convection, charge exchange, ion conduction, and global energy change (dE/dt) terms. The power balance can then be expressed as

$$P_{RMF} = P_{rad} + P_{ion} + P_{conv} + P_{cx} + P_{cond} + dE/dt\,. \tag{7.17}$$

The input power P_{RMF} is calculated from the slight phase difference between the measured antenna voltage and current[46]. The input power for a vacuum reference shot is set to zero by adjusting the cable lengths, and therefore the phase delay, of the measured signals. In this way, only the power actually delivered to the plasma is considered.

The primary loss mechanism for the TCS plasmas is radiation. This is a combination of impurity line radiation, neutral line radiation, and bremsstrahlung emission. The total radiation is measured by a pinhole bolometer, as described in Sec. 4.3. Since there is only a single chord-integrated measurement of the radiation, no axial or radial profile information is available. Therefore, a zero-dimensional model is made by assuming that the radiation is spatially uniform throughout the FRC.

As described above, the ionization rate is calculated from the measured Dα emission. The average ionization rate is assumed to be uniform throughout the FRC. The ionization power loss P_{ion} is the ionization rate S_{ion} multiplied by the 13.6 eV deuterium ionization energy,

$$P_{ion} = (13.6\ eV)\langle S_{ion}\rangle V_{FRC}\,, \tag{7.18}$$

where V_{FRC} is the FRC volume. Ionization losses due to impurity ionization are not considered.

In steady-state, the particle inventory is unchanging and the particle loss rate equals the ionization rate. Assume that each lost particle convects with it $\frac{3}{2}kT$ of thermal energy, kT of magnetic compression energy (since the ion-electron pair is magnetized), and $\frac{1}{2}m_i v_{i\theta}^2$ of rotational energy. The incoming neutral is assumed to be cold and non-rotating. The convective energy loss rate is then

$$P_{conv} = \left(\frac{5}{2}kT_{total} + \frac{1}{2}m_i v_\theta^2\right)\langle S_{ion}\rangle V_{FRC}. \tag{7.19}$$

The charge-exchange rate was calculated in Sec. 7.4. The neutral reactant is assumed to be cold (1 eV) and non-rotating, while the neutral product is lost and carries with it $\frac{3}{2}kT_i$ of thermal energy and $\frac{1}{2}m_i v_\theta^2$ of rotational energy. In this case, the particle does not carry away any magnetic compression energy because it is a neutral. The charge-exchange energy loss rate is then

$$P_{cx} = \left[\frac{3}{2}k\left(T_i - 1eV\right) + \frac{1}{2}m_i v_\theta^2\right]\langle S_{cx}\rangle V_{FRC}. \tag{7.20}$$

Ion conduction losses can be crudely estimated as well, although neither the ion temperature nor the temperature gradient is directly measured. The ion temperature gradient scale length is assumed to be an ion Larmor radius ρ_i:

$$\frac{dT_i}{dr} \approx \frac{T_i}{\rho_i}. \tag{7.21}$$

Using the classical value for thermal conductivity,

$$K_{\perp i} = \frac{2T_i}{m_i\omega_{ci}^2\tau_i}; \qquad \tau_i = 6.6\text{x}10^{17}\sqrt{\frac{m_i}{m_p}}\frac{T_i^{1.5}[keV]}{n_i \ln\lambda}, \tag{7.22}$$

the conducted power is then independent of ion temperature and depends only on density and the plasma surface area S_{FRC}:

$$P_{cond} = n_i K_{\perp i}\frac{dT_i}{dr} = 1.8\times10^{-31}\frac{n_i^2}{B[G]}S_{FRC}. \tag{7.23}$$

The final term in the power balance is the global FRC energy change. The total energy of the FRC is calculated at each point in time from the magnetic flux arrays. A smoothed time derivative then gives the energy change rate dE/dt.

Results from a typical power balance are shown in Fig. 7.14. The power losses nearly balance the input power, and errors due to profile effects could easily make up the difference. Radiation losses dominate the power balance. The reason for performing this power balance was to verify the accuracy of the calculated neutral density and source rates. Since radiation losses are so dominant, the sensitivity of the power balance to the neutral density (and corresponding ionization and charge-exchange rates) needs to be checked. The neutral density is arbitrarily doubled, and the power balance is again calculated and shown in Fig. 7.15. The energy losses are now too large; therefore, it will be claimed that the calculated neutral density is accurate to within a factor of two.

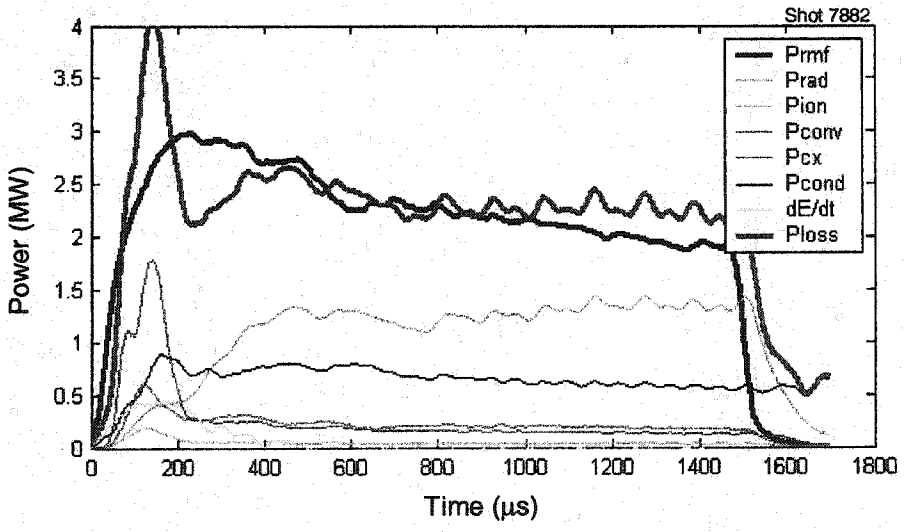

***Figure 7.14**: Global Power Balance. Thick black line: input power from the RMF antennas. Thick red line: Sum of power loss mechanisms.*

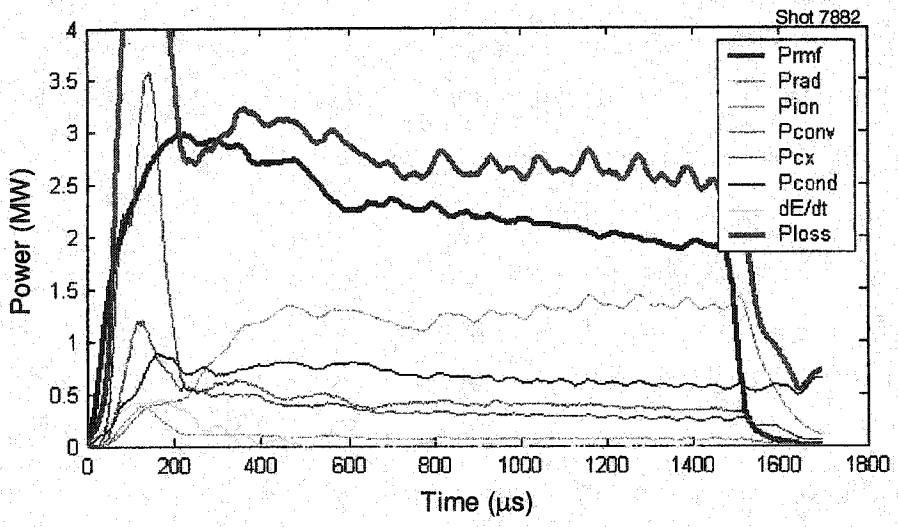

***Figure 7.15**: Global Power Balance with Neutral Density Doubled.*

Chapter Eight

Global Torque Balance

If the FRC poloidal flux is steady state, then the torque applied to the FRC by the rotating magnetic field exactly balances the resistive friction torque. If the ion azimuthal velocity is steady state, then the resistive friction torque must be balanced by the various ion drag mechanisms. In Sec. 8.1, the applied torque is estimated by several methods from the measured field profile. In Sec. 8.2, the drag torque due to ion-neutral interactions is estimated and compared with the applied torque. The neutral drag is found to be insufficient to balance the applied torque. The ion viscosity coefficient is estimated in Sec. 8.3 and viscous drag to the wall is proposed as a possible braking mechanism.

8.1 Applied Torque

The rotating magnetic field imparts a net torque on the FRC. The local azimuthal force applied to the plasma is $\langle j_z B_r \rangle$. Assuming axisymmetry (when averaged over an RMF cycle), the applied torque per unit antenna length is

$$T'_{RMF} = 2\pi \int_0^{r_w} \langle j_z B_r \rangle r^2 dr . \tag{8.1}$$

As described in Ch. 7, the axial current can be calculated from the internal magnetic probe but the radial magnetic field cannot. Since the applied torque cannot be calculated directly from the internal magnetic probe, several methods of estimating the applied torque will be presented and compared.

One way to estimate the applied torque is to fit the analytic expression presented in Sec. 3.1 to the observed B_θ field profile. In this way, the parameters B_ω, a, and δ^* are obtained. This model assumed rigid electron rotation. The analytic expression for the applied torque per unit antenna length is then

$$T'_{RMF} = T_0\left(\frac{\sqrt{2}f(ka)}{ka}\right); \qquad T_0 \equiv \frac{2\pi a^2 B_\omega^2}{\mu_0}, \tag{8.2}$$

where $k \equiv \sqrt{2}/\delta^*$. In the large ka limit, this expression simplifies to

$$T'_{RMF} \approx \frac{\delta^*}{a} T'_0. \tag{8.3}$$

The penetration depth can be estimated without the use of the internal magnetic probe by relating the penetration depth to ζ and λ according to the empirical scaling $\frac{\delta^*}{a} \approx 0.86\frac{\zeta^{0.2}}{\lambda^{0.6}}$. Neglecting end effects, the total applied torque is

$$T_{RMF} \approx 0.86\frac{\zeta^{0.2}}{\lambda^{0.6}} T_0 L_{ant}. \tag{8.4}$$

The resistive torque between the electrons and ions can be estimated if the resistivity is uniform. The applied torque and the resistive torque are equal if three conditions are met. First, the poloidal flux must be steady-state. Second, the RMF must not impart a torque directly on the ions, a condition examined in Sec. 9.1. Finally, electron-neutral friction (due to ionization and elastic collisions) must be negligible compared to electron-ion friction. Assuming these conditions are met and the plasma is axisymmetric, the resistive torque per unit length is

$$T'_\eta = -2\pi \int_0^{r_w} ne\eta_\perp j_\theta r^2 dr. \tag{8.5}$$

The resistivity is estimated from the measured input power, as described by Hoffman[40], and is assumed to be uniform. The expression can be further simplified if the current profile is assumed to be rigid rotor:

$$j_\theta = -ne\omega_r r \tag{8.6}$$

where $\omega_r \equiv \omega_e - \omega_i$ is the difference between the electron and ion rotation frequencies. Eq. (8.5) then simplifies to

$$T'_\eta = 2\pi \int_0^{r_w} \frac{1}{\omega_r}\eta_\perp j_\theta^2 r dr = \frac{P_{abs\theta}}{\omega_r L_{FRC}}, \tag{8.7}$$

where $P_{abs\theta}$ is the component of the absorbed power due to azimuthal current, typically about half of the total absorbed power, and L_{FRC} is the FRC length. The resistive torque is obtained from external quantities from

$$T_\eta \approx \frac{P_{abs\theta}}{\omega\zeta}. \tag{8.8}$$

The applied torque is calculated by both methods and compared for two different plasmas; the plasma parameters for these two shots are shown in Fig. 8.1. Shot 7882, shown as a black line, has a strong B_ω and therefore a high applied torque. The high torque can sustain a high plasma density (nearly 2×10^{19} m^{-3}), but the temperature remains low due to high radiation losses. In contrast, shot 10160 (shown in red) is a low-torque case, with a lower resulting plasma density. Both plasmas are observed to rotate with the same frequency $\omega_i=7\times10^4$ s^{-1}, based on C-III Doppler shift measurements.

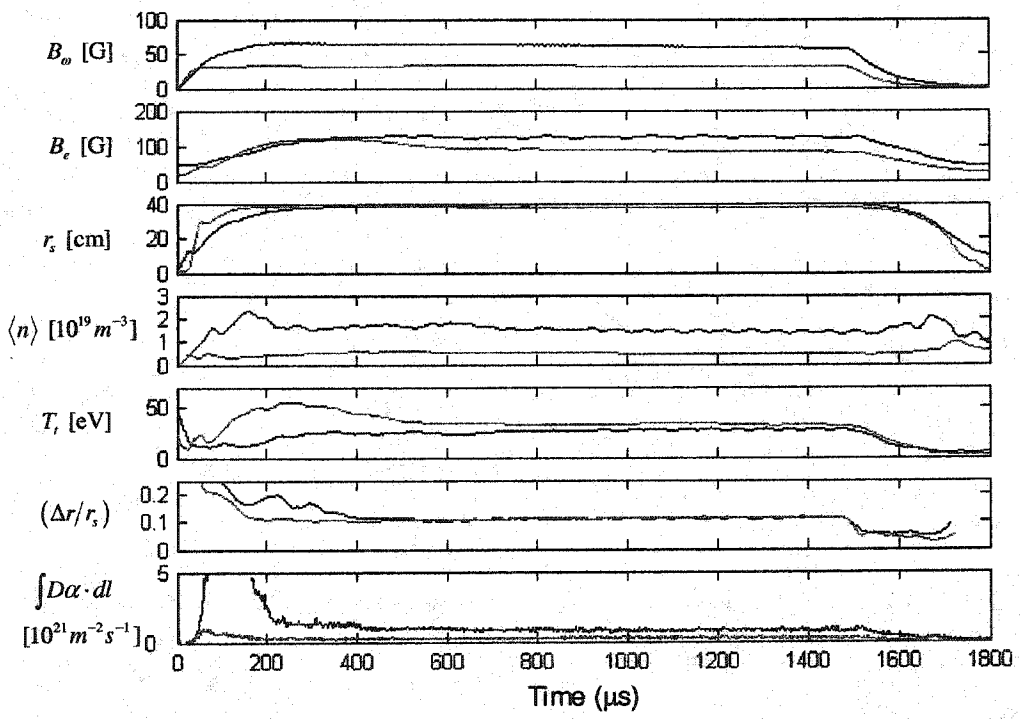

***Figure 8.1**: Plasma Parameters for Torque Balance. Black line: Shot 7882. Red line: Shot 10160. RMF frequency $\omega=0.52\times10^6$ s^{-1}.*

The applied torque for the high-torque condition (shot 7882) is computed by both methods and compared in Fig. 8.2. The applied torque based on the analytic model and the observed penetration depth is about 5 Nm. The torque based on the absorbed power is much higher than the torque based on the internal field. The simplest explanation for this disagreement is that the power-based torque given in Eq. (8.8) is computed in terms of the average electron frequency $\langle \omega_e \rangle = \omega\zeta$. In actuality, the torque is applied at the outer edge of the plasma, where the electrons are nearly synchronous with the RMF and the local ω_e is much higher than the average value, as shown in Fig. 8.3.

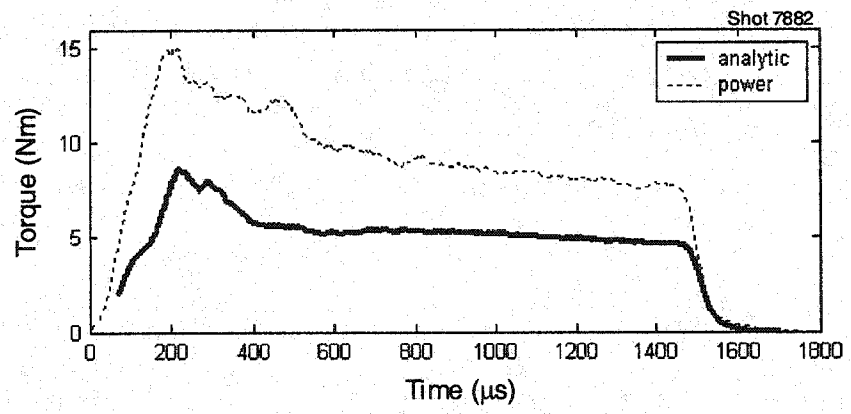

***Figure 8.2**: Applied RMF Torque. Solid line: Based on analytic expression and observed penetration depth. Dotted line: based on absorbed power.*

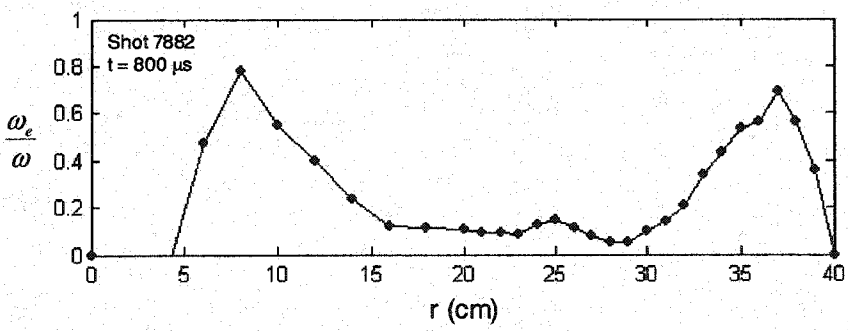

***Figure 8.3**: Electron Rotation Profile. Based on calculated current profile, calculated density profile, and rigid ion rotation $\omega_i = 7 \times 10^4\ s^{-1}$.*

The applied torque for a low-torque case is shown in Fig. 8.4. The torque based on the analytic model is about 1.5 Nm, while the torque based on the absorbed power is again an overestimation. The applied torque will therefore be based on Eq. (8.4).

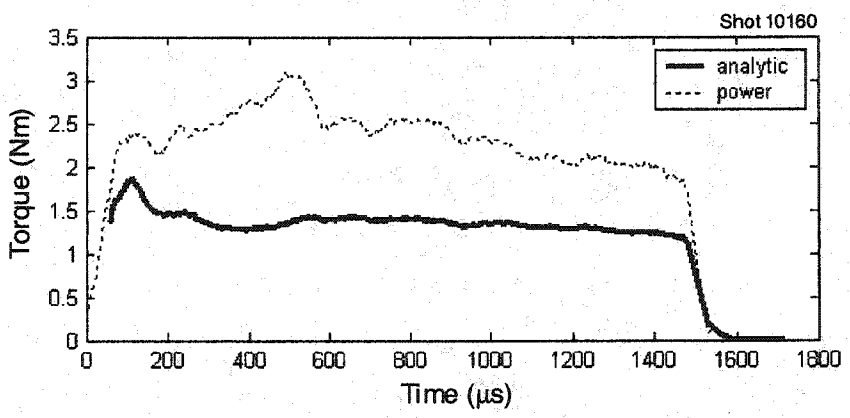

***Figure 8.4**: Applied RMF Torque for Low-torque Case. Solid line: Based on analytic expression and observed penetration depth. Dotted line: based on absorbed power.*

8.2 Neutral Drag

Ion-neutral friction has been proposed as a braking mechanism[10]. The background neutral density and resulting charge-exchange and ionization rates have been calculated from an array of absolutely calibrated Dα detectors, as described in Ch. 7. The neutral density has been verified with a global power balance in Sec. 7.4. Although this global model does not prove that the neutral density is correct, it does indicate that the neutral density is at least plausible. Since there are no axial profile measurements available, the neutral drag will be assumed to be globally uniform along the length of the FRC. In all cases, the FRC is longer than the RMF antenna, thought to be necessary to maintain a steady radial flow pattern.

The ion-neutral collision torque T_{in} is the sum of the resonant charge-exchange and elastic ion-neutral collision torques. The charge-exchange rate is obtained from the Dα emission as described in Sec. 7.3. Assume that the incoming neutrals are cold (1 eV) and non-rotating, and that the charge-exchange neutral is immediately lost along

with all of its angular momentum. Assuming axisymmetry, the drag torque due to charge exchange is then the area integral of the angular momentum loss rate:

$$\begin{aligned} T_{cx} &= -2\pi L_{FRC} \int_0^{r_w} S_{cx} \left(m_i \mathrm{v}_{i\theta} r\right) r dr \\ &= -2\pi L_{FRC} \int_0^{r_w} S_{cx} m_i \omega_i r^3 dr \end{aligned} \tag{8.9}$$

where L_{FRC} is the FRC length and the charge-exchange profile $S_{cx}(r)$ was calculated in Sec. 7.3. There may be an additional momentum loss due to ion-neutral elastic collisions. A common assumption[47] for plasmas in the 1-10 eV range is that the elastic scattering and charge-exchange cross-sections are equal. The total torque due to ion-neutral momentum scattering is then twice the charge-exchange torque:

$$T_{in} \approx 2T_{cx} = -4\pi L_{FRC} \int_0^{r_w} S_{cx}(r) m_i \omega_i r^3 dr \,. \tag{8.10}$$

While the net charge-exchange rate has been verified with the global power balance, the charge-exchange profile may have significant errors due to the spatial inversion. It is possible that most of the charge-exchange is occurring at the outer edge of the plasma, beyond the last Dα measurement at 35 cm. This is unlikely, however, since the neutral mean-free-path in these low-density experiments is quite long. Using a charge-exchange cross section of 3×10^{-19} m^2, the mean-free-path is given by

$$\lambda_{mfp} = \left(n_i \sigma_{cx}\right)^{-1} \tag{8.11}$$

and is approximately equal to the plasma radius. The charge-exchange profile shown in Fig. 7.11 is therefore quite reasonable.

The ionization rate profile $S_{ion}(r)$ has been calculated in Sec. 7.3. In steady-state, the particle loss rate equals the ionization rate. Fueling only puts a net torque on the plasma if the incoming neutrals have negligible angular momentum and the lost particles have angular momentum. No information is presently available about where the ions are lost and how much angular momentum is carried away with them. Since the RMF puts a strong inward radial force on the ions, the particles could be lost out of an axial jet at the ends of the FRC rather than at the separatrix. Ions lost at the axis

would carry away negligible angular momentum and the net torque due to fueling would be small. On the other hand, the FRC is longer than the RMF antenna and may be in a "bubble mode," with particles being lost near the separatrix at the ends of the plasma. Since no data is available about where particles are lost, the torque due to fueling will be calculated by integrating the ionization profile. Assuming axisymmetry, the fueling torque is

$$T_f = -2\pi L_{FRC} \int_0^{r_w} S_{ion}(r) m_i \omega_i r^3 dr . \tag{8.12}$$

The neutral drag torque is compared with the applied torque for the two plasmas in Fig. 8.5. In the high-torque, high-density case, neutral drag can account for about half of the total applied torque. In the low-torque, low-density plasma shown in Fig. 8.5(b), neutral drag only accounts for about 25% of the applied torque. One possible explanation is that the background neutral density is independent of the plasma density. The Dα emission and neutral drag both depend on the product of plasma density and neutral density. The background neutral density could be roughly constant late in the discharge, independent of puff-fill pressure or plasma density. The neutrals late in the discharge could be outgassed from the wall, possibly as adsorbed D, D_2, H_2, or dissociated H_2O. Further evidence of wall outgassing comes from the high H/D fraction of ~30% at the edge, deduced from the Balmer α lines as described in Sec. 6.2, even though the puff fill is 99.99% pure D_2. The neutral density could be independent of the plasma density simply because the plasma is semi-transparent to the neutrals. The neutral mean-free-path, given by Eq. (8.11), is longer than the plasma radius.

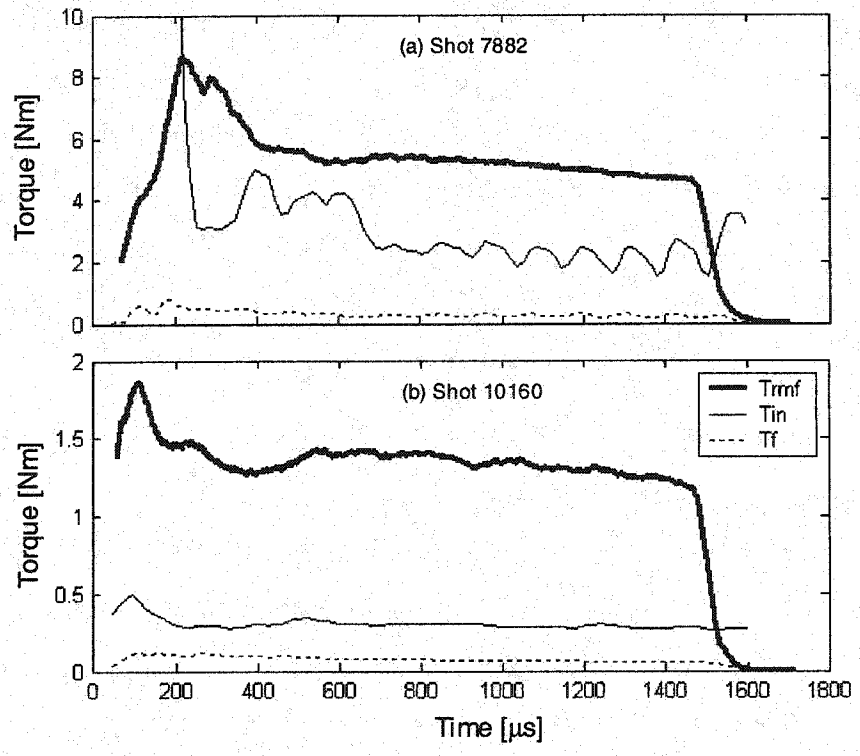

***Figure 8.5**: Neutral Drag Torque. (a) Shot 7882. (b) Shot 10160. Thick line: applied RMF torque. Thin line: ion-neutral collision torque. Dashed line: fueling torque.*

The estimation of neutral drag torque assumes that the plasma is composed of pure deuterium ions, while the background neutrals are pure deuterium atoms. The impurity contribution to the torque balance is neglected. This may be justifiable for several reasons. First, it is hoped that the impurity species are a small concentration of the deuterium plasma. The only impurity concentration known with any precision is carbon, which has been measured between 0.5% and 2% particle concentration[40]. Because carbon is six times as massive as deuterium, carbon could represent up to 12% of the net angular momentum of the FRC. Even if impurities comprise a significant fraction of the angular momentum, they still may be negligible in the torque balance. Table 8.1 lists various rate coefficients for hydrogen and carbon. The electron-impact ionization rate coefficient for hydrogen and carbon are roughly the same, so the carbon confinement time cannot be significantly shorter than the deuterium confinement time.

Thus, including the effect of carbon would increase the particle loss torque by a maximum of 12%. The $C^+ + H \rightarrow C + H^+$ charge-exchange rate coefficient is an order of magnitude larger than the corresponding hydrogen charge-exchange rate coefficient. The fraction of carbon in this ionization state is unknown, but assume for a moment that all the carbon is singly ionized (which clearly is not the case, since radiation from C^{+2} is observed). The maximum carbon charge-exchange rate $S_{cx}(carbon) = n_{C+} n_H \langle \sigma v \rangle_{cx}$ would still be only 20% of the hydrogen charge-exchange rate. Including carbon could increase the charge-exchange torque by an absolute maximum of 120%. Thus, even with the addition of impurities, ion-neutral drag still cannot be the sole braking mechanism on the plasma for Shot 10160.

***Table 8.1**: Typical Rate Coefficients. Values shown are for $T_e = T_i = 20$ eV, $T_0 = 1$eV.*

Reaction	$\langle \sigma v \rangle$ [m^3/s]	Ref.
$H + e \rightarrow H^+ + 2e$	1.4×10^{-14}	43
$C + e \rightarrow C^+ + 2e$	3.3×10^{-14}	43
$H^+ + H \rightarrow H + H^+$	2.0×10^{-14}	44
$C^+ + H \rightarrow C + H^+$	2.0×10^{-13}	50
$C^{+2} + H \rightarrow C^+ + H^+$	9.3×10^{-16}	50

8.3 Viscous Torque

Ion viscosity could be a significant component of the torque balance. This is suggested by several observations. First, the ion azimuthal velocity profile is observed to be rigid rotor, even though the electron velocity profile is not. In the partially penetrated case, the edge electrons are nearly synchronous with the RMF, while the inner electrons rotate more slowly. If the resistivity is uniform, then the resistive torque on the ions is much higher at the edge. If ion viscosity were negligible, one would expect an ion rotation profile that mirrored the electron rotation profile. Second, a wide

range of impurity species and ionization states are observed to rotate synchronously, as described in Sec. 6.1. The electron-ion friction and neutral drag are likely very different for these impurities, yet they all rotate as rigid bodies with the same frequency, implying a high ion-ion viscosity.

To estimate the viscous drag to the wall, we assume laminar viscous flow at the boundary and that the plasma can be modeled as a Newtonian fluid. Furthermore, if the edge velocity gradient length is small compared to the radius of curvature of the wall, then the flow can be modeled as planar flow, as shown in Fig. 8.6. A no-slip boundary condition is imposed at the wall, while the boundary condition at some small distance δr away is $v = \omega_i r_w$. The solution for these boundary conditions is the well-known planar Couette flow, which results in a linear velocity profile as shown in Fig. 8.6. Assuming uniform viscosity μ, the viscous shear stress τ_w at the wall is

$$\tau_w \approx \mu \frac{\partial v_\theta}{\partial r} = \mu \frac{\omega_i r_w}{\delta r}. \tag{8.13}$$

The viscous torque is the product of the shear stress at the wall times the wall radius times the wall area:

$$T'_{visc} = -\tau_w r_w (2\pi r_w) = -T_{v0}\left(\frac{r_w}{\delta r}\right), \tag{8.14}$$

with T_{v0} defined as

$$T_{v0} \equiv 2\pi\mu\omega_i r_w^2. \tag{8.15}$$

The viscous torque depends inversely on the gradient length δr and is linear with the viscosity coefficient μ. The ion velocity profile is often observed to be rigid rotor up to the outermost chordal measurement at 35 cm, while the quartz vacuum boundary is at 40 cm radius. The maximum gradient length δr is then 5 cm, which would yield a minimum viscous torque of $T'_{min} = -8T_0$. The minimum gradient length scale is unknown. Variation of the gradient length scale is probably not as significant as the considerable variation in the ion viscosity coefficient, as will be seen below.

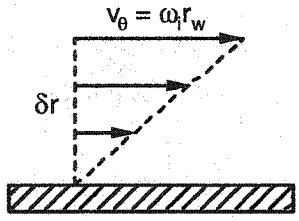

***Figure 8.6**: Plane Couette Flow.*

The ion viscosity coefficient will be estimated assuming that the magnetic field is in the axial direction. Although the instantaneous field at the edge has a radial component as well, the ions do not respond to this field provided that $\omega_{ci} << \omega$, where ω_{ci} is the ion cyclotron frequency in the *radial* component of the RMF. The classical cross-field viscosity for a given magnetization is given by Braginskii[48]

$$\mu_\perp = nk_b T_i \tau_{ii} \left(\tfrac{24}{5} x^2 + 2.23 \right) / \Delta \tag{8.16}$$

where x is the ion magnetization:

$$x \equiv \omega_{ci} \tau_{ii} \tag{8.17}$$

and we have switched to a definition of ω_{ci} as the ion cyclotron frequency in the *axial* field. The classical ion-ion collision time τ_{ii} is

$$\tau_{ii} = \frac{3 \times 10^{12}}{(\ln \lambda / 10)} \sqrt{\frac{m_i}{2m_p}} \frac{T_i^{1.5}(eV)}{Z^3 n_e}, \tag{8.18}$$

where Δ is a function defined by

$$\Delta \equiv 16x^4 + 16.12x^2 + 2.33 . \tag{8.19}$$

In the magnetized limit, viscosity is governed by the ion gyroradius and scales as

$$\mu \propto \frac{n_{edge}^2 m_i^{3/2}}{B^2 T_i^{1/2}} \qquad (\omega_{ci} \tau_{ii} \gg 1), \tag{8.20}$$

while in the unmagnetized limit viscosity is governed by the collisional mean free path and is independent of density:

$$\mu \propto m_i^{1/2} T_i^{5/2} \qquad (\omega_{ci} \tau_{ii} \ll 1). \tag{8.21}$$

For the edge conditions in TCS, the magnetic field and ion temperature are low enough that the plasma may not be in the magnetized limit, particularly for massive impurities. The viscous torque that can be transferred to the wall is shown in Fig. 8.7 as a function of edge ion density and edge ion temperature. Both of these quantities are unfortunately not measured in TCS to any degree of accuracy. Fig. 8.7 simply shows what edge density and temperature are required for viscous torque to be sufficient to balance a given applied torque. The curves in Fig. 8.7 are generated using an axial field B_e=150 G, an ion rotation frequency $\omega_i=7\times10^4$ s^{-1}, and a velocity gradient length scale δr=2.5 cm. The solid lines are for pure deuterium at various ion temperatures, while the dashed lines are for pure O-II plasma. The viscosity for oxygen is higher because it is magnetized in this field at low density, and magnetized viscosity scales as $m_i^{3/2}$.

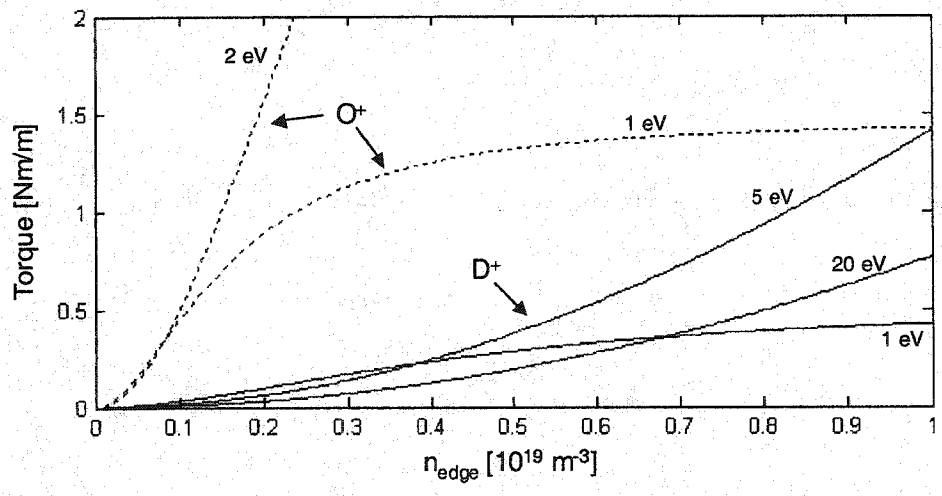

***Figure 8.7**: Viscous Torque for Typical TCS Conditions. Solid lines: Deuterium viscous torque to wall. Dashed lines: Oxygen viscosity to wall, with τ_{ii} set by O^+--O^+ collisions. All curves for B_e=150 G, $\omega_i=7\times10^4$ s^{-1}, and δr=2.5 cm*

In both plasmas considered above in Fig. 8.5, neutral drag alone cannot balance the applied torque. In shot 7882 (the high applied torque case shown in black in Fig. 8.1), there is a 3-Nm difference between the applied torque and the neutral drag torque. The FRC is 2.0-m long; therefore, about 1.5 Nm/m of drag torque per unit length is

needed from some other braking mechanism. Assuming pure deuterium, this would require a wall plasma density of at least 1×10^{19} m^{-3} for wall viscosity to be sufficient to explain the observed ion rotation. The plasma density profile for this plasma was computed from the internal magnetic probe measurements and is shown in Fig. 7.4. At the axial midplane, the plasma density at the wall is certainly not this high, and is more like 1×10^{18} m^{-3}. The plasma in Shot 10160 is 1.75-m long, and so has about 0.6 Nm/m of applied torque per unit length that is not accounted for by neutral drag. With pure deuterium, this would require an edge density of at least 6×10^{18} m^{-3}. The density profile calculated from the internal magnetic probe is shown in Fig. 8.8. The edge density at the axial midplane and assuming uniform plasma temperature is only ~3×10^{18} m^{-3}.

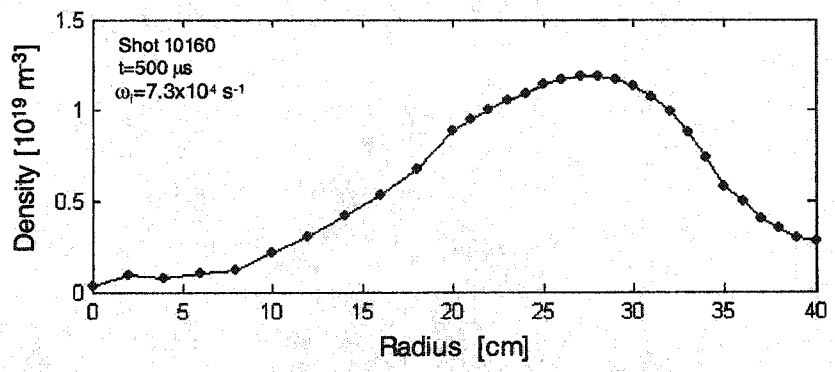

***Figure 8.8**: Density Profile for Shot 10160. Assumes uniform temperature.*

There could still be several reasons why viscous drag to the wall can explain the observed rotation. The edge plasma could have a very high impurity content of carbon, oxygen, and silicon, which would have a higher viscosity similar to the dashed lines in Fig. 8.7. Second, the assumption of axial and azimuthal symmetry could be invalid. The local edge plasma density could be much higher at the ends of the FRC or directly underneath each axial field coil. In both of these locations, there is no inward radial force due to the RMF as described in Sec. 7.1. Third, the edge velocity gradient could be much shorter than 2.5 cm, as the viscous torque scales as $1/\delta r$. There is no information about the ion rotational velocity beyond the last ICCD viewing chord at 35

cm. Finally, the density solution assumed a uniform temperature profile. If the edge plasma is cold, the edge density could be higher.

Evidence of viscous drag to the wall is seen in Fig. 8.9, a plot of B_z contours measured by the internal magnetic probe. The plasma is assumed to be time invariant, allowing the time history of the magnetic field measured at one azimuthal location to be mapped out spatially. Of course, any time variation in the plasma during this 105 μs interval will be mistaken as a spatial variation, which is probably the explanation for the high-mode structure at the center of the FRC. The plasma clearly exhibits an n=2 distortion, and one can see what looks like viscous boundary layer flow at the edge of the FRC. This figure also reveals how, in the presence of a distortion, the local separatrix radius can be much closer to the wall than the average excluded flux radius obtained from the excluded flux loops.

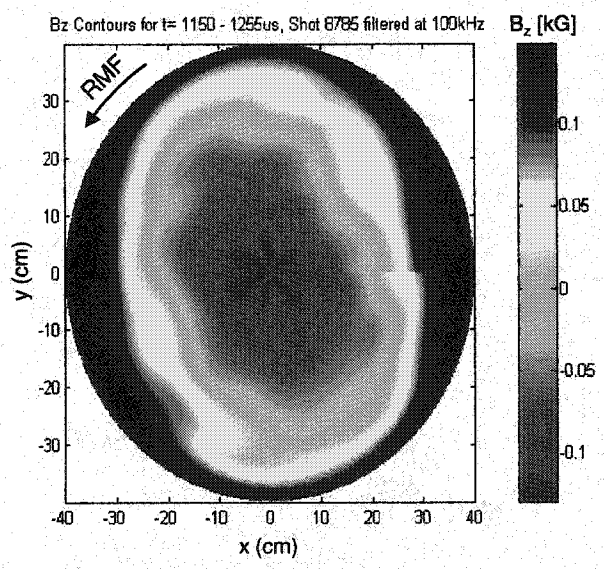

Figure 8.9: *Spatially-mapped B_z Contours. B_z data from internal magnetic probe fixed at one azimuthal location. The time history of B_z has been converted into a spatial plot.*

The dependence of the viscous torque with the ion rotation can be estimated using a simple model of the centrifugal pressure. As the plasma rotates, centrifugal pressure will cause the plasma pressure to be slightly higher on the outer portion of a

flux line than on the inner portion; that is, pressure is no longer a flux quantity. The magnitude of this pressure difference can be estimated by considering a simple rotating fluid with uniform temperature. The inviscid Euler equation for the fluid is

$$k_b T_t \frac{\partial n}{\partial r} - m_i \omega_i^2 n r = 0 . \tag{8.22}$$

This can be immediately integrated to obtain the solution

$$n(r) = n_0 \exp\left(r/\Delta\right)^2 ; \quad \Delta \equiv \sqrt{\frac{2k_b T_t}{m_i \omega_i^2}} \tag{8.23}$$

where n_0 is the density at the geometric axis. For viscosity, we are interested in how ion rotation raises the density at the edge of the FRC. The separatrix density is higher than n_0 by a factor

$$\frac{n(r_s)}{n_0} = \exp\left(\frac{m_i \omega_i^2 r_s^2}{2k_b T_t}\right). \tag{8.24}$$

The viscous torque was shown in Sec 8.2 to be

$$T_{visc}^{'} = 2\pi\mu\omega_i r_w^2 \left(r_w/\delta r\right). \tag{8.25}$$

In the magnetized limit, the viscosity coefficient is governed by the ion gyroradius and scales as $\mu \propto n_{edge}^2 T_i^{-1/2}$. Using the scaling for the edge density given in Eq. (8.24), the viscous torque will scale with ion rotation as

$$T_{visc}^{'} \propto \omega_i T_i^{-1/2} \exp\left(\frac{m_i \omega_i^2 r_s^2}{T_t}\right). \tag{8.26}$$

This scaling implies a very strong dependence of the viscous torque with the ion rotation frequency, particularly at low temperature. This type of viscous scaling would explain why the ion rotation seems to reach a constant value of $\omega_i \approx 7\times10^4$ s^{-1} late in the discharge, regardless of the applied torque. Neutral temperature measurements shown in Sec. 6.2 indicate that the ion temperature may be cold at late times, also leading to a strong increase of the viscous torque with ion rotation frequency. An increase in the applied torque would lead to a small increase in the ion rotation frequency. Since the plasma is cold, the centrifugal pressure is a significant fraction of the plasma pressure,

and the plasma is pushed out closer to the wall. The ion rotation frequency is also approximately equal to the ion diamagnetic drift frequency (see Fig. 6.31) and this small increase in rotation leads to a growth of the n=2 instability, further putting plasma on the wall. Since ion viscosity increases as the square of the edge density, a slight increase in rotation could lead to a large increase in the viscous torque. On the other hand, early in the discharge the ion temperature may be much higher, as T_t is higher and the fraction $T_i/T_e \approx 1$, as indicated by the neutral Dα temperature. This would lead to a lower viscous torque and a higher possible ion rotation frequency, as observed in Figs. 6.16 and 6.29.

In conclusion, if the plasma is modeled as axisymmetric, axially uniform, and composed of pure deuterium, then measurements made at the axial midplane indicate that the applied torque cannot be balanced by neutral drag alone. With these assumptions and simples estimates of the edge parameters, viscous torque to the wall cannot account for the remainder of the torque either. Of course, with the addition of impurities and three-dimensional effects, either of these braking mechanisms could be significantly altered. Without more detailed radial and axial profile measurements as well as knowledge of the impurity concentration, no more can be concluded at this point. An additional braking mechanism, end-shorting of the radial electric field, will be discussed in Sec. 9.2.

Chapter Nine

Additional Analysis

This chapter addresses two remaining issues concerning ion spin-up. First is the concern that the RMF may drive the ions directly as the ratio ω_{ci}/ω is raised to a value approaching unity. Clearly, in the limit where $\omega_{ci} \ll \omega$, the ions are not magnetized in the RMF field and cannot respond quickly enough to the rotating field to experience any $\langle v_z B_\theta \rangle$ Lorentz force. However, as B_ω is raised and the RMF frequency ω is lowered, this condition is no longer satisfied. For instance, TCS has reached values of ω_{ci}/ω as high as 0.75, yet is still able to maintain current drive. The approach taken here is to solve the two-fluid equations in a given RMF field. Inclusion of the RMF Lorentz force directly on the ions makes the equations highly coupled, and the equations are solved numerically. The resulting electron and ion fluid motions are shown for various values of ω_{ci}/ω and neutral drag.

The second issue addressed is the effect of end-shorting of the radial electric field on the plasma rotation. The ion diamagnetic rotation typically observed in conventional FRTP-formed FRCs has often been attributed to end-shorting. Axial field-line solutions indicate that end-shorting most likely occurs in TCS, although the open-field line plasma at the axial midplane is probably not line-tied to the ends of the device due to the transverse RMF. With the present diagnostics it is impossible to make any estimate of the drag torque that could result from end-shorting.

9.1 RMF Force Directly on the Ions

All the previous analyses have assumed that the rotating magnetic field does not exert an azimuthal force directly on the ions. As shown in Sec. 3.2, in the limit $\omega_{ci} \ll \omega$, where ω_{ci} is the ion cyclotron frequency in the RMF vacuum field B_ω, the ion

axial oscillation is purely inductive (90 degrees out of phase) with the radial magnetic field:

$$\tilde{\mathrm{v}}_{iz} = -ir\frac{e\tilde{B}_r}{m_i}. \tag{9.1}$$

The average azimuthal Lorentz force $\left\langle \tilde{\mathrm{v}}_{iz}\tilde{B}_r \right\rangle$ on the ions due to the RMF is then zero. The limit $\omega_{ci} \ll \omega$ is too restrictive, however. In TCS, at the lowest RMF frequency $\omega = 0.52\times10^6\ s^{-1}$ and highest field B_ω = 80 G, the ratio ω_{ci}/ω is as high as 0.75, yet the RMF is still able to drive a steady current. Clearly, a more accurate limit is needed on the RMF strength and frequency. This section reexamines the two-fluid equations and compares the azimuthal Lorentz force on the ions with the electron-ion resistive force. A less restrictive condition for ω and B_ω is found.

The analysis begins with the two-fluid momentum equations

$$\begin{aligned} n_e m_e \frac{D\mathbf{v}_e}{Dt} &= -n_e e\left(\boldsymbol{E} + \mathbf{v}_e \times \boldsymbol{B}\right) - \nabla P_e - n_e m_e \upsilon_{ei}\left(\mathbf{v}_e - \mathbf{v}_i\right) - n_e m_e \upsilon_{en}\mathbf{v}_e - m_e s\mathbf{v}_e \\ n_i m_i \frac{D\mathbf{v}_i}{Dt} &= n_i e\left(\boldsymbol{E} + \mathbf{v}_i \times \boldsymbol{B}\right) - \nabla P_i + n_i m_e \upsilon_{ei}\left(\mathbf{v}_e - \mathbf{v}_i\right) - n_i m_i \upsilon_{in}\mathbf{v}_i - m_i s\mathbf{v}_i \end{aligned} \tag{9.2}$$

where ν_{ei} is the electron-ion collision frequency, ν_{in} is the ion-neutral collision frequency, and s the electron (and ion) source rate due to ionization. It is assumed that the neutral particles involved in the momentum transfer and fueling have no directed velocities. The collision frequencies are taken to be constants independent of the directed electron and ion velocities.

This simple analysis does not take into account the three-dimensional equilibrium constraints of an FRC in a flux conserver. Instead, the magnetic field will be specified as

$$\vec{B} = B_r \cos\left(\omega t - \theta\right)\hat{r} + B_\theta \sin\left(\omega t - \theta\right)\hat{\theta} + B_z\hat{z}. \tag{9.3}$$

Using Faraday's law, the electric field is

$$\boldsymbol{E} = E_r(r)\hat{r} + r\omega\tilde{B}_\omega\hat{z}\,. \tag{9.4}$$

The model will also restrict all oscillating quantities to simple first-order oscillations. Neglecting all higher order harmonics, the ion and electron velocities in such a field then have steady radial and azimuthal components and an oscillating axial component:

$$\mathrm{v} = \mathrm{v}_r(r)\hat{r} + \mathrm{v}_\theta(r)\hat{\theta} + \tilde{\mathrm{V}}_z(r)\hat{z}\,. \tag{9.5}$$

The radial flow cannot be solved without taking into account three-dimensional equilibrium constraints. For this analysis, radial flow will be neglected. The plasma is assumed to be infinitely long and axially uniform. The ion and electron pressures are assumed to be axisymmetric. In summary, this model is restricted to a specified magnetic field, simple sinusoidal oscillations, and negligible radial flow, with no axial derivatives and axisymmetric pressure. The model is thus applicable only to the outermost edge of the FRC, where the $\langle\tilde{\mathrm{v}}_z\tilde{B}_r\rangle$ Lorentz force is larger than the $\mathrm{v}_r B_z$ force and the rotating magnetic field is not overly perturbed from the vacuum solution.

By neglecting radial flow, the system of equation has been reduced to just the axial and azimuthal equations, independent of the axial magnetic field. To simplify the notation, define $\upsilon_{ie} \equiv (m_e/m_i)\upsilon_{ei}$, $\upsilon_e{}^* \equiv \upsilon_{en} + s/n_e$, and $\upsilon_i{}^* \equiv \upsilon_{in} + s/n_i$. The electron and ion azimuthal equations are steady while the electron and ion axial equations describe sinusoidal oscillators:

$$\begin{aligned}
e\hat{\theta}:&\quad 0 = -(e/m_e)\langle\tilde{\mathrm{v}}_{ez}\tilde{B}_r\rangle - \upsilon_{ei}(\mathrm{v}_{e\theta} - \mathrm{v}_{i\theta}) - \upsilon_e{}^*\mathrm{v}_{e\theta}\\
i\hat{\theta}:&\quad 0 = (e/m_i)\langle\tilde{\mathrm{v}}_{iz}\tilde{B}_r\rangle + \upsilon_{ie}(\mathrm{v}_{e\theta} - \mathrm{v}_{i\theta}) - \upsilon_i{}^*\mathrm{v}_{i\theta}\\
e\hat{z}:&\quad i(\omega - \mathrm{v}_{e\theta}/r)\tilde{\mathrm{v}}_{ez} = -(e/m_e)(r\omega\tilde{B}_r - \mathrm{v}_{e\theta}\tilde{B}_r) - \upsilon_{ei}(\tilde{\mathrm{v}}_{ez} - \tilde{\mathrm{v}}_{iz}) - \upsilon_e{}^*\tilde{\mathrm{v}}_{ez}\\
i\hat{z}:&\quad i(\omega - \mathrm{v}_{i\theta}/r)\tilde{\mathrm{v}}_{iz} = (e/m_i)(r\omega\tilde{B}_r - \mathrm{v}_{i\theta}\tilde{B}_r) + \upsilon_{ie}(\tilde{\mathrm{v}}_{ez} - \tilde{\mathrm{v}}_{iz}) - \upsilon_i{}^*\tilde{\mathrm{v}}_{iz}
\end{aligned} \tag{9.6}$$

The azimuthal Lorentz force $\langle\tilde{\mathrm{V}}_z\tilde{B}_r\rangle$ is evaluated as

$$\langle\tilde{\mathrm{v}}_z\tilde{B}_r\rangle = \frac{|\mathrm{v}_z||B_r|}{2}\cos(\phi_{\mathrm{v}_z} - \phi_{B_r})\,. \tag{9.7}$$

Since B_r is pure real ($\phi_{B_r} = 0$), Eq. (9.7) simplifies to $\left\langle \tilde{v}_z \tilde{B}_r \right\rangle = (B_r/2)\mathrm{Re}(V_z)$. The equations can be simplified further by defining a cyclotron frequency in the radial magnetic field $\omega_{ce} \equiv (eB_r/m_e)$; $\omega_{ci} \equiv (eB_r/m_i)$ and a slip frequency as the difference between the rotation frequency and the RMF frequency: $\varpi_e \equiv \omega - \omega_e$; $\varpi_i \equiv \omega - \omega_i$. The set of equations can now be expressed as

$$\begin{aligned}
e\hat{\theta}: &\quad 0 = \omega_{ce}\,\mathrm{Re}(\mathsf{v}_{ez})/2 - \upsilon_{ei}(\mathsf{v}_{e\theta} - \mathsf{v}_{i\theta}) - \upsilon_e * \mathsf{v}_{e\theta} \\
i\hat{\theta}: &\quad 0 = \omega_{ci}\,\mathrm{Re}(\mathsf{v}_{iz})/2 + \upsilon_{ie}(\mathsf{v}_{e\theta} - \mathsf{v}_{i\theta}) - \upsilon_i * \mathsf{v}_{i\theta} \\
e\hat{z}: &\quad i\varpi_e \tilde{\mathsf{v}}_{ez} = -\omega_{ce} r\varpi_e - \upsilon_{ei}(\tilde{\mathsf{v}}_{ez} - \tilde{\mathsf{v}}_{iz}) - \upsilon_e * \tilde{\mathsf{v}}_{ez} \\
i\hat{z}: &\quad i\varpi_i \tilde{\mathsf{v}}_{iz} = \omega_{ci} r\varpi_i + \upsilon_{ie}(\tilde{\mathsf{v}}_{ez} - \tilde{\mathsf{v}}_{iz}) - \upsilon_i * \tilde{\mathsf{v}}_{iz}
\end{aligned} \tag{9.8}$$

Of the three terms on the right-hand side of each equation, the first is the total Lorentz force, the second is the electron-ion friction, and the third term is the neutral drag.

Before proceeding with a numerical solution to this set of equations, we can first attempt to find a simple analytic expression for the azimuthal RMF force applied directly to the ions. We are interested in the real part of the ion axial oscillation, since it is only this real part that will contribute to an average azimuthal Lorentz force. To decouple the ion axial equation from the electron axial equation, neglect the electron-ion friction term in the ion axial equation. The real part of the ion axial oscillation is then

$$\mathrm{Re}(\mathsf{v}_{iz}) \approx \frac{\omega_{ci} r\varpi_i \upsilon_i *}{(\upsilon_i *)^2 + \varpi_i^2}. \tag{9.9}$$

The azimuthal RMF force per unit mass directly on the ions is

$$F_{RMF}^{'} \approx \frac{1}{2}\frac{\omega_{ci}^2 r\varpi_i \upsilon_i *}{(\upsilon_i *)^2 + \varpi_i^2}. \tag{9.10}$$

The ion azimuthal equation can be decoupled from the electron azimuthal equation simply by assuming that the electrons are rotating synchronously with the RMF:

$\omega_e \approx \omega$. The ratio of the RMF azimuthal force on the ions to the resistive friction force $F_\eta = \upsilon_{ie}\left(\mathrm{v}_{e\theta} - \mathrm{v}_{i\theta}\right)$ is then found to be

$$\frac{F_{RMF}}{F_\eta} \approx \frac{1}{2}\left(\frac{\upsilon_i^*}{\upsilon_{ie}}\right)\left(\frac{\omega_{ci}^2}{\left(\upsilon_i^*\right)^2 + \varpi_i^2}\right). \tag{9.11}$$

As long as this ratio is small, then the RMF drive directly on the ions is negligible compared with electron-ion resistive friction. We conclude that there is no simple magnetization parameter $\omega_{ci}\tau$ for the ions in the RMF field. Eq. (9.11) is complicated despite considerable simplifications to decouple the electron and ion equations. For example, consider the interaction between ions and neutrals. Neutral collisions are a drag term in the ion azimuthal equation, but neutral collisions also allow the ion axial motion to have a real component, which leads to an RMF azimuthal force on the ions. This is why the neutral collision frequency υ_i^* appears in Eq. (9.11), even though at first glance it might seem that the RMF and electron-ion friction forces would be independent of the neutrals.

Eq. (9.8) can be solved numerically, of course. Divide all equations by the RMF frequency ω and denote normalized quantities with a prime, i.e. $\omega_{ce}' \equiv \omega_{ce}/\omega$. Dividing the axial equations by r, the set of equations can now be expressed in matrix form

$$\begin{bmatrix} \left(\upsilon_{ei}' + \upsilon_{en}'\right) & -\upsilon_{ei}' \\ -\upsilon_{ie}' & \left(\upsilon_{ie}' + \upsilon_{in}'\right) \end{bmatrix}\begin{bmatrix} \varpi_e' \\ \varpi_i' \end{bmatrix} = \begin{bmatrix} \left(\omega_{ce}'/2\right)\mathrm{Re}\left(\mathrm{V}_{ez}'/r\right) + \upsilon_{en}' \\ -\left(\omega_{ci}'/2\right)\mathrm{Re}\left(\mathrm{V}_{iz}'/r\right) + \upsilon_{in}' \end{bmatrix}$$

$$\begin{bmatrix} \left(i\varpi_e' + \upsilon_{ei}' + \upsilon_{en}'\right) & -\upsilon_{ei}' \\ -\upsilon_{ei}' & \left(i\varpi_i' + \upsilon_{ie}' + \upsilon_{in}'\right) \end{bmatrix}\begin{bmatrix} \mathrm{V}_{ez}'/r \\ \mathrm{V}_{iz}'/r \end{bmatrix} = \begin{bmatrix} -\omega_{ce}'\varpi_e' \\ \omega_{ci}'\varpi_i' \end{bmatrix} \tag{9.12}$$

This is a set of coupled non-linear equations. The equations are solved numerically in MATLAB using a nonlinear least-squares minimization solver. From the MATLAB documentation: "This algorithm is a subspace trust region method and is based on the

interior-reflective Newton method[51]. Each iteration involves the approximate solution of a large linear system using the method of preconditioned conjugate gradients (PCG)."

The system of equations given in (9.12) is solved for typical TCS parameters: $\gamma = (\omega_{ce}/\upsilon_{ei}) = 18$, $(\upsilon_i^*/\upsilon_{ie}) = 4$, and $(\upsilon_e^*/\upsilon_{ei}) \approx 0$. The electron-neutral collision frequency υ_e^* is negligible if we assume that electron-impact ionization is the dominant collision process. If the ionization and charge-exchange rate coefficients are roughly equal, then the electron-neutral collision frequency will be half the total ion-neutral collision frequency: $\upsilon_e^* \approx 0.5\upsilon_i^*$. Since $\upsilon_{ei} = (m_i/m_e)\upsilon_{ie} = 3672 \cdot \upsilon_{ie}$, the ratio of electron-neutral friction to electron-ion friction is negligible: $(\upsilon_e^*/\upsilon_{ei}) = 5\times10^{-4}$.

Various quantities computed using these parameters are shown in Fig. 9.1 as a function of $(\omega_{ci}/\omega) \propto (B_r/\omega)$. In Fig. 9.1(a), the normalized electron (blue) and ion (red) rotation frequencies are shown, as well as the net diamagnetic frequency $(\omega_e - \omega_i)/\omega$ in black. Both the electrons and the ions rotate in the same direction as the RMF. The electrons are nearly synchronous at all values of (ω_{ci}/ω), while the ions rotate at 20% of ω up to $(\omega_{ci}/\omega) = 0.5$, beyond which they ions are driven directly by the RMF. The current-drive is effectively negated by $(\omega_{ci}/\omega) = 0.75$ as the ions are nearly synchronous with the RMF. In Fig. 9.1(b), the normalized axial velocities for the electrons and ions are shown. The magnitude of the ion and electron axial oscillations are nearly equal, a somewhat counter-intuitive result. Despite its small mass, the electron's axial oscillation in the applied E_z field is limited by the $v_\theta \times B_r$ Lorentz force. This Hall term is what allows the RMF to penetrate much further than the simple resistive skin depth. The phases of the electron and ion axial oscillation relative to B_r are shown in Fig. 9.1(c). At very low values of (ω_{ci}/ω), we see the

expected result that the electrons are resistive (180°) and the ions are inductive (90°) relative to B_r. As (ω_{ci}/ω) is raised, the ions remain inductive but the electrons quickly become predominantly inductive as well. This surprising result can be explained as follows. In this computation, the ratio $(\omega_{ce}/\upsilon_{ei})=18$ is held fixed. As (ω_{ci}/ω) is increased, the ratio (υ_{ei}/ω) increases as well. Electron-ion friction begins to dominate the electron axial equation, and the electrons essentially follow the ions, with the remaining phase difference sufficient to drive the electron azimuthal velocity. In Fig. 9.1(d), the ratio of the oscillating axial current to the steady azimuthal current is shown. The ratio remains small until $(\omega_{ci}/\omega)\approx 0.7$, beyond which the azimuthal current decreases rapidly as the axial current remains about the same. Finally, Fig 9.1(e) shows the importance of the RMF $\langle \tilde{v}_{iz}\tilde{B}_r \rangle$ drive term to the resistive term in the ion azimuthal equation. As long as this ratio is below one, the RMF is not driving the ions directly. For these plasma parameters, a critical value of about $(\omega_{ci}/\omega)_{crit}\approx 0.5$ is found. Of course, it must be remembered that in this computation ω_{ci} is defined as the cyclotron frequency in the actual radial field B_r, not the vacuum value B_ω. In the partially-penetrated case, the edge value of B_r is perhaps 20% of the vacuum B_ω. The quoted value for TCS of $(\omega_{ci}/\omega)_{max}\approx 0.75$ was calculated using B_ω; the corresponding value for this calculation would be $(\omega_{ci}/\omega)_{max}\approx 0.15$.

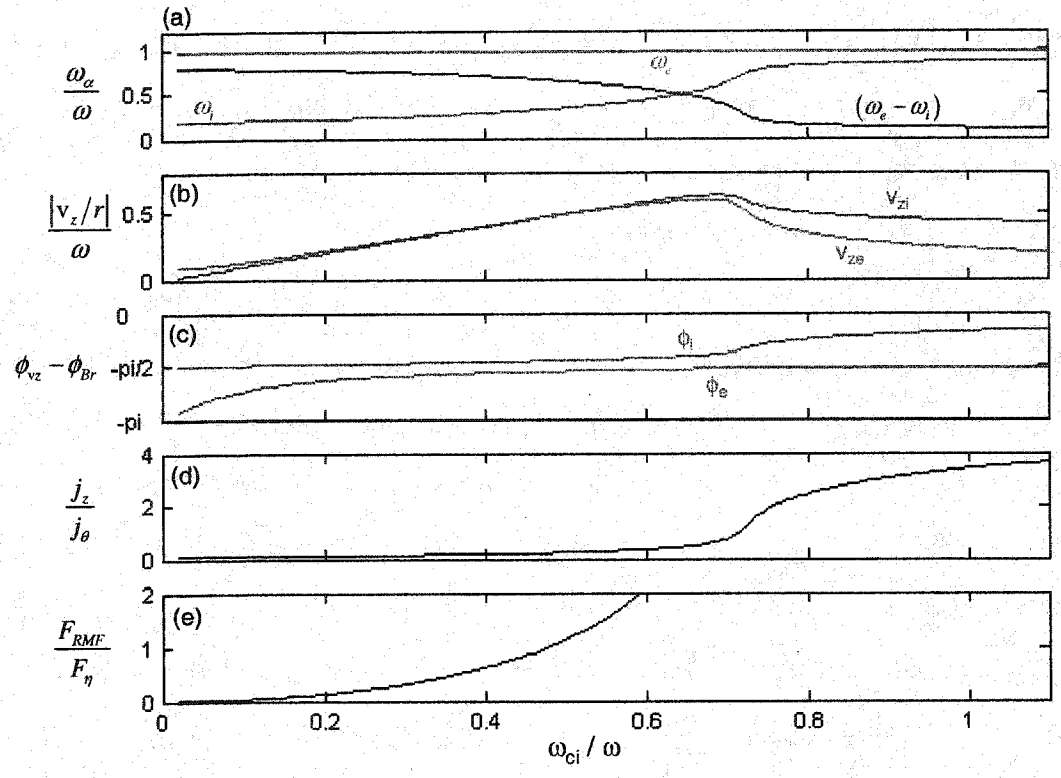

Figure 9.1: *Numerical Two-fluid Solutions.* $\gamma = (\omega_{ce}/\upsilon_{ei}) = 18$, $(\upsilon_i{}^*/\upsilon_{ie}) = 4$, *and* $(\upsilon_e{}^*/\upsilon_{ei}) = 0$. *Blue lines: electrons. Red lines: ions. (a) Normalized rotation frequency. The net diamagnetic frequency is shown as a black line. (b) Normalized axial oscillation magnitude. (c) Phase of the axial oscillation relative to the radial field. (d) Amplitude of the oscillating axial current relative to the steady azimuthal current. (e) Amplitude of the azimuthal force directly on the ions relative to resistive electron-ion friction.*

An important parameter for ion rotation is $(\upsilon_i{}^*/\upsilon_{ie})$. The two-fluid equations have been solved for various values of this parameter, and the results are shown in Fig. 9.2. At low values of (ω_{ci}/ω), the ion rotation in this model is well-characterized by the expression

$$\frac{\omega_i}{\omega} \approx \left(1 + \frac{\upsilon_i{}^*}{\upsilon_{ie}}\right)^{-1}. \qquad (9.13)$$

At low values of $(\upsilon_i{}^*/\upsilon_{ie})$, the azimuthal current drive decreases rapidly when (ω_{ci}/ω) exceeds a value of about 0.5 as the ions are driven directly by the RMF. At higher values of ion-neutral friction, the penalty is not so stiff, and current drive can be maintained even when $\omega_{ci} > \omega$.

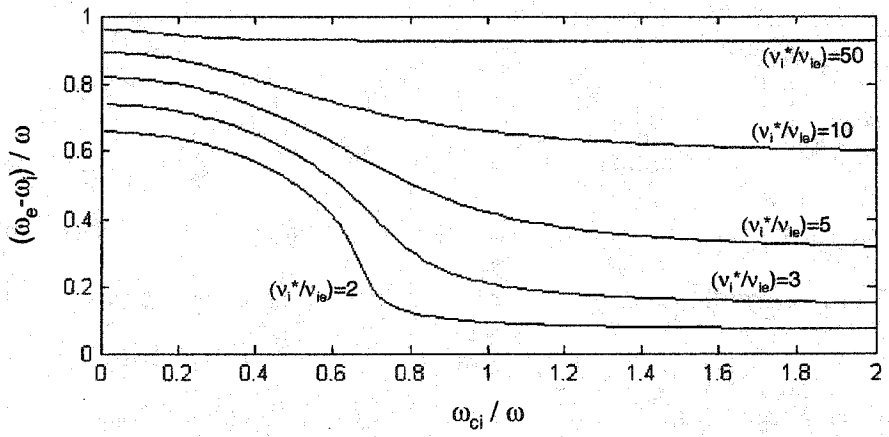

***Figure 9.2**: Effect of Ion-neutral Friction on Azimuthal Current Drive*

9.2 Radial Electric Field

Up this point in the analysis, the radial electric field has been left as an unspecified parameter, free to adjust to the value required by a given ion rotation velocity and pressure gradient. In this section, the effect of a boundary condition imposed on the radial electric field is considered. First, the governing equation for the relationship between the ion azimuthal velocity and the radial electric field is derived from the radial component of the ion fluid equation. Second, a shorted boundary condition is applied to the radial electric field at the ends of the vacuum chamber. The resulting radial electric field at the axial midplane of the FRC is then found by solving the axial electron equation, following the work by Steinhauer[24]. Finally, the implications of end-shorting are qualitatively discussed.

Neglecting resistivity and neutral friction, the ion fluid momentum equation is

$$mn\left[\frac{\partial \mathbf{v}}{\partial t}+(\mathbf{v}\cdot\nabla)\mathbf{v}\right]=nq(\boldsymbol{E}+\mathbf{v}\times\boldsymbol{B})-\nabla p. \tag{9.14}$$

In steady-state, Faraday's law dictates that the electric field is the gradient of a scalar potential: $E=-\nabla\phi$. Assume that there is no radial flow and neglect centripetal acceleration; the convective derivative on the left-hand side of the equation is then zero. Assuming axisymmetric pressure, the radial component of Eq. (9.14) can be written as

$$\mathsf{v}_\theta=\frac{1}{B_z}\frac{\partial\phi}{\partial r}-\frac{\left\langle\tilde{\mathsf{v}}_z\tilde{B}_\theta\right\rangle}{B_z^2}+\frac{1}{neB_z}\frac{dp_i}{dr}. \tag{9.15}$$

The first term on the right-hand side is the electric drift $\mathsf{v}_E\equiv(\partial\phi/\partial r)/B_z$, and the last term is the diamagnetic drift $\mathsf{v}_d\equiv(dp_i/dr)/(neB_z)$. The middle term is something new to FRCs; it is similar to a $g\times B$ gravity drift and is caused by the interaction between the radial RMF force and the axial magnetic field. This term may be significant because the ion axial velocity and the azimuthal magnetic field are nearly in-phase. The $\left\langle\tilde{\mathsf{v}}_z\tilde{B}_\theta\right\rangle$ force is inwards, so this "RMF drift" is in the ion paramagnetic direction.

Up to this point, the radial electric field has been assumed to be free to adjust. With the observed ion paramagnetic rotation, this implies a strong inward electric field. We now ask the question: what happens if a boundary condition is applied to the electric field? Particularly, what if the radial electric field is shorted at the ends of the vacuum chamber? This boundary condition may be applicable in TCS, where conducting Tantalum inserts line the conical ends of the sustainment chamber. The adjoining acceleration section on the upstream end is made of non-conducting quartz, while the plug section on the downstream end is made of conducting stainless steel. Lines of constant flux are shown in Fig. 9.3 for two shots with very different boundary conditions. The flux lines are generated from an axial array of flux loops. The excluded flux radius of the FRC is fit to an ellipse, the flux at the geometric axis is set to zero, and the lines of constant flux are obtained by solving for the magnetic vector

potential. In Fig. 9.3(a), the open field lines are clearly intersecting the conducting cones since the cone coil was not fired. At this conducting boundary, the radial electric field between these field lines is shorted. In Fig. 9.3(b), the cone coil has been fired, preventing the external field from intersecting the cones. Nevertheless, the field lines still intersect the stainless steel plug section on the downstream end of the sustainment chamber, where they will be shorted as well.

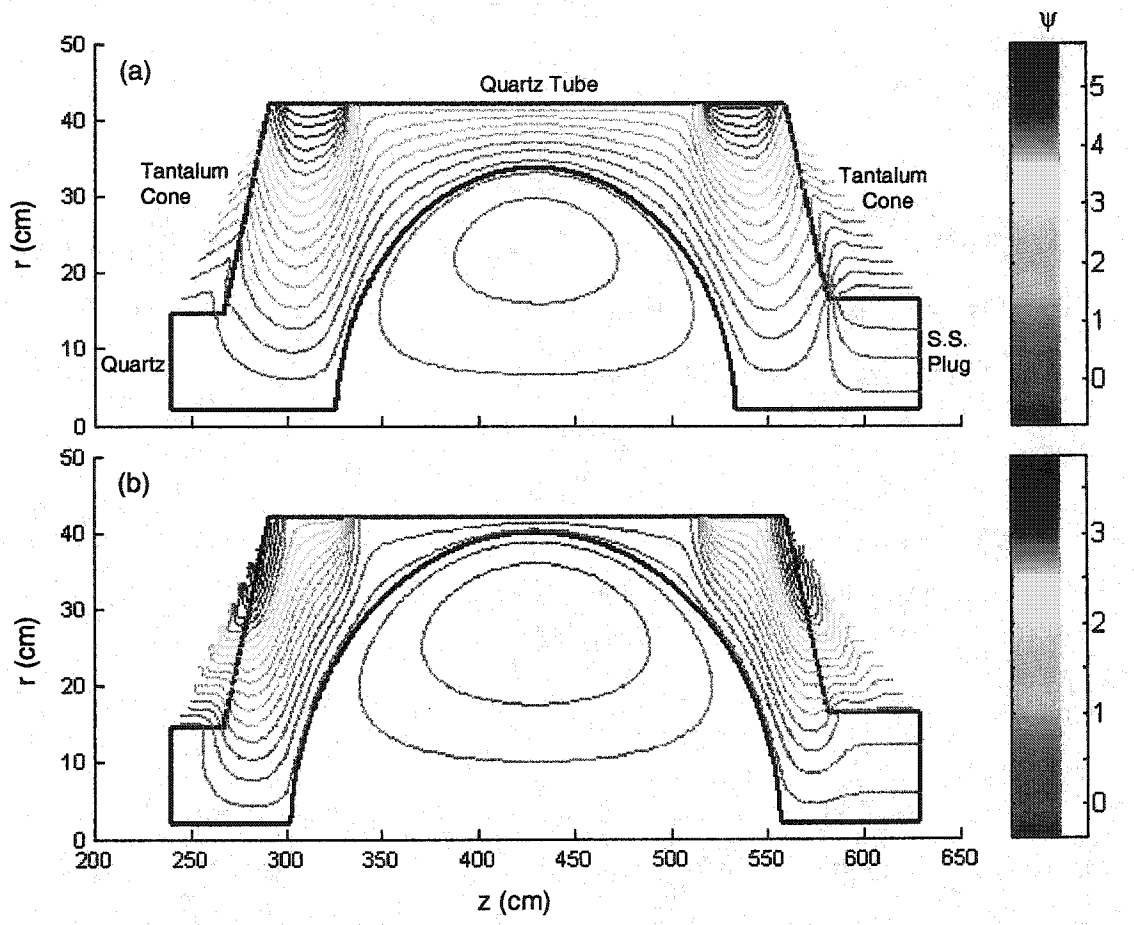

***Figure 9.3**: External Field Lines. (a) Cone coil not fired (shot 7368 t=800 μs). (b) Cone coil fired at 350 V (shot 7884 t=800 μs).*

Just because the radial electric field is shorted at the boundary does not necessarily imply that the radial electric field is zero at the axial midplane. The electric field along an open field line can be found from the electron axial equation of motion:

$$0 = en_e \frac{\partial \phi}{\partial z} - \frac{\partial p_e}{\partial z} \tag{9.16}$$

where we have assumed massless electrons, neglected resistivity, and ignored any Lorentz forces due to the RMF. Parallel electron thermal conduction is sufficiently high that we can assume uniform electron temperature along the field line. The electron equation is then

$$0 = en_e \frac{\partial \phi}{\partial z} - k_b T_e \frac{\partial n_e}{\partial z}. \tag{9.17}$$

The solution to this differential equation is the Boltzmann relation

$$\phi(z) = \left(\frac{k_b T_e}{e} \right) \ln n_e(z) + \phi_0 \tag{9.18}$$

where ϕ_0 is the potential at the boundary. If the boundary potential is uniform $(\partial \phi_0 / \partial r = 0)$, as is the case at a conducting boundary, then the radial electric field is found by differentiating Eq. (9.18) with respect to r:

$$E_r = -\frac{\partial \phi}{\partial r} = -\frac{k_b T_e}{en_e} \frac{\partial n_e}{\partial r}. \tag{9.19}$$

The density gradient is negative (inward) on the open field lines, so the radial electric field is positive (points outward). The resulting electric drift on the open field lines at the axial midplane is

$$\mathsf{v}_E = \frac{k_b T_e}{en_e B_z} \frac{\partial n_e}{\partial r}. \tag{9.20}$$

The electric drift is in the ion diamagnetic direction and has the same form as the diamagnetic drift, except that it depends on electron temperature. Assuming quasineutrality and uniform total temperature $T_t \equiv T_i + T_e$, we can define a total drift velocity on the open field lines

$$\mathsf{v}_{tot} \equiv \mathsf{v}_E + \mathsf{v}_d = \frac{k_b T_{tot}}{enB_z} \frac{\partial n}{\partial r}. \tag{9.21}$$

With the open-field plasma rotating in the ion diamagnetic direction, and the closed-field plasma rotating in the paramagnetic direction, a large velocity shear will develop.

The viscous torque analysis presented in Sec. 8.2 is still valid, but the viscous momentum transfer will be to the open field plasma rather than to the wall.

The presence of the RMF may make this open-field solution to the electron equation incorrect. The electrons no longer see the time-averaged axial field lines shown in Fig. 9.3; rather, they see the instantaneous total field, including the radial component of the RMF, which may strike the quartz wall first. In this case, the open-field plasma at the midplane is not line-tied to the ends of the machine. Nevertheless, end-shorting could still put a significant torque on the ends of the plasma. In steady-state, the FRC must extend beyond the ends of the RMF antenna in order to maintain a steady radial flow pattern. The radial electric field at the ends of the FRC could still be shorted.

With the present diagnostics, it is impossible to quantify how much torque could be applied to the plasma due to end-shorting in TCS. The torque would be supplied by the conducting boundary and transmitted to the open-field plasma at the midplane via twisted axial field lines. The torque would then be transferred to the closed-field plasma through viscosity. Detailed three-dimensional measurements of the axial field profile at the ends of the device would be needed to calculate the torque using a Maxwell stress tensor. The twisting of the field should also be detectable as a small, steady toroidal component on the open field lines at the ends of the FRC.

TEN

Summary and Conclusions

Conventional FRCs formed by the Field-Reversed Theta-Pinch technique can be rapidly heated to high temperature, but then resistively decay away without some external means of sustaining the poloidal flux. The simple closed geometry of the FRC precludes inductive current drive as in Tokamaks. One promising current drive method studied in the TCS experiment is the use of a transverse Rotating Magnetic Field, or RMF. This has been shown in TCS to drive a steady electron current and maintain a low-density, low-temperature FRC in essentially steady-state. In driving the electron current through a $\langle v_z \times B_r \rangle$ Lorentz force, the RMF is putting a net torque on the plasma. This torque is eventually transferred to the ions through resistive collisions. Without a drag force, the ions will rapidly spin up in the paramagnetic direction and negate the current drive. With the anomalous resistivity in TCS, the ions should spin up on a ~20 μs timescale.

A multi-chord Intensified Charge-Coupled Device (ICCD) spectrometer has been installed on TCS to measure the ion rotation profile via the Doppler shift of impurity line radiation. The majority Deuterium species is fully ionized and so cannot be used for Doppler shift studies, but impurities of various mass and ionization state have all been found to be rotating synchronously. Furthermore, the impurity ion rotation frequency has been found to correspond to the n=2 rotational frequency, providing further evidence that the ICCD measurements truly reflect the bulk plasma rotation rate. The plasma is observed to rapidly spin up in the ion paramagnetic direction to a typical rigid rotation frequency $\omega_i \approx 7 \times 10^4$ s^{-1}, or less than 15% of the RMF frequency. Although this ion rotation rate is not fast enough to significantly degrade the current drive, it does lead to a rotational n=2 instability in the ion paramagnetic direction, opposite to conventional FRTP-formed FRCs. Because of this,

TCS has typically been operated with the FRC separatrix radius very near the quartz vacuum boundary to wall-stabilize the mode.

Neutral drag has been proposed as the primary ion drag mechanism in earlier Rotamak experiments. The neutral density and resulting charge-exchange and ionization rates have been calculated from an array of absolutely calibrated Dα emission detectors. The typical background neutral fraction in TCS is about 2% of the plasma density. The resulting charge-exchange and ionization rates have been verified with a global power balance model. The low ionization rate indicates a long particle confinement time of ~500 μs, while the energy confinement time is radiation-dominated and is under 100 μs.

The low neutral density obtained from the Dα emission cannot explain the relatively slow ion rotation observed in TCS. At most, neutral drag accounts for about half of the total applied torque, and in most cases accounts for only 25% of the torque. The most likely candidate to supply the remaining torque is viscous drag to the wall. Using classical ion-ion viscosity, the key parameters in determining the viscous drag are the edge plasma density, the edge ion temperature, and the edge velocity gradient. Unfortunately, none of these parameters are measured accurately in the present experiment. Using very simple estimates for these parameters, with pure deuterium, and assuming axial and azimuthal uniformity of the edge plasma, viscous drag on the wall is not sufficient to explain the observed ion rotation rate. However, errors in the edge measurements, nonuniformities, and the inclusion of impurities could raise the viscous drag significantly.

There are several additional lines of evidence that viscosity is significant. First, the plasma is observed to rotate as a rigid body, even though the electron rotation is not rigid and the resistivity may be anisotropic. Second, the plasma separatrix is only a few cm from the wall, and the development of even a small n=2 instability will put plasma

locally on the wall. The fact that the instability is wall stabilized with a non-conducting quartz wall implies that the wall is acting as a limiter. Finally, at low ion temperature, centrifugal pressure for these rotational velocities becomes a significant fraction of the total pressure, driving plasma density outwards to the wall.

An additional concern is that, as the RMF strength is raised and the RMF frequency is lowered, the ions may become magnetized in the RMF and may be driven directly. Numerical solutions to the two-fluid equations show that as long as (ω_{ci}/ω) remains less than about 0.5, the RMF drive directly on the ions is less than the electron-ion friction. The correct definition of ω_{ci} is shown to be the ion cyclotron frequency in the *radial* component of the RMF field, not the vacuum RMF field. Due to the screening of the RMF, the radial field can be 10% or less of the vacuum field. TCS operates with a *vacuum* (ω_{ci}/ω) as high as 0.75, but using the correct definition this ratio is lowered to about 0.08, and direct ion drive is negligible.

Although ion spin-up is not a problem in the present device, it may become significant in future experiments. If the viscous boundary is removed (by the addition of internal flux rings inside the vacuum chamber, for instance) and the background neutral density is further lowered (through Titanium gettering, for instance), then the ions may spin up to a much higher rotation frequency. Ion spin-up may scale unfavorably with ion temperature as well, as the classical ion viscosity coefficient decreases with temperature. This may have been observed in TCS, where the plasma rotates faster at the beginning of the discharge when the total temperature, and presumably the ion temperature, is hotter and the impurity concentrations are lower.

There are possible solutions to the problem of ion spin-up even if wall viscosity and neutral drag are diminished in future experiments. If the resistivity can be decreased, then the total applied torque that the RMF must supply to maintain the poloidal flux is decreased as well. As the separatrix radius is removed from the wall,

end-shorting of the radial electric field may become important. This mechanism has been invoked to explain the *diamagnetic* ion rotation observed in conventional FRCs. Finally, neutral beams can be injected in the ion diamagnetic direction. Not only would these beams directly supply an opposing torque, but they would also lower the drive requirement of the RMF.

End Notes

1. M. Tuszewski, *Nucl. Fusion* **28**, 2033 (1988)

2. J. L. Scharzmeier et al, *Phys. Fluids* **26**, 1295 (1983)

3. J. T. Slough and A. L. Hoffman, *Nucl. Fusion* **28**, 1121 (1988)

4. D. C. Barnes, J. L. Schwarzmeier, H. R. Lewis, and C. E. Seyler, *Phys. Fluids* **29**, 2616 (1986)

5. H. Yamada, T. Katano, A. Ishida, and L. C. Steinhauer, *Phys. Plasmas* **10**, 1168 (2003)

6. J. T. Slough, A. L. Hoffman, R. D. Milroy, R. Maqueda, and L. C. Steinhauer, *Phys. Plasmas* **2**, 2286 (1995)

7. A. L. Hoffman et al, *Fusion Tech.* **23**, 185 (1993)

8. T. Ishimura, *Phys. Fluids* 27, 2139 (1987)

9. A. L. Hoffman, J. T. Slough, and D. G. Harding, *Phys. Fluids* **26**, 1626 (1983)

10. W. N. Hugrass, *J. Plasma Phys.* **28**, 369 (1982)

11. I. R. Jones and W. N. Hugrass, *J. Plasma Phys.* **26**, 441 (1981)

12. A. L. Hoffman, *Nucl. Fusion* **40**, 1523 (2000)

13. R. D. Milroy, *Phys. Plasmas* **7**, 4135 (2000)

14. H. A. Blevin and P. C. Thonemann, *Nucl. Fusion Supplement* **Part 1**, 55 (1962)

15. W. N. Hugrass and I. R. Jones, *J. Plasma Phys.* **29**, 155 (1983)

16. W. N. Hugrass, *Aust. J. Phys.* **39**, 513 (1986)

17. P. M. Bellan, *Phys. Rev. Lett.* **62**, 2464 (1989)

18. M. Ohnishi and A. Ishida, *Nucl. Fusion* **36**, 232 (1996)

19. A. L. Hoffman, *Phys. Plasmas* **5**, 979 (1998)

20. R. A. Clemente, *J. Phys. Soc. Jpn.* **67**, 3450 (1998)

21. R. D. Milroy, *Phys. Plasmas* **6**, 2771 (1999)

22. R. D. Milroy, *Phys. Plasmas* **8**, 2804 (2001)

23. L. C. Steinhauer, *Phys. Plasmas* **8**, 3367 (2001)

24. L. C. Steinhauer, *Phys. Plasmas* **9** (2002)

25. I. R. Jones, *Phys. Plasmas* **6**, 1950 (1999)

26. H. R. Zwi, A. Kuthi, A. Y. Wong, and B. Wells, *Phys. Fluids B* **3**, 126 (1991)

27. J. T. Slough and K. E. Miller, *Phys. Plasmas* **7**, 1945 (2000)

28. A. L. Hoffman et al, *Nucl. Fusion* **41**, 92 (2002)

29. A. L. Hoffman, P. Gurevich, J. Grossnickle, and J. T. Slough, *Nucl. Fusion* **39** (1999)

30. J. A. Grossnickle, Ph.D. thesis, University of Washington (2001)

31. S. J. Tobin et al, *Rev. Sci. Instrum.* **72**, 3528 (2001)

32. R. J. Maqueda, G. A. Wurden, and E. A. Crawford, *Rev. Sci. Instrum.* **63**, 4717 (1992)

33. G. R. Votroubek, private communication

34. A. M. Peter, Master's thesis, University of Washington (2001)

35. C. Earle, *Laser Focus World* **35** (1999)

36. I. H. Hutchinson, Principles of Plasma Diagnostics. Cambridge: Cambridge University Press 2002.

37. W. H. Press et al, Numerical Recipes in C. Cambridge: Cambridge University Press 1995.

38. R. E. Bell, *Rev. Sci. Instrum.* **68**, 1273 (1997)

39. Z. A. Pietrzyk, private communication

40. A.L. Hoffman, H.Y. Guo, R.D. Milroy, and Z.A. Pietrzyk, to be published

41. L. C. Johnson and E. Hinnov, *J. Quant. Spectros. Radiat. Trans.* **13**, 333 (1973)

42. P. S. Krstic and D. R. Schultz, *Phys. Rev. A* **60**, 2118 (1999)

43. G. S. Voronov, *Atomic Data and Nuclear Tables* **65** (1997)

44. C. F. Barnett, Oak Ridge National Laboratory: ORNL-6086 (1990)

45. K. Sawada, K. Eriguchi, and T. Fujimoto, *J. Appl. Phys.* **72**, 8122 (1993)

46. H. Y. Guo, A. L. Hoffman, R. D. Brooks, A. M. Peter, Z. A. Pietrzyk, S. J. Tobin, and G. R. Votroubek, *Phys. Plasmas* **9**, 185 (2002)

47. R. D. Milroy, private communication

48. S. I. Braginskii, Reviews of Plasma Physics Vol. 1, New York: Consultants Bureau, 1965.

49. R. J. Kanzleiter, D. P. Stotler, C. F. F. Carney, and D. Steiner, *Phys. Plasmas* **7**, 5064 (2000)

50. J. B. Kingdon and G. J. Ferland, *ApJS* **106**, 205 (1996)

51. T.F. Coleman and Y. Li, *SIAM Journal on Optimization* **6**, 418 (1996)

Bibliography

Barnes, D. C., J. L. Schwarzmeier, H. R. Lewis, and C. E. Seyler, *Phys. Fluids* **29**, 2616 (1986)

Barnett, C. F. Oak Ridge National Laboratory: ORNL-6086 (1990)

Bell, R. E. *Rev. Sci. Instrum.* **68**, 1273 (1997)

Bellan, P. M. *Phys. Rev. Lett.* **62**, 2464 (1989)

Blevin H. A. and P. C. Thonemann, *Nucl. Fusion* Supplement Part 1, 55 (1962)

Braginskii, S. I. Reviews of Plasma Physics Vol. 1, New York: Consultants Bureau, 1965.

Clemente, R. A. *J. Phys. Soc. Jpn.* **67**, 3450 (1998)

Coleman, T. F. and Y. Li, *SIAM Journal on Optimization* **6**, 418 (1996)

Earle, C. *Laser Focus World* **35** (1999)

Grossnickle, J. A. Ph.D. thesis, University of Washington (2001)

Guo, H. Y., A. L. Hoffman, R. D. Brooks, A. M. Peter, Z. A. Pietrzyk, S. J. Tobin, and G. R. Votroubek, *Phys. Plasmas* **9**, 185 (2002)

Hoffman, A. L., J. T. Slough, and D. G. Harding, *Phys. Fluids* **26**, 1626 (1983)

Hoffman, A. L. et al, *Fusion Tech.* **23**, 185 (1993)

Hoffman, A. L. *Phys. Plasmas* **5**, 979 (1998)

Hoffman, A. L., P. Gurevich, J. Grossnickle, and J. T. Slough, *Nucl. Fusion* **39** (1999)

Hoffman, A. L. *Nucl. Fusion* **40**, 1523 (2000)

Hoffman, A. L. et al, *Nucl. Fusion* **41**, 92 (2002)

Hoffman, A.L., H.Y. Guo, R.D. Milroy, and Z.A. Pietrzyk, to be published

Hugrass, W. N. *J. Plasma Phys.* **28**, 369 (1982)

Hugrass, W. N. and I. R. Jones, *J. Plasma Phys.* **29**, 155 (1983)

Hugrass, W. N. *Aust. J. Phys.* **39**, 513 (1986)

Hutchinson, I. H. Principles of Plasma Diagnostics. Cambridge: Cambridge University Press 2002.

Ishimura, T. *Phys. Fluids* 27, 2139 (1987)

Johnson, L. C. and E. Hinnov, *J. Quant. Spectros. Radiat. Trans.* **13**, 333 (1973)

Jones, I. R. and W. N. Hugrass, *J. Plasma Phys.* **26**, 441 (1981)

Jones, I. R. *Phys. Plasmas* **6**, 1950 (1999)

Kanzleiter, R. J., D. P. Stotler, C. F. F. Carney, and D. Steiner, *Phys. Plasmas* **7**, 5064 (2000)

Kingdon, J. B. and G. J. Ferland, *ApJS* **106**, 205 (1996)

Krstic, P. S. and D. R. Schultz, *Phys. Rev. A* **60**, 2118 (1999)

Maqueda, R. J., G. A. Wurden, and E. A. Crawford, *Rev. Sci. Instrum.* **63**, 4717 (1992)

Milroy, R. D. *Phys. Plasmas* **6**, 2771 (1999)

Milroy, R. D. *Phys. Plasmas* **7**, 4135 (2000)

Milroy, R. D. *Phys. Plasmas* **8**, 2804 (2001)

Milroy, R. D. private communication

Ohnishi, M. and A. Ishida, *Nucl. Fusion* **36**, 232 (1996)

Peter, A. M. Master's thesis, University of Washington (2001)

Pietrzyk, Z. A. private communication

Press, W. H. et al, Numerical Recipes in C. Cambridge: Cambridge University Press 1995.

Sawada, K., K. Eriguchi, and T. Fujimoto, *J. Appl. Phys.* **72**, 8122 (1993)

Scharzmeier, J. L. et al, *Phys. Fluids* **26**, 1295 (1983)

Slough, J. T. and A. L. Hoffman, *Nucl. Fusion* **28**, 1121 (1988)

Slough, J. T., A. L. Hoffman, R. D. Milroy, R. Maqueda, and L. C. Steinhauer, *Phys. Plasmas* **2**, 2286 (1995)

Slough, J. T. and K. E. Miller, *Phys. Plasmas* **7**, 1945 (2000)

Steinhauer, L. C. *Phys. Plasmas* **8**, 3367 (2001)

Steinhauer, L. C. *Phys. Plasmas* **9** (2002)

Tobin, S. J. et al, *Rev. Sci. Instrum.* **72**, 3528 (2001)

Tuszewski, M. *Nucl. Fusion* **28**, 2033 (1988)

Voronov, G. S. *Atomic Data and Nuclear Tables* **65** (1997)

Votroubek, G. R. private communication

Yamada, H., T. Katano, A. Ishida, and L. C. Steinhauer, *Phys. Plasmas* **10**, 1168 (2003)

Zwi, H. R., A. Kuthi, A. Y. Wong, and B. Wells, *Phys. Fluids B* **3**, 126 (1991)

Appendix A

Error Analysis

The emission profile $\varepsilon(r)$ is obtained by Abel inverting the total brightness profile B(y) and is independent of the deconvolution. Two sources of error are considered here. The first is systematic error in the calibration of the relative transmission of each fiber. The fibers were calibrated with a mercury or cadmium lamp placed inside an integrating sphere. A single collimating lens was placed at the exit of the integrating sphere, and the fibers were calibrated one at a time, each through the same lens. Systematic errors in the calibration could arise from variation of the lamp intensity with time, variations of the fiber placement in the lens holder, and variations in the lenses actually used on the experiment. Systematic errors have been estimated by calibrating the same fiber several times, with different fiber placements and lenses. The systematic error σ_S is estimated from the standard deviation in calibrated fiber transmission, found to be σ_S=2.3%. Statistical error σ_N is calculated assuming Poisson statistics for the collected photons. Although the ICCD spectrometer is not absolutely calibrated, the total system gain is estimated at 53 digital counts/photon from the average single photon signal. This is a reasonable gain, as the maximum gain is specified as 80 counts/photon and the intensifier is not run at the maximum voltage. The conversion factor β is then 0.019 photons/count. The statistical variation σ_N is proportional to the square root of the total number of photons collected:

$$\sigma_N = \sqrt{\beta N} \tag{A.1}$$

where N is the integrated number of digital counts in the spectrum. Statistical variation in the background bremsstrahlung emission and CCD dark charge are neglected. The error in the measured brightness B_i for chord is then

$$\sigma_{Bi}^2 = \sigma_S^2 + \sigma_{Ni}^2 . \tag{A.2}$$

The error in the inverted emission ε_j for shell j is found from the matrix inversion formula given in Eq. (5.13):

$$\sigma_{\varepsilon j}^2 = \sum_i \left(L_{ji}^{-1} \sigma_{Bi} \right)^2 . \tag{A.3}$$

The matrix-inversion formula for the local velocity v_j is

$$v_j = \frac{\sum_i M_{ji}^{-1} B_i u_i}{\sum_i L_{ji}^{-1} B_i} = \frac{\sum_i M_{ji}^{-1} B_i u_i}{\varepsilon_j} . \tag{A.4}$$

The velocity error thus depends on the emission error as well as additional error due to the computation of the apparent Doppler shift σ_u. σ_B was found assuming Poisson statistics in Eq. (A.2). The standard deviation of the apparent Doppler shift σ_u should depend on the Poisson statistics at each wavelength of the spectrum as well. However, it is preferable to base the standard deviation on variation in calibration data at similar intensity levels as the experiment rather than attempting to compute it based on Poisson photon statistics for two reasons. First, the ICCD has not been absolutely calibrated and basing the velocity error on photon statistics depends on the assumed gain. Second, systematic errors in the curvature calibration are probably just as significant as statistical errors. Therefore, σ_u is found from the standard deviation of Doppler shifts observed from a stationary calibration lamp, with the exposure time set so that the intensity of each row on the ICCD is similar to that of a binned spectrum during the experiment. An example of the variation in the Doppler shift is shown in Fig. 5.6. The standard deviation in the calculation of the Doppler shift σ_u is taken to be a constant 2.55 km/s, or about 0.4 pixels. The errors in the length matrices L and M are neglected.

The chord-integrated brightness B_i appears in the sums in both the numerator and the denominator, precluding the use of a closed-form expression for the velocity deviation σ_v. The velocity deviation can be found numerically, however. Gaussian distributions for B and u were created and the resulting velocity profile was computed.

A typical velocity histogram is shown in Fig. A.1 based on a 30,000 sample population. The velocity histogram is well-modeled as a Gaussian distribution.

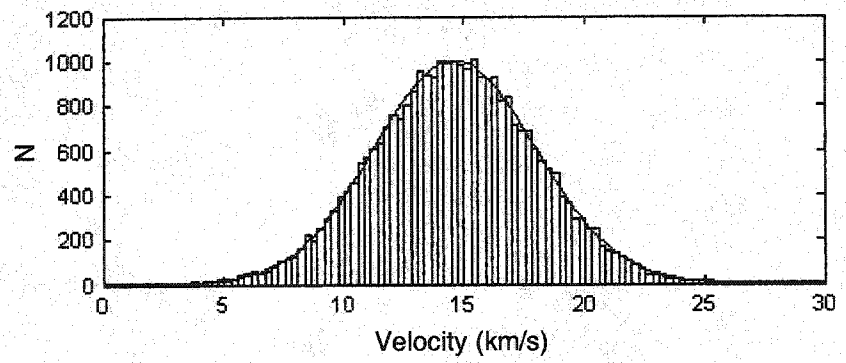

***Figure A.1**: Simulated Velocity Histogram. Solid black line: Gaussian distribution. Data generated from a 30,000 sample population.*

Vita

Andrew Maxwell Peter

Bachelor of Science Cum Laude, Mechanical Engineering, Cornell University, 1998.

Master of Science, Aeronautics and Astronautics, University of Washington, 2001.

Doctor of Philosophy, Aeronautics and Astronautics, University of Washington, 2003.